

EFFECTS OF AC STIMULATION ON CHICK DRG NEURITE GROWTH, DENSITY  
AND DIRECTIONALITY

A Thesis

Presented to

The Graduate Faculty of The University of Akron

In Partial Fulfillment

of the Requirements for the Degree

Master of Science

Pragya Jai Kumar

August, 2013

EFFECTS OF AC STIMULATION ON CHICK DRG NEURITE GROWTH, DENSITY  
AND DIRECTIONALITY

Pragya Jai Kumar

Thesis

Approved:

Accepted:

---

Advisor  
Dr. Rebecca Willits

---

Department Chair  
Dr. Brian Davis

---

Committee Member  
Dr. Erik Engeberg

---

Dean of the College  
Dr. George K. Haritos

---

Committee Member  
Dr. Hossein Tavana

---

Dean of the Graduate School  
Dr. George R. Newkome

---

Date

## ABSTRACT

The impact of electrical stimulation (ES) on growth and regeneration of nerves has been widely studied, with field strength, type of ES, and duration of application all demonstrating impact on the regeneration. However, little information exists directly comparing the frequency of alternating current (AC) stimulation impacts these cell behaviors. This study investigated the biological behavior of chick dorsal root ganglia (DRG): growth of the neurites, spreading of cells from DRG body, cell viability, neurite density and neurite directionality, at 4 frequencies to determine the most efficient frequency with the healthiest neurite growth. E9 chick DRG were stimulated directly with platinum electrodes with AC sinusoidal signals of  $2.5V_{p-p}$  amplitude and varying frequencies of 20Hz, 200Hz, 1MHz and 20MHz. Characterization of DRG was done using antibody staining. From this study, it can be concluded that application of AC EF increased the length, density and directionality of neurites at low frequencies. Also, application of ES increased cell spreading from the DRG body, which may guide the neurites. Moreover, neurites have greater growth in the high amplitude region of the stimulation chamber (or closer to the anode), indicating that the growth and density is influenced by the voltage intensity. From literature survey, the changes in the biological characteristics of DRG neurites may be due to changes in DRG conductivity.

## ACKNOWLEDGEMENTS

I would like to express my gratitude to my academic advisor Dr. Rebecca Kuntz Willits, for her constant guidance, remarks and engagement through the learning process of this master thesis. Furthermore, I would like to thank Dr. Erik Engeberg for his support and guidance on electrical topics and letting me use his electronic equipment. Also, I like to thank Dr. Hossein Tavana for his useful comments for the thesis.

I am also obliged to Ms. Shilpa Chakinala for her help in MATLAB processing, Mr. Vivek Krishna Nagarajan and Dr. Bryn Martin for their comments and tips. Special thanks to Kathleen McNamara and Wenda Zhou for teaching me about lab equipment and cell culture. I would like to thank my loved ones, who have supported me throughout entire process, both by keeping me harmonious and helping me putting pieces together. I will be grateful forever for your love.

## TABLE OF CONTENTS

	Page
LIST OF TABLES.....	vii
LIST OF FIGURES.....	viii
CHAPTER	
I. INTRODUCTION.....	1
II. BACKGROUND.....	4
Introduction to nervous system.....	4
Dynamics of ES of nerve tissue.....	11
Dielectric properties of tissues.....	17
Changes in biological properties of nerve tissues in EF.....	21
III. PURIFICATION OF SCHWANN CELLS FROM MIXED NEURONAL POPULATION.....	23
Introduction.....	23
Materials and Methods.....	24
Results.....	29
Discussion.....	36
Conclusion.....	38

IV.	EFFECTS OF LOW AND HIGH FREQUENCY STIMULATION ON NEURITE GROWTH, DIRECTIONALITY AND DRG CONDUCTIVITY .....	00	39
	Introduction.....		39
	Materials and Methods.....		40
	Results.....		54
	Discussion.....		71
	Conclusion.....		76
V.	CONCLUSION.....		78
VI.	FUTURE WORK.....		81
	BIBLIOGRAPHY.....		82
	APPENDICES.....		92
	APPENDIX A: DRG MODEL AND CONDUCTIVITY.....		93
	APPENDIX B: MATLAB CODES.....		101
	APPENDIX C: DATA TABLES AND FIGURES.....		105

## LIST OF TABLES

Table	Page
2.1: List of dielectric dispersion groups with respect to the input frequency and corresponding cellular mechanisms [54]. .....	20
4.1: Voltage and current measurements in the ES chamber for different frequencies at positions A and C.....	46
4.2: Average $\pm$ standard deviation neurite growth for all frequencies and positions. * represents the values that are significantly different from sham. ....	55
4.3: Average $\pm$ standard deviation CS ratio for all frequencies and positions.....	58
4.4: Average $\pm$ standard deviation % viability for all frequencies and positions. ....	61
4.5: Average $\pm$ standard deviation density ratio (D) for all frequencies and positions. * represents the values that are significantly different from sham. ....	64
4.6: Total number of points in 4 quadrants. Each point represents 75 neurites with $\pm 2.5^\circ$ . * represents the values that are significantly different from sham. ....	66
A.1: List of conductivities for Maxwell-Wagner and Cole-Cole models for different frequencies. ....	99
C.1: Cell densities of total cells and SC for mixed, non-adherent and adherent population, for the three time points. Data is depicted as average $\pm$ standard deviation, with sample size, n=28, n=43 and n=45 for 1, 2 and 4 hrs time points, respectively. ....	105

## LIST OF FIGURES

Figure	Page
2.1: Anatomical structure of a neuron. The cell body consists of cytoplasm that houses the nucleus and other important cellular organelles like mitochondria, endoplasmic reticulum, golgi apparatus, etc., where the important cellular processes take place. The cell body is surrounded by a cell membrane. The axon may be covered by myelin sheath which is generated by Schwann cells that is helpful in faster conduction of impulse to the axon terminal. (with permission: Quasar Jarosz at en.wikipedia) .....	5
2.2: Phases of neuron action potential. The resting membrane potential is $-70\text{mV}$ until arrival of a stimulus that increases the potential to threshold potential of $-55\text{mV}$ . Thereafter, due to opening of $\text{Na}^+$ channels, the neuron depolarizes to $+40\text{mV}$ . After attaining the peak, the neuron repolarizes due to closing of $\text{Na}^+$ channels and opening of $\text{K}^+$ channels. Finally, neuron has a hyperpolarizing phase where the $\text{K}^+$ channels remain open till the potential reaches resting state. (with permission: Human Medical Physiology) .....	8
2.3: Charge redistribution at electrode-electrolyte interface at the positive electrode. The application of EF creates a double layer interface at each electrode by attraction of the electrode to the counter-ion. [53 (with permission)].....	13
2.4: Diagrammatic representation of DC and AC current flow through a capacitor. The current source sends DC or AC signal to capacitor C of reactance $X_C$ . Since for DC input, $X_C$ is infinite, DC current is blocked by it and the output of the capacitor is only AC signal. ....	14
2.5: Graphical representation of change in capacitive reactance and current with respect to increase in frequency. An increase of frequency decreases the capacitive reactance and increases the current flow through it due to increase of rate of voltage that occurs at the plates of the capacitor. ....	15

2.6: Path of current flow in tissue at low and high frequency EF. The elliptical structures represent the cell while the grey background is the extracellular fluid. At DC, the current passes around the cells because the cell membrane acts as capacitance and blocks the flow of DC through it. As the input frequency increases, the membrane allows current to pass and the path of the current is through the cytoplasm. [53, (*with permission*)]. ..... 16

2.7: Representation of Gildemeister effect: the action potential is generated after summation of a certain number of cycles from the input signal at high frequencies. [38, (*with permission*)]. ..... 17

2.8: Dispersion regions  $\alpha$ ,  $\beta$ , and  $\gamma$  for permittivity  $\epsilon'$  and conductivity  $\sigma'$ . Each dispersion region is grouped based on response of the dielectric materials to frequency, and corresponds to specific cellular process. Note that with the increase of input frequency, the permittivity decreases while the conductivity increases. (53, *with permission*) ..... 20

3.1: Fluorescent and phase images of neuron (A, B) and SC (C, D) at 20x magnification. The 20x magnification was done to distinguish neurons and SC. As seen in A and B, the neurons have round cell body, with a prominent round or oval shaped nucleus, with a single axon protruding out. The green label of the neurofilament has fused with the blue labeled nucleus, indicating the cell in a neuron. On the contrary, C and D show SC, with bipolar morphology and a cigar-shaped nucleus. Scale bars are same for all images as in (A), line (upper left) indicates a scale of 20 $\mu$ m. .... 30

3.2: Fluorescent images of adherent (A, B) and non-adherent (C, D) populations at 1 hr time point. A, C represent fibroblasts (red) and neuron labeling (green) while B, D represent fibroblasts (red) and SC (green) labeling. Blue dots represent the nuclei of the cells. From A and B, it can be said that after 1 hr 38% of the total cells in mixed population adheres to the surface of the well plate while 68% of the total cells constitute the non-adherent population. The 1 hr time point also marks the separation of the fibroblasts constituting 87% of the total cells in the adherent population. Scale bars are same for all images as in (A), line (upper left) indicates a scale of 50 $\mu$ m ..... 32

3.3: Fluorescent images of adherent (A-B) and non-adherent (C-D) populations at 2 hr time-point. A, C represent fibroblasts (red) and neuron labeling (green) while B, D represent fibroblasts (red) and SC (green) labeling. Blue dots represent the nuclei of the cells. From A and C, it can be said that after 2 hrs the number of adherent cells increased

from 38% to 65%. Also, as indicated in C, 98% of the total cells in the adherent population label for SC with only 1.2% fibroblast contamination (the rest of the cells did not label for any cell type). Scale bars are same for all images as in (A), line (upper left) indicates a scale of 50 $\mu$ m. .... 33

3.4: Fluorescent images of adherent (A-B) and non-adherent (C-D) populations at 4 hr time-point. A, C represent fibroblasts (red) and neuron labeling (green) while B, D represent fibroblasts (red) and SC (green) labeling. Blue dots represent the nuclei of the cells. After 4 hrs, 95% of the total cells adhered to the surface with only 5% non-adherent cells in the non-adherent population. No cells labeled for neurons or SC in the non-adherent population. About 0.2% cells labeled for fibroblasts in the non-adherent population after 4 hrs (C, D). Scale bars are same for all images as in (A), line (upper left) indicates a scale of 50 $\mu$ m ..... 34

3.5: Graphical representation of average cell density  $\pm$  standard deviation of cells in adherent and non-adherent populations for 1, 2 and 4 hrs time points. The number of cells increased in the adherent population as the time increase. After 2 hr, 98.3% of the total cells in adherent population labeled for SC. .... 35

3.6: Graphical representation of average cell density  $\pm$  standard deviation of mixed, adherent and non-adherent populations for 1, 2 and 4 hrs time points. For 2 hr and 4 hr time points,  $n > 43$ , for the mixed population,  $n = 45$  and for 1 hr time point,  $n = 28$ . Statistical significance is indicated by \*, \*\* and \*\*\* which represent differences from mixed population, 1h and 2h time points, respectively. ( $p < 0.05$ )..... 36

4.1: Schematic representation of the ES chamber. The units of the distances are in cm. The anode and cathode are made of platinum sheets which is connected with the function generator that supplies the input sinusoidal signal at 2.5 V<sub>p-p</sub>, at 20Hz, 200Hz, 1MHz and 20MHz. Positions A and C represent the position of the DRG containing coverslip. The chamber is filled with PBS and the flow of charges through PBS on application of EF is from anode to cathode. Position A is exposed to higher EF intensity than position C due to resistance of the PBS and the DRG, the system acts as a voltage divider circuit. Thus, net resistance at position C is more than position A, which results in less intensity..... 44

4.2: Voltage measured at positions A and C for 20Hz, 200Hz, 1MHz and 20MHz. This experiment was done to ensure that the voltage and current passing through the DRG at different frequencies was the same, and that frequency was the only variable. Figure A

represents the circuit diagram of the experiment, where a resistor  $R_{sens} = 98.3\Omega$  was placed to near the cathode. The voltage across  $R_{sens}$  was used to calculate the current flow in the system using Ohm's law. (B-E) shows the voltage at positions A and C, and  $R_{sens}$  for all frequencies of stimulation. Results showed 3.7% shift in the voltages across all the frequencies, which is negligible..... 45

4.3: Measurement of neurite length and cell distance. Concentric circles are drawn around the DRG body and the tip of the longest neurite (B) or the farthest cell (C). (A) Pre-stimulated image, with  $i_1$  and  $O_1$  as the inner and outer radius of the circles; (B-C) post-stimulation fluorescent images for neurites and cells. The length of the longest neurite and the distance of farthest cell were calculated using Eqns. 4.2 and 4.3. Scale bar in (A) is  $100\ \mu\text{m}$  and in (B-C) are  $500\ \mu\text{m}$ ..... 48

4.4: Diagram of the density measurement method. The original image is shown in A. The DRG body and the surrounding neurites are zoomed in and cropped (B) to reduce the background. The center pixel x and y coordinates are determined and the image is split into two equal parts (images C and D). The number of white pixels in each half is counted and the ratio of cathode to anode (D) is considered for analysis. If D is greater than 1, then the neurites are denser towards the cathode..... 52

4.5: Diagram illustrating the quantification of directionality of neurites using polar plots. The plot was divided into 4  $90^\circ$  quadrants, and each quadrant was sub-divided into 3  $30^\circ$  segments. Quadrant 1 faced the cathode (C) whereas quadrant 1 faced the anode (A).... 53

4.6: Post-stimulated images of DRG samples, A is sham, B-E are stimulated DRG for position A for 20Hz, 200Hz, 1MHz and 20MHz, respectively, while F-I are for position C. The lengths of the neurites were measured by Eqn. 4.2. From the figure, it is clear that neurites grow longer in LF stimulations, and the length of neurites for HF was similar to control. The white bar in A represents a scale of  $500\ \mu\text{m}$ . ..... 56

4.7: Graphical representation of average neurite growth  $\pm$  standard deviation for all the frequencies of stimulation for positions A and C. The sample size was  $n = 40$  for each case. Statistical significance between the sham and stimulated samples is indicated by \* ( $p < 0.05$ ). Results indicate that neurite length for 20Hz, 200Hz and 1MHz (position A) is significantly different from sham and HF. Thus, LF stimulation promotes growth. Also, the length at position A was significantly different from position C for LF samples, indicating that high intensity fields aids in more growth of neurites..... 57

4.8: Post-stimulated images of DRG samples, yellow dots represents the cells; A is sham, B-E are stimulated DRG for position A for 20Hz, 200Hz, 1MHz and 20MHz, respectively, while F-I are for position C. The distance of furthest cell from the DRG body was quantified by Eqn. 4.5. The figure illustrates that the cells spread to greater distances in stimulated samples, regardless of frequency and intensity of EF, than the control samples. The white bar in A represents a scale of 500  $\mu\text{m}$ . ..... 59

4.9: Graphical representation of average CS ratio  $\pm$  standard deviation for all the frequencies of stimulation for positions A and C. The sample size was  $n = 40$  for each case. Results indicated that CS ratio for stimulated samples was significantly different from the control samples..... 60

4.10: Post-stimulated images of DRG for viability study; the green stained images represent the live cells and the red stained images represent the dead cells. The images show that application of EF at high intensity or high frequency does not significantly impact cell viability than compared to control sample. The white bar in A represents a scale of 500 $\mu\text{m}$ ..... 62

4.11: Graphical representation of average % viability  $\pm$  standard deviation for all the frequencies of stimulation for positions A and C. The sample size was  $n = 40$  for each case. Results indicate that the cell viability for stimulated samples is not significantly different from the control samples. Thus, application of ES at any intensity or frequency does not affect the cell viability. .... 63

4.12: Graphical representation of average density ratio (D)  $\pm$  standard deviation for all the frequencies of stimulation for positions A and C. The sample size was  $n = 40$  for each case. Statistical significance between the sham and stimulated samples is indicated by \* ( $p < 0.05$ ). Results indicated that density for 20Hz, 200Hz and 1MHz (position A) was significantly different from sham and HF. Thus, LF stimulation led to growth of denser neurites towards cathode. Also, D at position A was significantly different from position C for LF samples, indicating that high intensity fields aided in denser growth of neurites. .... 65

4.13: Polar plots for directionality measurements for 20Hz position A (A) and 20MHz position A (B), and control (C). The plots show that neurites grow symmetrically around the DRG body for control and 20MHz. For 20Hz, the number of neurites in quadrant 1

was significantly more than other quadrants, as well as control and 20MHz. Thus, neurites show cathodal preference at LF stimulation. .... 67

4.14: Graphical representation of the total number of tips per quadrants for 20Hz, 200Hz, 1MHz and 20MHz. A illustrates the number of tips per quadrant for position A, while B represents position C. 4500 neurites were counted for each condition. The plot representing sham is flat in both cases, indicating that neurites grow equally in all quadrants. The number of neurites is largest in quadrant 1 for 20Hz and 200Hz, indicating that more neurites grow to the side if the DRG facing cathode. The plots for 1MHz and 20MHz look similar to sham, depicting that HF does not promote directional growth of neurites. .... 68

4.15: FEA plot of the voltage distribution in the ES chamber. Using boundary condition specifications, left side of R1 was stimulated at  $V=2.5$ . The DRG were placed 0.5cm away from each electrode. Results indicated that DRG at position A was exposed to 2V while DRG at position C was exposed to 0.9V, which was similar to the results obtained experimentally (Table 4.1). The red arrows represent the current density field lines. .... 71

A.1: Tissue conductivity of grey matter with respect to frequency of stimulation..... 94

A.2: (A) A schematic diagram of a suspension of cells; (B) An electric circuit equivalent of the effective conductivity of the suspended cells. .... 95

A.3: Diagram of Maxwell-Wagner model in parallel combination..... 96

A.4: Diagram of Cole-Cole model in parallel combination..... 97

A.5: Plot of DRG conductivity using Maxwell-Wagner model and Cole-Cole model, with respect to frequency. The conductivity values were obtained by using admittance equations of these models. The results show very low conductivity values at 20Hz, 200Hz but increase at higher frequencies. However, the values of conductivity at high frequencies for Maxwell-Wagner and Cole-Cole models differ by about 0.45 S/m. .... 98

Figure C.1: Polar plots for directionality measurements for control, 20Hz position A, 20Hz position C, 200Hz position A, 200Hz position C, 1MHz position A, 1MHz position C, 20MHz position A, and 20MHz position C. .... 108

## CHAPTER I

### INTRODUCTION

A recent survey by National Center for Health Statistics shows that as of December 2011, 50,000 cases of peripheral nerve repair procedures have been performed per year and the annual cost for treatment of such injuries is about \$7 billion [1]. However, less than 1% of the patients are discharged with complete functional recovery [1]. Many studies are being carried out to enhance the therapeutic procedures for treatment of such injuries, in order to improve the quality of life for the patients suffering from peripheral injuries. One such modality is the application of external electric fields for structural and functional recovery of the injured peripheral tissues.

External stimulation of nerve tissues is a widely researched method to aid in nerve regeneration. These methods include the application of electric and magnetic guidance cues to encourage and direct neurite regeneration. Electrical fields (EFs) and pulsed electromagnetic fields (PEMFs) have been found to improve repair of nerve injuries *in vivo* and enhance neuronal development by increasing neurite outgrowth and aligning the neurites with respect to direction of the EF *in vitro* [2-5]. Moreover, studies have demonstrated that direct current (DC) electric stimulation improves activity of non-neural

cells like Schwann cells, indirectly boosting the growth of nerves [6]. Some researchers have used alternating current (AC) to stimulate nerves due to certain benefits offered by AC stimulation over DC stimulation, like decreased power consumption, and increased field propagation inside the tissue [7].

Nerve tissue response to external EFs can be due to various characteristics of the tissue, one of which is the conductivity. According to Gabriel et al., any biological tissue contains a resistive and capacitive component [8]. The membranes of all the cells in the tissue add up as the capacitive element while the extracellular fluid (ECF), cytoplasm, and the cellular organelles inside constitute the resistive element [9]. The dielectric properties of the tissue will change due to the presence of the capacitive component. Thus, the tissue conducts the EF differently for DC, low frequency AC, and high frequency AC stimulation.

Research has demonstrated that application of high frequency electromagnetic fields (EMF) does not have significant effect on neurite growth compared to sham in 7 days of culture [94]. However, the comparisons of neurite growth with respect to frequency were not direct. Thus, the motivation of the present study was to directly compare the difference in neurite growth, neurite density and neurite alignment at low or high frequency AC fields. In addition, location of the support cells that reside within the tissue after stimulation was quantified to examine spreading of cells relative to neurite growth. Also, parallel comparisons were made between the electrically stimulated samples with the control samples to establish that the effects occur as a result of the stimulation and not other factors. The specific goals of the project were as follows:

*Goal 1:* Identify the cell types in chick DRG and purification of Schwann cells from mixed population.

*Goal 2:* Determine the impact of ES on length of neurites.

*Goal 3:* Quantify changes in cell movement with different ES and compare to neurite length.

*Goal 4:* Quantify cell viability with respect to frequency of stimulation.

*Goal 5:* Determine the impact of ES on neurite density.

*Goal 6:* Determine the impact of ES on growth orientation of neurites.

## CHAPTER II

### BACKGROUND

#### 2.1 Introduction to nervous system

Multicellular animals must monitor and maintain a constant internal environment as well as respond to external stimuli. In many animals, both these vital functions are coordinated by an integrated organ system: the nervous system (NS). The NS is divided into central nervous system (CNS), which comprises of brain and spinal cord, and peripheral nervous system (PNS), which connects the CNS to other body parts using nerves. The CNS controls the body by means of passage of electrical signals called impulse. There are two main components of the PNS: sensory (afferent) pathways that provide input from the body into the CNS and the motor (efferent) pathways that carry impulses to muscles and glands (effectors).

##### 2.1.1 Neurons and neuroglia

At a cellular level, the structural and functional unit of the nervous system is called a nerve cell or neuron, which transmits impulses from one point to another. A neuron consists of cell body, dendrites, and an axon. The cell body is the central part of the neuron, which contains the nucleus of the cell in the cytoplasm along with other cellular

components like mitochondria, endoplasmic reticulum, etc. The dendrites are branched cellular extensions, and their main function is to pass the input impulses into the cell body. The axon is the longest projection from the cell body that carries impulses away from the cell body to the next neuron at axon terminals. The axon terminal contains synapses, specialized structures where neurotransmitter chemicals are released to communicate with target neurons. The axon may or may not be covered by a layer of insulation called myelin sheath, which helps in faster conduction of electric impulses. Figure 2.1 shows the anatomical structure of a neuron.

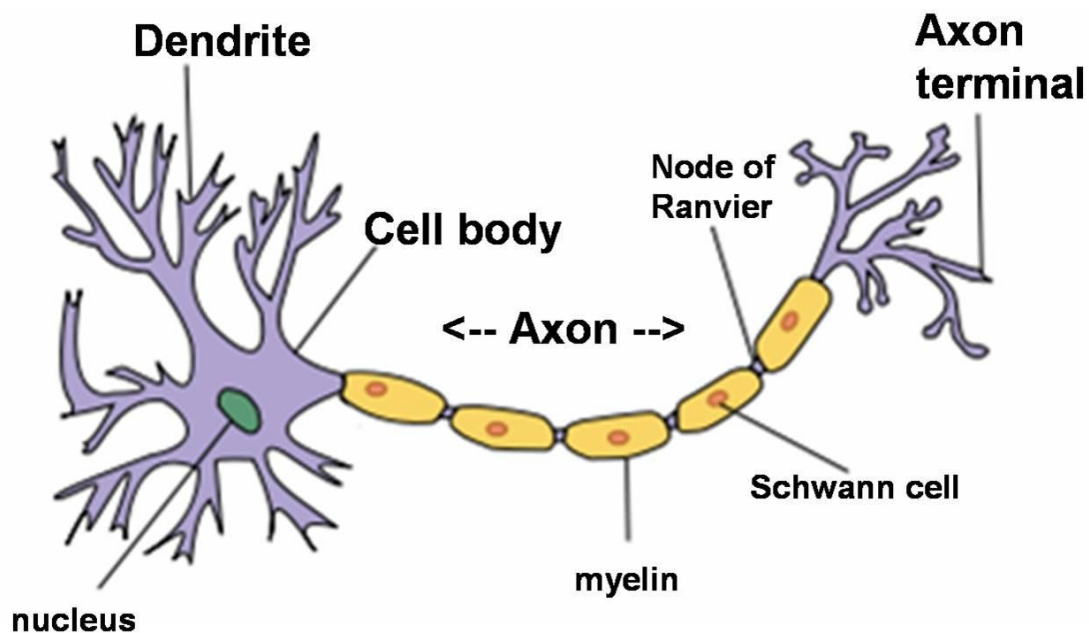


Figure 2.1: Anatomical structure of a neuron. The cell body consists of cytoplasm that houses the nucleus and other important cellular organelles like mitochondria, endoplasmic reticulum, golgi apparatus, etc., where the important cellular processes take place. The cell body is surrounded by a cell membrane. The axon may be covered by myelin sheath which is generated by Schwann cells that is helpful in faster conduction of impulse to the axon terminal. (with permission: Quasar Jarosz at en.wikipedia)

The NS also contains non-neuronal cells called glial cells; their primary function is to provide support and protection to the neurons. The major glial cells of CNS are

astrocytes, oligodendrocytes, ependymal cells, and radial glia, while PNS glia are Schwann cells, satellite cells, and enteric glial cells [19]. In the PNS, nerve fiber bundles are encapsulated in fibroconnective tissue that is also comprised of fibroblasts. The main role of fibroblasts is the synthesis of the extracellular matrix and collagen, but they are critical to the wound healing process [10]. For example, fibroblast growth factors are secreted in the pituitary gland that causes fibroblasts to proliferate [19]. Research performed by Grothe et al. demonstrated that basic fibroblast growth factor (FGF-2) and its receptors are expressed in nerve tissues and upregulated in DRG following peripheral nerve injury [12]. FGF-2 was found to aid the injured neurons and support neurite outgrowth of injured nerves by increasing the healing action of fibroblasts [12]. Other studies have noted that fibroblasts play a role in nerve regeneration through increase of FGF-2 aids in peripheral nerve injury [13, 16, 17].

The myelin surrounding peripheral nerve axons is supplied by Schwann cells (SC), whereas oligodendrocytes perform this role in the CNS [2, 19, 20]. SC constitute the majority of the neuroglia in PNS and play an important role in nerve regeneration [14]. Growth of degenerated nerves depends on the presence of many neurotrophic factors such as nerve growth factor (NGF), brain-derived neurotrophic factor (BDNF), interleukin-6 etc., which are known to be secreted by SC [12]. SC are known for their roles in supporting regeneration of injured nerves by the process of phagocytosis (digestion of myelin) [15]. The onset of phagocytosis attracts macrophages that further clear axon debris [15, 18]. SC emit growth factors that attract new axonal sprouts growing from the proximal stump and create a 'tunnel' between the regeneration axon the target organ [18].

### 2.1.2 Nerve impulse: generation and propagation

An action potential is an electrical wave that travels along the length of the neuron, where the electrical membrane potential of a cell rapidly rises and falls [20]. Action potentials occur in electrically excitable cells like neurons, muscles, etc. The action potentials occurring in nerve cells are called impulses and play a central role in transferring signals from brain and spinal cord to effector organs and vice versa.

The electric potential across any cell's plasma membrane with respect to the interstitial fluid is called its membrane potential. Specialized protein structures called ion pumps and ion channels aid to pass the impulse through the length of the axon. Typically,  $\text{Na}^+$ ,  $\text{K}^+$  and  $\text{Ca}^{2+}$  ion channels play an important role in impulse transmission. At a resting state, the potential across the membrane is called resting membrane potential, and its value is -70mV and the concentrations of  $\text{Na}^+$  and  $\text{Cl}^-$  are higher in the extracellular fluid than intracellular fluid while the concentration of  $\text{K}^+$  is more in the intracellular fluid. This concentration gradient causes an outflow of  $\text{K}^+$  making the resting potential close to -70 mV. The stimulus has to increase the membrane potential to a threshold potential of -55mV to trigger an action potential. Once the potential reaches threshold, it rises rapidly to around +40mV and the phase is called depolarization lasting approximately 1 to 2 msec. The membrane potential increases due to the binding of the stimulus by means of neurotransmitter to a specific ion channel, like  $\text{Na}^+$ , which opens the channels allowing inflow of  $\text{Na}^+$  ions. Simultaneously, the  $\text{K}^+$  channels open and  $\text{K}^+$  ions move out of the cell. The inward flow of  $\text{Na}^+$  ions increases the concentration of positively charged cations in the cell, thereby increasing the membrane potential (depolarization). At the peak of the potential,  $\text{Na}^+$  channels close, but the  $\text{K}^+$  ions continue to exit the cell. After

reaching the peak, the membrane potential drops rapidly to below the resting membrane potential and the phase is termed as repolarization. The continuous outflow of  $K^+$  ions decreases the membrane potential of the cell and the neuron is incapable of producing an action potential due to the inactivation of voltage-gated  $Na^+$  channels and the lag in closing of the  $K^+$  channels. In addition, an influx of  $Ca^{2+}$  into the membrane causes more  $K^+$  channels to open. Hence, an undershoot or hyperpolarization persists until the membrane potassium permeability returns to its usual value, as shown in Figure 2.2. This period of incapability of the neuron to respond to stimulus is known as refractory period. The absolute refractory period corresponds to the time required for the voltage-activated  $Na^+$  channels to close.

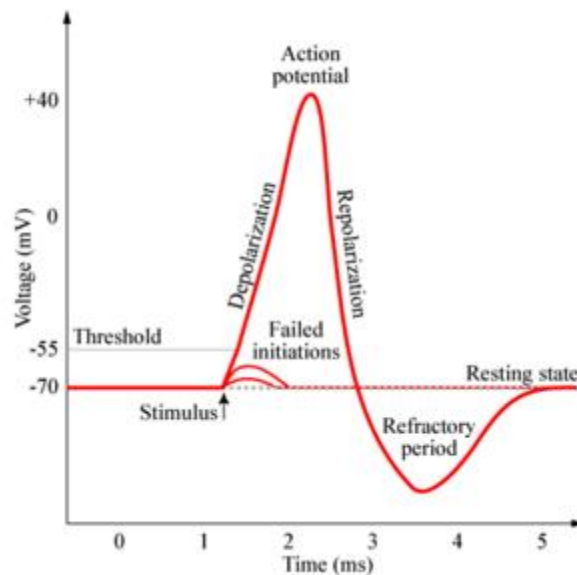


Figure 2.2: Phases of neuron action potential. The resting membrane potential is  $-70\text{mV}$  until arrival of a stimulus that increases the potential to threshold potential of  $-55\text{mV}$ . Thereafter, due to opening of  $Na^+$  channels, the neuron depolarizes to  $+40\text{mV}$ . After attaining the peak, the neuron repolarizes due to closing of  $Na^+$  channels and opening of  $K^+$  channels. Finally, neuron has a hyperpolarizing phase where the  $K^+$  channels remain open till the potential reaches resting state. (with permission: *Human Medical Physiology*)

The transmission of the nerve impulse occurs along the length of the axon. To ensure efficient and faster conduction of impulses, a phenomenon called saltatory conduction occurs. The myelin sheath plays a major role in saltatory conduction. The myelin sheath is a layer of insulating material that enwraps the axon in segments separated by intervals known as nodes of Ranvier. The myelin is produced by specialized cells: Schwann cells (SC) in the PNS, and oligodendrocytes in the CNS. The myelin sheaths reduce membrane capacitance in the inter-node intervals, thus allowing a fast movement of action potentials from node to node [21, 22]. Also, the cytoplasm of the axon is electrically conductive, and because the insulating myelin does not let charge leak through the membrane, depolarization at one node is sufficient to elevate the voltage at a neighboring node [21]. At each successive node, the membrane potential of the axon is brought to the threshold potential to initiate an action potential. Thus, in myelinated axons, action potentials do not propagate continuously as waves throughout the length of the axon, but recur at successive nodes, thereby increasing the efficiency and time of the impulse transmission. The speed with which the impulse propagates along the axon is called conduction velocity, which is dependent on the axon diameter, degree of myelination, conductivity of axon, etc. [22].

The passage of the electrical impulse from one neuron to another occurs with the help of the synapse. The impulse transfer occurs via neurotransmitters or gap junctions. The neurotransmitters are trapped in vesicles in the membrane of the pre-synaptic axon terminal and on the onset of the impulse, they diffuse into the interstitial fluid and bind to specific receptors in the membrane of the post-synaptic neuron [20]. Thereafter, they release the signal into the target neuron.  $\text{Ca}^{2+}$  plays a vital role in the process of

neurotransmitter release; when the action potential reaches the nerve terminal, voltage-dependent  $\text{Ca}^{2+}$  channels open and  $\text{Ca}^{2+}$  rushes into the neuron terminal due to a greater extracellular concentration. On the other hand, gap junctions are specialized connections between two cells and are composed of proteins. The gap junctions allow free flow of ions from one cell to another and the impulse can transfer freely and more rapidly into the target cell [19, 20].

### 2.1.3 Dorsal root ganglia

The DRG contain groups of cell bodies of neurons that carry signals from sensory organs towards the CNS. They are located at the dorsal side of the spine in vertebrates. The DRG develop in the embryo from neural crest cells [25]. The axons of the DRG are known as afferent neurons because they carry impulses from the sensory organs like eye, ear, nose, tongue, skin, etc. to their corresponding integration center in the CNS [20, 25]. As discussed earlier, the main glial cells in the PNS are SC and the neurons and SC are surrounded by a mesh of fibroblasts, thus, the main cellular components of the DRG are neurons, SC, and fibroblasts.

The DRG neurons have various receptors for specific ions or other stimuli, and the research on this topic is ongoing. For example, 31-40% of the DRG neurons express G protein-coupled-receptors (GPCRs) [23]. The DRG also contain mechanoreceptors that respond well to a mechanical stimulus and produce action potentials [24]. However, the diameters of the axons from the DRG are relatively small compared to other systems, thereby reducing the conduction velocity [24]. Early studies done by Harper et al. and

Nieminen et al. have used voltage clamping technique to determine the electrical properties of DRG [26, 27].

Characterization of electrical properties of DRG neurons based on external electric stimulation has also been widely studied. An application of external DC fields and low frequency AC fields enhanced neurite outgrowth from the DRG [2, 3]. Moreover, stimulation at a low frequency of 20Hz for an hour led to an increase in DRG neurons regenerating into cutaneous and muscle branches than compared to unstimulated samples or samples stimulated for a longer duration [28]. It has been hypothesized that the upregulation of  $Ca^{2+}$  release after stimulation has an important role to play in the increase of neurite growth from the DRG. Study by Wan et al. shows that an increase of  $Ca^{2+}$  increased the release of neurotrophic factors like BDNF, while several studies suggest that influx of  $Ca^{2+}$  across the neuronal membrane could impact second messenger systems regulating the elongation of neurites or interaction with cation-dependent cytoskeletal components that modulate the morphology and motility of the growth cone [29-32].

## 2.2 Dynamics of ES of nerve tissue

This section describes the intracellular processes that occur on the application of EF to nerves. The changes in the electrical properties of the tissue, like bioimpedance and conductivity, at a resting state and after field application are compared. Also, changes in the electrical properties of nerve on application of different field types are explained.

### 2.2.1. Electrochemical processes in the electrolyte after EF application

In the simplest ES system, two metal electrodes are placed in an electrolyte and voltage is applied at the electrodes that drive a current between the electrodes. When a metal electrode is placed in an electrolyte and voltage is applied across it, an interface is created between the electrode and the electrolyte phases, where the transfer of charges occurs from electrons in the electrode to ions in the electrolyte. At the interface, a double layer of charge is created, which acts like a simple parallel plate capacitor, as shown in Figure 2.3 [33, 37]. The double layer occurs because application of voltage at electrodes drives one electrode to a positive potential while the other electrode goes into a comparatively negative potential. The positive electrode has an accumulation of positive charges (cations) that attracts negative charges (anions) from the electrolyte. The exact opposite effect occurs at the other electrode. The redistribution of charges in the electrolyte creates a double layer at the interface. The charge transfer from the electrode to the ions in the electrolyte occurs by charging and discharging of the capacitor [33, 34, 37].

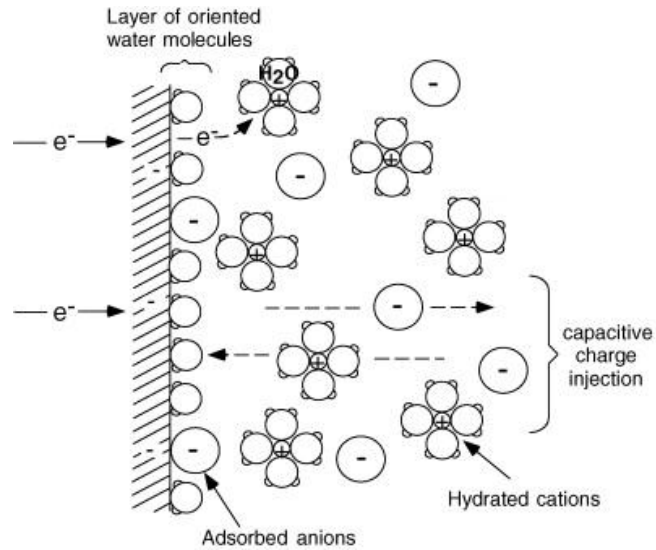


Figure 2.3: Charge redistribution at electrode-electrolyte interface at the positive electrode. The application of EF creates a double layer interface at each electrode by attraction of the electrode to the counter-ion. [53 (*with permission*)]

When the charge is transferred from the electrode to the electrolyte, the presence of a potential difference between the electrodes drives the current through the electrolyte that surrounds the nerve tissue. The current interacts with the axon membrane and the positive potential of the electrode causes redistribution of charges near the membrane, with positive charge accumulating outside the membrane [53]. The redistribution of charges causes depolarization of the membrane by opening the  $\text{Na}^+$  and  $\text{K}^+$  channels [34, 35]. The negative charges move intracellularly from the region near the cathode (negative electrode) towards the anode (positive electrode).

### 2.2.2. DC vs AC stimulation – current path in the tissue

The response of nerve tissues to ES depends largely upon the type of waveform being applied. The reason for the change in response is due to the inherent bioimpedance properties of the tissue and the extracellular fluid surrounding it. The membrane of the

cell has more capacitive properties and the cytoplasm is more resistive in nature [54, 33, 36]. These passive elements would respond differently to DC, low frequency AC, and high frequency AC signals. The current always follows the least resistive path.

A capacitor blocks DC signal but allows AC signal to pass [54]. The capacitive reactance,  $X_C$ , is defined as the resistance of the capacitor to a change in voltage.  $X_C$ , for a capacitor of capacitance,  $C$ , at frequency,  $f$ , is given by:

$$X_C = \frac{1}{2\pi f C} \quad (2.1)$$

Since the value of  $f$  for DC is 0,  $X_C$  tends to infinity. Thus, DC does not pass through capacitor as the capacitor offers infinite resistance to DC, as shown in Figure 2.4. From Equation 2.1, an increase of frequency decreases the reactance of the system. At very high frequencies,  $X_C$  becomes 0 (short circuit). For a capacitor, the current increases with the increase of frequency because the rate of voltage change across its plates increases, as shown in Figure 2.5.

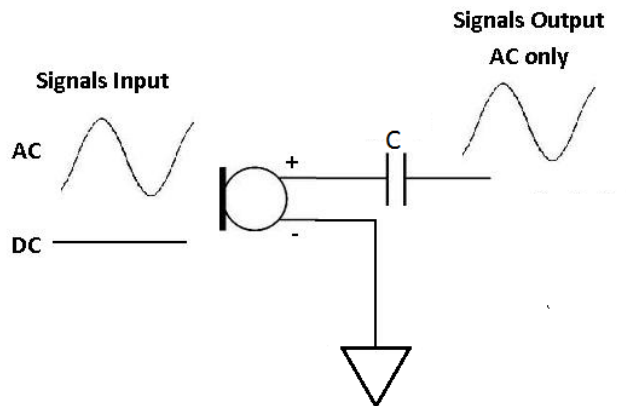


Figure 2.4: Diagrammatic representation of DC and AC current flow through a capacitor. The current source sends DC or AC signal to capacitor  $C$  of reactance  $X_C$ . Since for DC

input,  $X_C$  is infinite, DC current is blocked by it and the output of the capacitor is only AC signal.

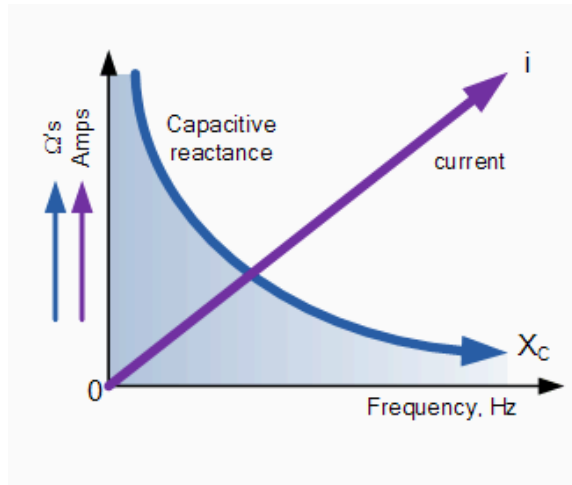


Figure 2.5: Graphical representation of change in capacitive reactance and current with respect to increase in frequency. An increase of frequency decreases the capacitive reactance and increases the current flow through it due to increase of rate of voltage that occurs at the plates of the capacitor.

In cells, the membrane acts as the capacitor [53]. At DC and AC frequencies (up to 1kHz), the current passes around the cells [53]. Due to the capacitive nature of the membrane, the cytoplasm does not contribute to current flow. However, at higher frequencies the membrane capacitance allows AC current to pass removing any membrane effects, and the current flows through the cell interior, as shown in Figure 2.6.

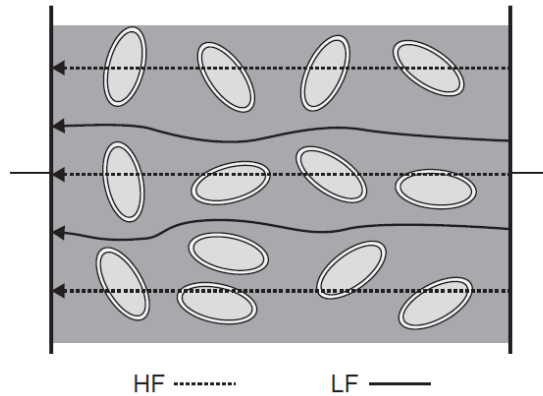


Figure 2.6: Path of current flow in tissue at low and high frequency EF. The elliptical structures represent the cell while the grey background is the extracellular fluid. At DC, the current passes around the cells because the cell membrane acts as capacitance and blocks the flow of DC through it. As the input frequency increases, the membrane allows current to pass and the path of the current is through the cytoplasm. [53, (*with permission*)].

### 2.2.3 AC stimulation – generation of action potential

Another important difference in the application of DC and AC fields for nerve stimulation is the effect on the action potential. Cycle-synchronous depolarization takes place when nerve tissues are stimulated with DC or low frequency current [38]. According to this principle, every pulse of DC or AC causes a depolarization of the nerve fiber (provided the duration and strength of the pulse are sufficient). Action potentials are generated in the nerve in a rhythm synchronous to the frequency of the applied current. If the stimulation frequency increases, the depolarization frequency will increase correspondingly. But every nerve fiber has its maximum depolarization frequency, which is determined by the refractory period. For example, the maximum depolarization frequency for the largest myelinated nerve fiber is located between 800 and 1,000 Hz. During ES of nerve fibers with a frequency over 1,000 Hz, a number of pulses occur in the refractory period, i.e., not every AC pulse leads to a depolarization. Depending on the duration of the refractory period, the nerve does not react to every pulse but react to the

stimulation current at its own frequency. Thus, the depolarization frequency of the nerve no longer coincides with the frequency of the current, or with the depolarization frequency of other nerve fibers in the nerve bundle. This phenomenon is known as asynchronous depolarization [38].

After every cycle of an AC, the potential difference decreases slightly and approaches a threshold value. After a certain number of cycles (after a certain effective time) the threshold value is reached, resulting in a depolarization. The higher the intensity of the current, the shorter is the effective time for depolarization. The depolarization of nerve fibers according to this summation principle is known as the Gildemeister effect, as shown in Figure 2.7 [38, 39].

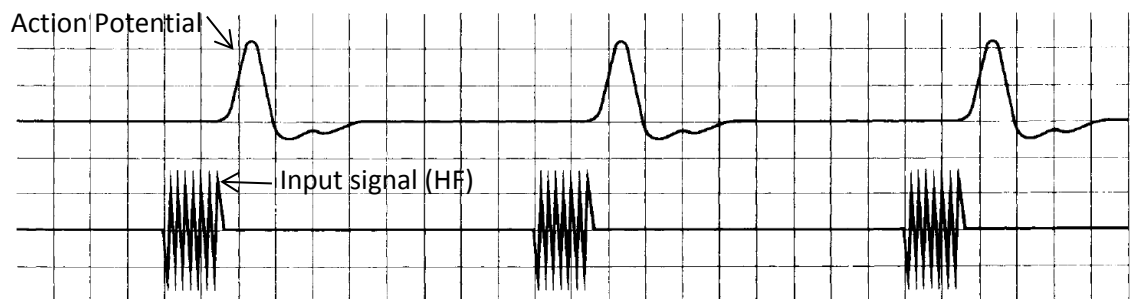


Figure 2.7: Representation of Gildemeister effect: the action potential is generated after summation of a certain number of cycles from the input signal at high frequencies. [38, (with permission)].

### 2.3 Dielectric properties of tissues

As discussed earlier, biological tissues have inherent electrical properties such as membrane capacitance, cytoplasmic resistance, etc. However, the electrical properties of tissues are dual in nature, thus one can regard tissues as dielectrics. A dielectric is defined

as ‘a material that the electric field penetrates’; conductors do not allow static EF penetration [53]. Any dielectric material has dielectric properties such as permittivity, conductivity, admittance, etc., which are dependent on time or frequency. Dielectric properties arise from a bound charge that is displaced by the application on EF, creating a dipole. The movement of free charges in the dielectric produces conductivity, whereas stationary dipoles produce permittivity. In such a case, we can combine the electrical properties into a complex conductivity,  $G$ :

$$G = G' + jG'' \quad (2.2)$$

Where, real part  $G'$  accounts for the magnitude of the conductivity, and  $G''$  gives the dielectric loss in the system. The real part of  $G$  accounts for the movement of charge that is in phase with the electric field; the imaginary part accounts for out-of-phase motion.

### 2.3.1 Relaxation and dispersion

Under the influence of EF, charge distribution occurs in the biomaterials (polarization), which has a direct effect on a material’s dielectric properties. If the intensity or direction of the applied EF changes with time, the charge distribution in the material also becomes time-dependent. Thus, the orientation of charge in the biomaterial due to the impact of a time varying EF is called relaxation [54]. Relaxation models include measurement of dielectric properties like permittivity with respect to changes in time, when a step input signal is applied. The permittivity of the biomaterial is measured in time domain and plotted.

The concept of relaxation is not valid while measuring the conductivity of the biomaterial because conductivity is constant with respect to time [54]. In such cases, the dispersion

phenomenon is considered where the change in charge distribution of biomaterial is measured in the frequency domain. The main difference between relaxation and dispersion is that for dispersion studies, the input signal has varying frequency. Thus, instead of applying step inputs, a sinusoidal input can be applied for dispersion studies. The resultant permittivity or conductivity of the biomaterial is plotted as a function of frequency.

The concept of dispersion was first introduced by Schwan, where he divided the dispersion mechanisms into three groups –  $\alpha$ ,  $\beta$ , and  $\gamma$  – each group related to different cellular mechanisms that occur in the tissue in a particular frequency range [53]. The changes in permittivity in frequency range from 0Hz – 1GHz is shown in Figure 2.8. Table 2.1 lists the dispersion groups with the corresponding frequency and cellular mechanism. From Figure 2.8, it is clear that the permittivity of any dielectric decreases with increase in frequency, because the charges are not quick enough to orient according to the changes in the EF [53].

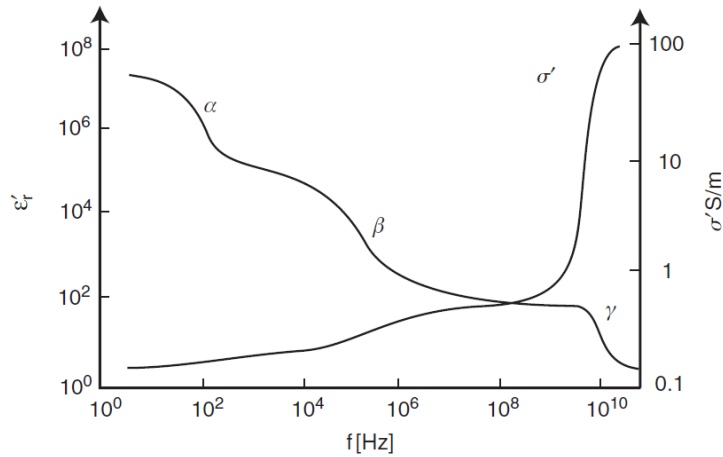


Figure 2.8: Dispersion regions  $\alpha$ ,  $\beta$ , and  $\gamma$  for permittivity  $\epsilon'$  and conductivity  $\sigma'$ . Each dispersion region is grouped based on response of the dielectric materials to frequency, and corresponds to specific cellular process. Note that with the increase of input frequency, the permittivity decreases while the conductivity increases. (53, *with permission*)

Table 2.1: List of dielectric dispersion groups with respect to the input frequency and corresponding cellular mechanisms [54].

Type	Characteristic frequency range	Cellular mechanisms
$\alpha$	mHz – kHz	Counterion effects near membrane surfaces, active cell membrane effects and gated channels, ionic diffusion, dielectric losses.
$\beta$	kHz – MHz	Maxwell-Wagner effects, passive cell membrane capacitance, intracellular organelle membranes, protein molecule response
$\gamma$	GHz	Dipolar mechanisms in polar media such as water, salt solution.

## 2.4 Changes in biological properties of nerve tissues in EF

Many studies have been done in order to observe the effects of external stimulation on the nerve tissue with respect to the field of application. A number of different types of external fields have been tested, both for *in vivo* and *in vitro* studies; some of them are DC, AC, magnetic fields, EMF, pulsed electromagnetic fields (PEMF) etc. This section elaborates the various works performed using external stimulation of nerve tissues or cells, and summarizes their findings.

The effect of stimulation on neurite outgrowth has been widely studied. According to Wood et al., short duration DC stimulation of chick embryo DRG enhanced neurite outgrowth [2]. Various other studies have studied the effect of DC or low frequency fields and have found that their application enhances the growth of neurites [3, 4, 47]. The length of the neurite growth after DC and low frequency stimulations (up to 200 Hz) were around 400 $\mu$ m, indicating that the field effect of DC and low frequency AC on neurite growth is similar [2, 29]. Koppes et al. proposed that EF increases the production of nerve growth factors (NGF) in SC, promoting neurite growth [6]. Other factors influencing neurite extension are support cell participation, substrate, soluble factors, external forces, and topography [7, 46]. AC stimulation of *Xenopus laevis* tissue *ex vivo* increased the neurite outgrowth with growth pattern similar to DC stimulation, yet having the additional advantage of increased field propagation [50]. On the contrary, research also indicated the application of a phasic pattern of stimulation led to retraction of neurite growth [47, 30-32]. According to Fields et al., the retraction of neurites may be for stabilization of outgrowth in the neurons by stopping further growth of neurites in neurons that failed to initiate synaptic contacts with the other neurons [47].

Another important trait in nerve tissue characteristics is the spreading of cells. Movement of newly formed neurons is a well regulated process that is critical for the development of brain architecture [76]. During brain development, neurons arise from the proliferative epithelium that covers the ventricular space throughout the neural tube. From there, the new neurons disperse throughout the nervous system [77, 78]. According to Marin et al., movement of cells is closely related to axon guidance, and the spreading of the cells in a particular direction may be involved in growth cone steering of the axons [76]. However, the underlying cellular processes have not been fully elucidated. Also, while ES has been shown to enhance growth, the phenomenon of changes in cell migration from tissue body *in vitro* due to EF, which in turn may drive neurites to grow, has not been widely researched.

In addition, several works note directionality of neurite outgrowth with respect to the applied field. According to Patel and Poo, application of low PEMF on dissociated *Xenopus* embryonic neurons enhanced neurite outgrowth and the accelerated growth is observed in the direction of the cathode [42-44]. These results indicated that neurites grow in the direction of the flow of current between the electrodes, which is from anode to cathode. The flow of current in the media may cause movement of the ions within the solution in the same direction, which may prompt neurites to grow in the same path.

## CHAPTER III

### PURIFICATION OF SCHWANN CELLS FROM MIXED NEURONAL POPULATION

#### 3.1 Introduction

Dorsal root ganglia (DRG) are neural tissues which are found at the dorsal end of the spinal cord in vertebrates. DRG play a vital role in the transfer of sensory information from peripheral nervous system (PNS) to the appropriate integration center in the central nervous system (CNS) [19]. DRG contain different neural and non-neural cells that aid in transfer of sensory signals within the body. The main cell types within a DRG are neurons, Schwann cells (SC), and fibroblasts [19, 20]. Many researchers are interested in using SC for nerve injury treatment because they are the principal glial cells of the PNS and play a vital role in structural and functional recovery of injured nerves [58]. After peripheral nerve injury, SC, along with macrophages, proliferate and remove axon debris and they also produce various neurotrophic factors to promote and guide axon growth in the distal nerve stumps [59]. Transplantation of pure SC in autografts has shown improved recovery in injured nerves [4]. However, the contamination of SC with fibroblasts is an issue in these cases because the fibroblasts divide very rapidly and build protecting layers (epi-, perineurium) surrounding bundles of nerve fibers [60]. The

removal of the contaminating fibroblasts with minimal damage to the SC is a challenging problem. The number of rapidly dividing fibroblasts can be reduced by addition of antimetabolic drugs, such as cytosine arabinoside (Ara-C), to the cell culture medium or by maintaining serum-free primary cultures [61, 62]. Other methods to purify SC used complemented mediated cytolysis via specific enzymes [63]. The resultant purified SC percentage was about 95%. Studies by Yu- Quing Jin and Kreider used a method based on differential cell detachment giving 99% pure SC by treating the cells with multiple collagenase before culture[64, 65]. In another study, magnetic-activated cell separation (MACS) was used to purify SC, which gave 95% pure SC [11]. Many other studies have been performed for purifying SC using different methods in the past few decades [56, 60, 62-66, 69].

With the time required to enrich SC and potential damage to SC due to the addition of antimetabolic drugs, these methods are not cost effective for purifying SC on a very large scale for clinical applications. This chapter describes a simple, fast purification method to isolate SC from mixed neural population using the process of differential adhesion.

## 3.2 Materials and Methods

### 3.2.1 Materials

Fertilized eggs were obtained from Sunrise Farms, NY. F12K media, trypsin-EDTA and fetal bovine serum (FBS) were purchased from Sigma Aldrich and nerve growth factor (NGF 2.5s, host species: mouse) was obtained from BD Biosciences. Paraformaldehyde was obtained from Fisher (Cat #: T353-500), wetting agent Triton X-100 from Ricca Chemical Company (Cat #: 8698.5-16), sodium borohydride (Cat #: 102894) and bovine

serum albumin (BSA, Cat #: 180577) were purchased from MP Biomedicals. Primary monoclonal antibodies neurofilament marker 3A10 (host species: mouse, isotype: IgG1, Cat #: 3A10), Schwann cell marker 1E8 (host species: mouse, isotype: IgG1, Cat #: 1E8) and fibronectin marker B3/D6 (host species: mouse, isotype: IgG2a, Cat #: B3/D6). 3A10, developed by Thomas M. Jessell / Jane Dodd / Susan Brenner-Morton, 1E8, developed by Eric Frank, and B3/D6, developed by Douglas M. Fambrough were obtained from the Developmental Studies Hybridoma Bank developed under the auspices of the NICHD and maintained by The University of Iowa, Department of Biology, Iowa City, IA 52242. Secondary antibodies Alexa Flour 488 goat anti-mouse IgG1 (Cat #: A21121) and Alexa Flour 546 goat anti-mouse IgG2a (Cat #: A21133) were purchased from Molecular Probes. DNA label Hoechst 33342 (Cat #: H1399) was purchased from Life Technologies.

### 3.2.2 Isolation and culture

DRG were dissected from 9-day chick embryos. The DRGs were cleaned of excess tissue and dissociated using 0.25% trypsin in 1mM EDTA. The dissociated cells were counted using a hemacytometer and supplemented media (20% fetal bovine serum (FBS) in media (F12K)) was added to the cells to obtain a seeding density of  $7.5 \times 10^3$  cells/cm<sup>2</sup>, where each well had an area of 9.6 cm<sup>2</sup>. The surface of the wells was coated with collagen (rat type I in 0.02M acetic acid). Collagen was adsorbed to the surface of the well plate for 1 hr at room temperature at 150 µg/mL concentration in PBS. NGF supplemented media was added to the cells at 25 ng/mL concentration and cultured for 24 hrs at 37°C, 5% CO<sub>2</sub> environment, which constituted the mixed population of the cells.

The remaining cells were separated into two wells of an uncoated 6-well plate and incubated for 1, 2 or 4 hrs, at 37°C, 5% CO<sub>2</sub> environment, with the serum-supplemented media. After the time period, using microscopy, it was observed that some cells were adhered to the bottom of the surface of the well plate constituting the adherent population while other cells were floating in the media, which were the non-adherent population. The media was removed from the well plates and placed in a tube labeled 'non-adherent'. The adherent cells were removed by adding 0.5 mL trypsin in 0.5 mL PBS on the surface for 10 minutes. Then, the solution was removed to another tube labeled 'adherent'. After centrifugation, the supernatant was discarded. NGF-supplemented media was added to the cells, which were seeded on collagen-coated well of a 6-well plate and left for 24 hr at 37°C, 5% CO<sub>2</sub> environment. The seeding density of the adherent and non-adherent cell populations differed from experiment to experiment depending upon the number of cells obtained initially after dissociation of the DRG. The respective seeding densities for adherent and non-adherent cells were noted for each experiment and calculations were done accordingly.

### 3.2.3 Fixation and antibody staining

To fix the cells, 4% paraformaldehyde was freshly prepared by dissolving 0.4g of paraformaldehyde powder and 0.1 mL of 1M NaOH in 7 mL of water at 60°C. After the powder dissolved, 1 mL of 10X PBS was added to the solution and was left to cool at room temperature. Thereafter, 0.1 mL of 1M HCl was added to bring the pH up to 7.4. Finally, more tissue-culture water was added to bring the volume up to 10 mL. Paraformaldehyde was added to the cells and left at room temperature for 20 min. Paraformaldehyde was removed and cells were permeabilized using 0.1% Triton X-100.

Finally, sodium borohydride was used at 1 mg/mL in PBS to quench the aldehyde and reduce autofluorescence. Fixed cells were blocked using 3% BSA in PBS prior to antibody labeling. The primary monoclonal antibodies used were 3A10 (neurofilament marker, to label neurons) at 1:200 dilution ratio, 1E8 (SC marker) at 1:1000 dilution ratio and B3/D6 (fibronectin marker, to label fibroblasts) at 1:200. Labeling using two antibodies was done to observe the number of neurons and SC with respect to fibroblasts in the total population. Thus, fibroblast marker B3/D6 was combined with 3A10 to observe neurons and fibroblasts and with 1E8 for SC and fibroblasts. The antibodies were added to the cells and incubated at 4°C for 12 hr. After 3 washes, secondary antibodies Alexa Fluor 488 anti-mouse for the neurofilament and SC staining and Alexa Fluor 546 anti-mouse for fibronectin staining were added at 1:200 dilution ratio with similar combination as the primary antibodies. For nuclei labeling, DNA label H33342 was used at 1:100 dilution along with the secondary antibodies. The cells were incubated again for 12 hr at 4°C and imaged.

#### 3.2.4 Image analysis

Characterization of neurons and SC was performed from the images captured using microscopy. Images were taken at both 10x and 20x magnifications and analyzed for cell types in each sample type. The total number of cells per unit area was obtained for adherent and non-adherent populations for each time point using the particle count function in ImageJ and compared with the initial seeding density of the mixed population. Thereafter, characterization for each cell type was performed based on morphology and antibody labeling. Since SC and neurons have the same secondary antibody, images of both cell types were taken using fluorescein isothiocyanate (FITC, green) filter.

Therefore, SC and neurons could not be labeled simultaneously in a single image. The fibroblasts were imaged using rhodamine (red) and the cells using 4', 6-Diamidino-2-Phenylindole, Dihydrochloride (DAPI, blue) filter. The SC were labeled in a single image along with fibroblasts and DNA label, while the neurons were labeled in another image with fibroblasts and DNA label. The neurons, SC and fibroblasts labels having nuclei were considered for determining the cell type number. If there was a green or red label in the image that did not have a blue label associated with it, that label was not considered for analysis. Morphology of the cell type was also examined before regarding it as neuron, SC, fibroblasts.

The percentage of each cell type was determined with respect to the overall number of cells in the image using particle counting function in ImageJ. Cell number was represented as mean  $\pm$  S.D. The SC purity was derived from the calculation of the percentage of SC with respect to the total number of counted cells:

$$SC \text{ purity} = \frac{SC \text{ number}}{Total \text{ number of cells}} \times 100\% \quad (3.1)$$

The percentages of cells for neurons and fibroblasts were obtained in similar way as Eqn (3.1). Thus, for a single image, the percentages of neurons and fibroblasts were determined with respect to the total number of cells in that image, and similarly, the percentages of SC and fibroblasts were obtained with the total number of cells in that particular image.

### 3.2.5 Statistical analysis

Statistical analysis was done on the SC and neuron purity between 1, 2 and 4 hr using MATLAB. A non-parametric test called the Kruskal-Wallis test was employed to obtain significance between the data, where  $p < 0.05$  was considered significant.

## 3.3 Results

### 3.3.1 Characterization using cell morphology

The cells were distinguished based on morphology by microscopy. The neurons were round in shape. Moreover, these cells had a single long axon protruding from the cell body in a particular direction. In order to determine if a cell is labeled as neuron, a 20x magnification was performed. The green label tended to overlap with the blue label of the cell representing the labeling of the cell body and beginning of axon, as shown in Figure 3.1, A. On the contrary, the nuclei of the SC that were blue labeled were long and stretched, as shown in Figure 3.1, C. Figure 3.1, B and D represent the phase images of the corresponding labeled images.

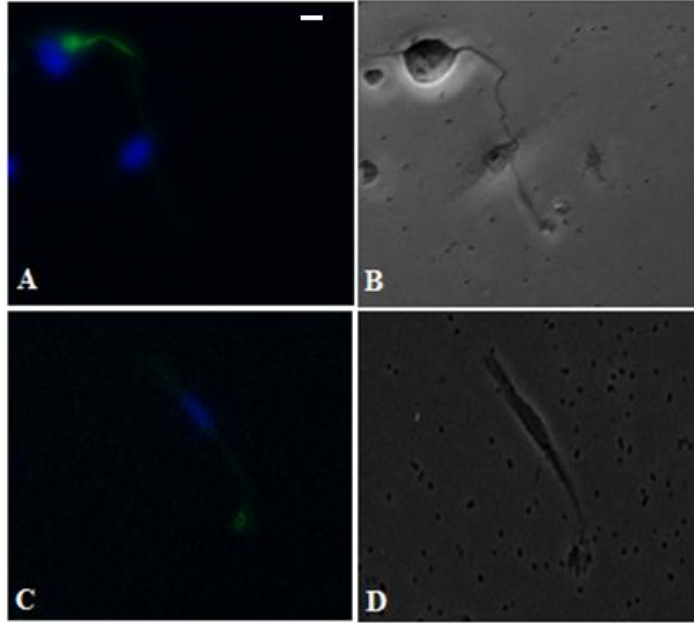


Figure 3.1: Fluorescent and phase images of neuron (A, B) and SC (C, D) at 20x magnification. The 20x magnification was done to distinguish neurons and SC. As seen in A and B, the neurons have round cell body, with a prominent round or oval shaped nucleus, with a single axon protruding out. The green label of the neurofilament has fused with the blue labeled nucleus, indicating the cell in a neuron. On the contrary, C and D show SC, with bipolar morphology and a cigar-shaped nucleus. Scale bars are same for all images as in (A), line (upper left) indicates a scale of 20 $\mu$ m.

### 3.3.2 Characterization using Antibody Staining

The analysis of the images to obtain the seeding densities at each time point and characterize cell types based on antibody labeling was performed using ImageJ. The percentages of neurons-fibroblasts and SC-fibroblasts for their respective images were taken with respect to the total number of cells in that image. The average cell percentage was determined for all the experiments and the standard deviation was calculated. After image analysis of all the populations, 35% of the cells in the mixed population were labeled as neurons, while 28% were labeled as SC and 37% were fibroblasts. About

0.02% of the cells were unlabeled. The cell densities of total cells and SC for mixed, adherent and non-adherent population for all the time points are listed in Table C.1 in Appendix C.

The average seeding density of the mixed population for 45 experiments was  $7.59 \pm 0.18 \times 10^3$  cells/ cm<sup>2</sup>. After 1 hr, the adherent population constituted about 32.8% of the total cells in the mixed population and non-adherent population contained 68.3% of the total cells in the mixed population. Moreover, no cells were labeled for SC in the adherent population and 71% of the total cells in the non-adherent population labeled for SC, as shown in Figure 3.2 (A-D).

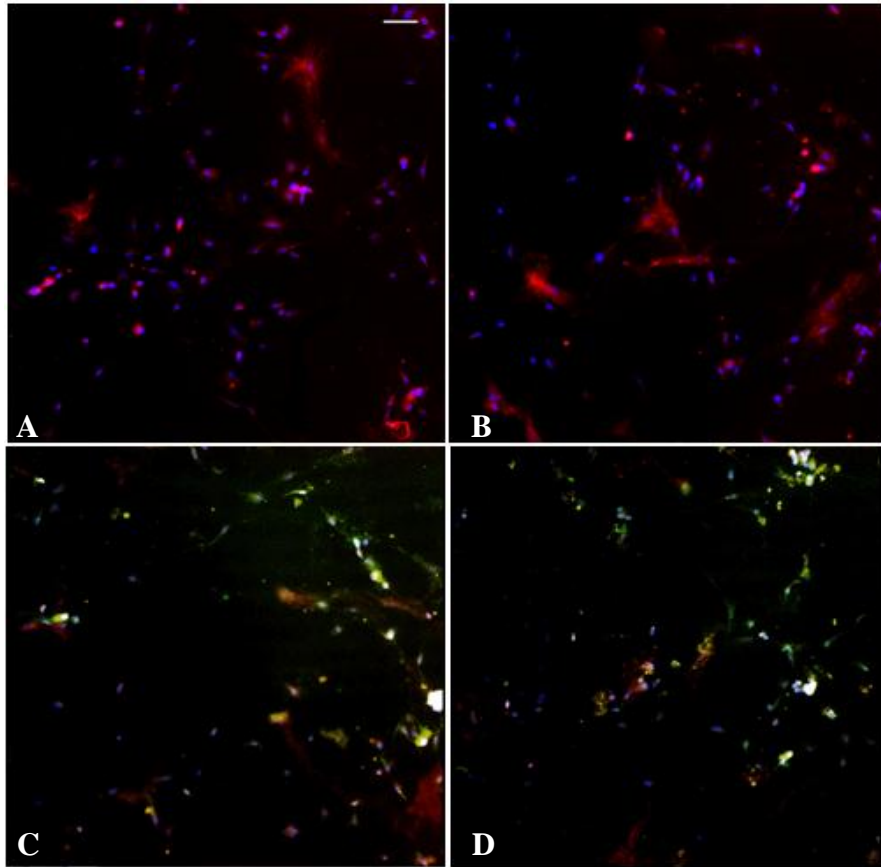


Figure 3.2: Fluorescent images of adherent (A, B) and non-adherent (C, D) populations at 1 hr time point. A, C represent fibroblasts (red) and neuron labeling (green) while B, D represent fibroblasts (red) and SC (green) labeling. Blue dots represent the nuclei of the cells. From A and B, it can be said that after 1 hr 38% of the total cells in mixed population adheres to the surface of the well plate while 68% of the total cells constitute the non-adherent population. The 1 hr time point also marks the separation of the fibroblasts constituting 87% of the total cells in the adherent population. Scale bars are same for all images as in (A), line (upper left) indicates a scale of 50 $\mu$ m

The total cell density of the adherent population increased from  $2.49 \pm 0.16 \times 10^3$  to  $4.91 \pm 0.16 \times 10^3$  cells/cm<sup>2</sup> after 2 hrs, which constituted 64.7% of the total number of cells in the mixed population. The most striking feature of the 2 hr time point is the adherence of SC, as shown in Figure 3.3, B. Although there was some fibroblast contamination, 98% of the total cells in the adherent population comprised of SC. No cells labeled for SC in non-adherent population.

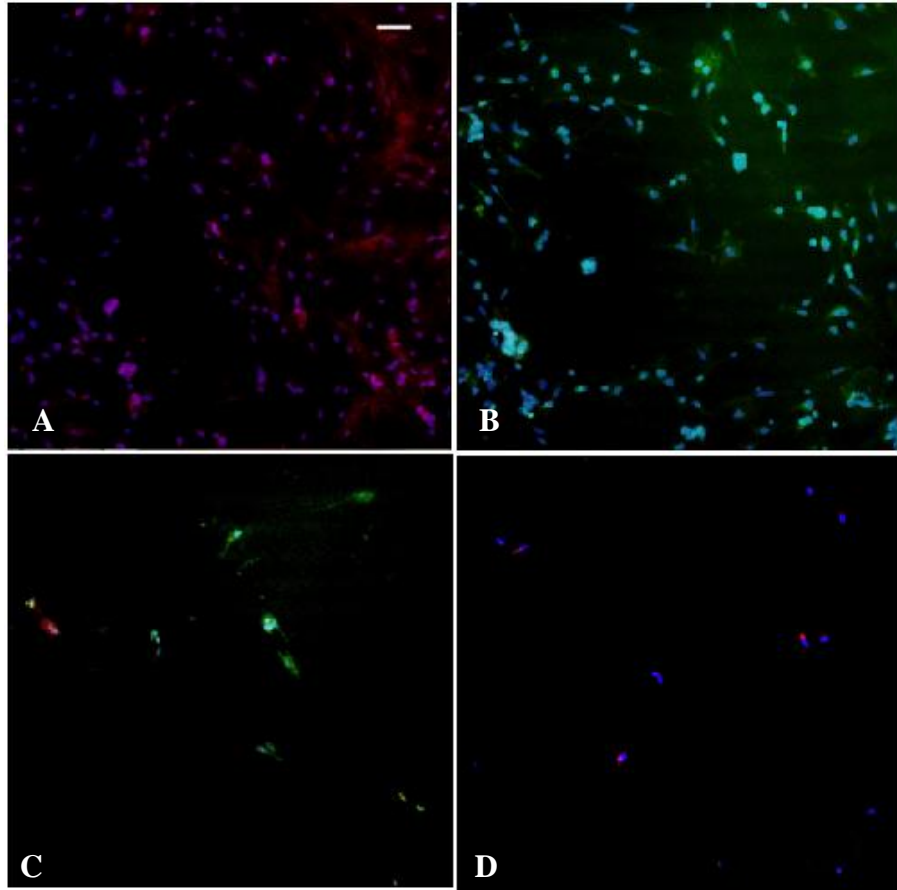


Figure 3.3: Fluorescent images of adherent (A-B) and non-adherent (C-D) populations at 2 hr time-point. A, C represent fibroblasts (red) and neuron labeling (green) while B, D represent fibroblasts (red) and SC (green) labeling. Blue dots represent the nuclei of the cells. From A and C, it can be said that after 2 hrs the number of adherent cells increased from 38% to 65%. Also, as indicated in C, 98% of the total cells in the adherent population label for SC with only 1.2% fibroblast contamination (the rest of the cells did not label for any cell type). Scale bars are same for all images as in (A), line (upper left) indicates a scale of 50 $\mu$ m.

After 4 hrs, 95.5% of the total cells in the mixed population had adhered to the surface of the well plate with only 0.05% cells in the non-adherent population, which did not label for any neurons, SC or fibroblasts. In the double labeled image of SC and fibroblasts, SC population was found to be 93% and the other 7% were fibroblasts, as shown in Figure 3.4. Hence after 4 hr, all the differentiated cell types had adhered to the surface of the well plate.

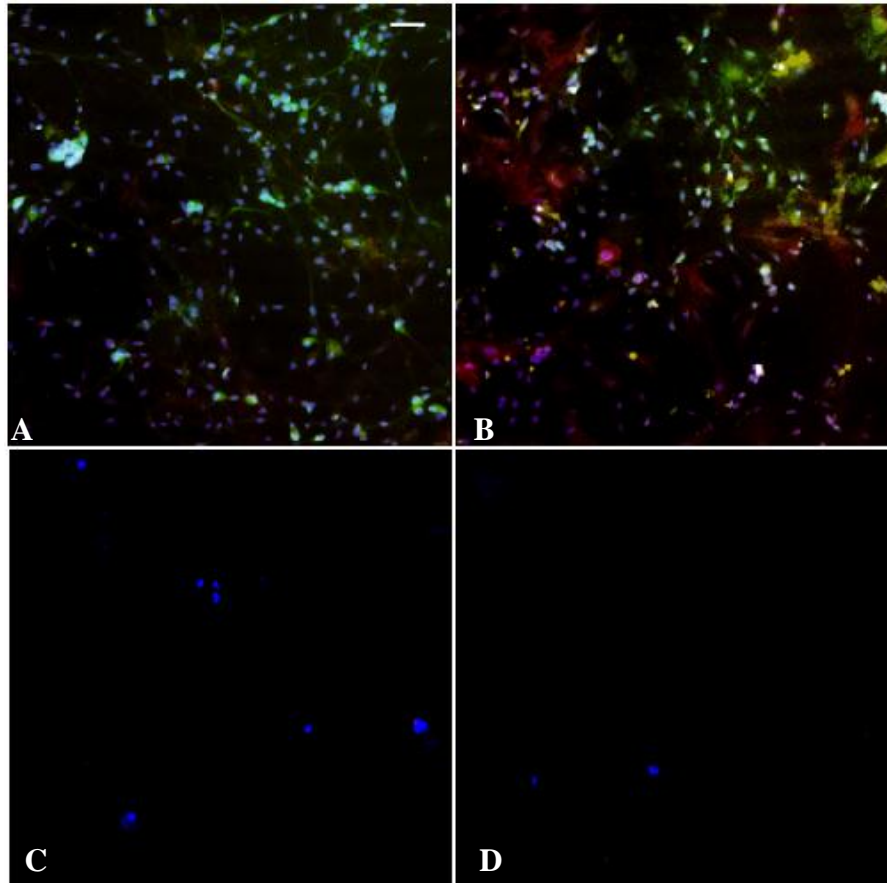


Figure 3.4: Fluorescent images of adherent (A-B) and non-adherent (C-D) populations at 4 hr time-point. A, C represent fibroblasts (red) and neuron labeling (green) while B, D represent fibroblasts (red) and SC (green) labeling. Blue dots represent the nuclei of the cells. After 4 hrs, 95% of the total cells adhered to the surface with only 5% non-adherent cells in the non-adherent population. No cells labeled for neurons or SC in the non-adherent population. About 0.2% cells labeled for fibroblasts in the non-adherent population after 4 hrs (C, D). Scale bars are same for all images as in (A), line (upper left) indicates a scale of 50 $\mu$ m

Figure 3.5 illustrates the changes in the cell densities of total cells and SC for mixed, adherent and non-adherent populations for 1, 2 and 4 hr time points. From the figure, it can be observed that the cell density of total cells increased in the adherent population with increase in duration of culture. Also, the cell density of SC increased in adherent population after 2 hrs constituting 98% of the total number of cells. Thereafter, the SC

cell density drops to 93% of the total cell population due to increased adherence of other cell types like neurons and fibroblasts.

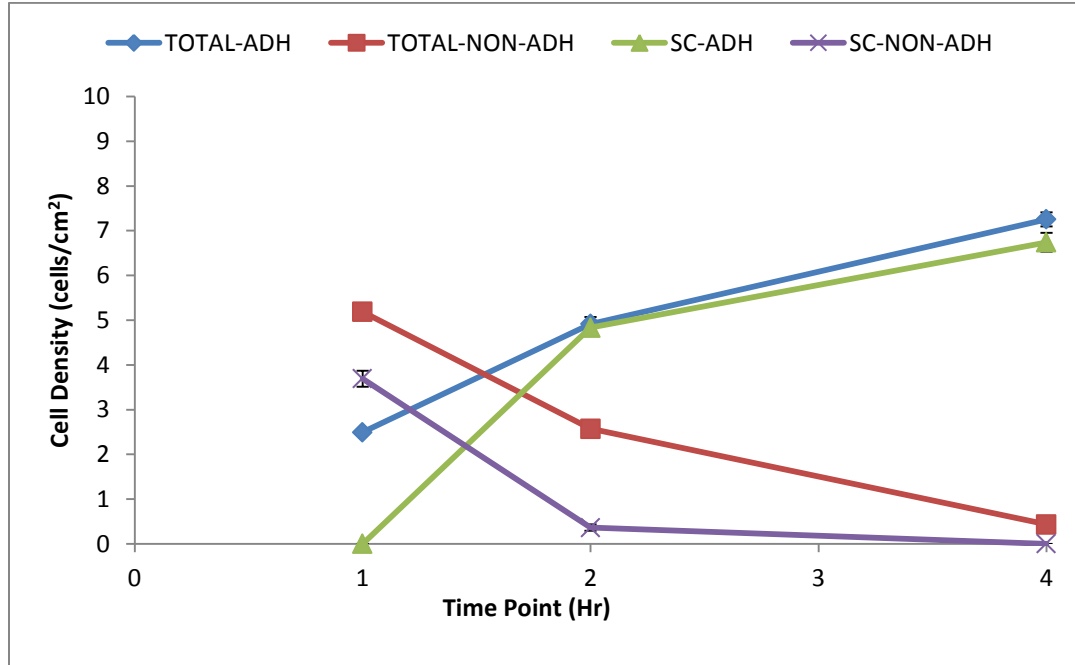


Figure 3.5: Graphical representation of average cell density  $\pm$  standard deviation of cells in adherent and non-adherent populations for 1, 2 and 4 hrs time points. The number of cells increased in the adherent population as the time increase. After 2 hr, 98.3% of the total cells in adherent population labeled for SC.

Statistical analysis was performed on all data using non-parametric Kruksal – Wallis test, which is equivalent to one-way ANOVA for non-parametric data. Graphical representation of the average total cell densities at each time point for mixed, adherent and non-adherent populations is shown in Figure 3.6. Significant differences were observed in the average cell densities between mixed population and non-adherent population for all the time points ( $p < 0.05$ ). A statistical decrease was observed in the cell density for the non-adherent population increases in time ( $p < 0.05$ ). No statistical significance was observed between mixed and adherent population for 4 hr time point ( $p > 0.05$ ).

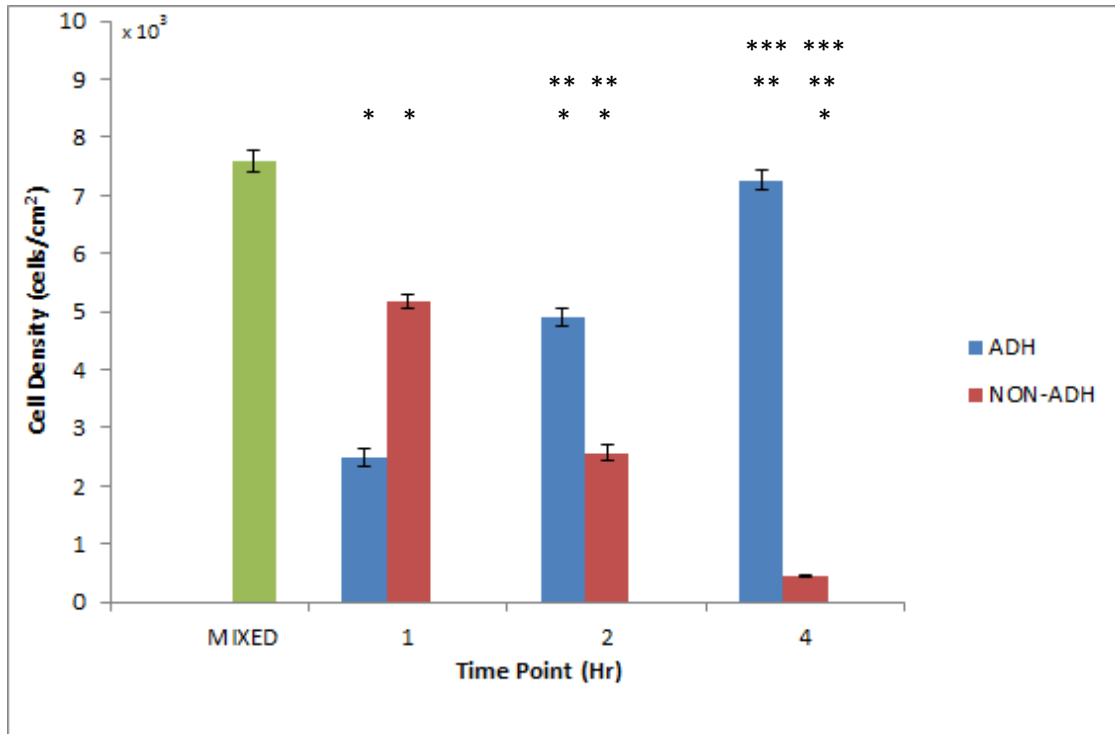


Figure 3.6: Graphical representation of average cell density  $\pm$  standard deviation of mixed, adherent and non-adherent populations for 1, 2 and 4 hrs time points. For 2 hr and 4 hr time points,  $n > 43$ , for the mixed population,  $n = 45$  and for 1 hr time point,  $n = 28$ . Statistical significance is indicated by \*, \*\* and \*\*\* which represent differences from mixed population, 1h and 2h time points, respectively. ( $p < 0.05$ ).

### 3.4 Discussion

Many protocols have been developed for the purification of SC from embryonic [66, 67], and adult mice [68-70]. The percentage of purified SC populations obtained in these studies range from 85% [68, 70] to 99% or more [64, 66]. Some of these methods have mentioned the contamination of SC population with fibroblasts [60, 63] and have devised different methods to keep the fibroblast population in control, but their limitation is that although the treatment of neural cell cultures with antimetabolic agents like arabinofuranosyl cytidine or cytosine arabinoside diminished fibroblasts contamination, they are also harmful to SC function [72]. Also, from a clinical standpoint, the usage of

antibodies with magnetic beads, flow cytometry, etc. to purify SC on a large scale would not be economical. The present study was completed to demonstrate a simple method of isolating SC based on differential adhesion with reduced fibroblast contamination without the use of any exogenous materials. The study also exhibited SC and neuron purification based on time points.

The results obtained from characterization of the cell types based on morphology show that neurons have a round structure, with a single long axon protruding from the cell body whereas, SC are bipolar and flat. The nuclei of the neurons were round and for SC, they were elongated, similar to another study, which has reported SC to be bipolar with cigar shaped nuclei [65]. The SC were mostly bipolar in shape. The fibroblasts did not seem to have any defined shape and were flat with oval shaped nuclei, as reported by Vroemen [65].

The cells began to adhere to the surface of the well-plate after 1 hr culture while after 4 hrs, all of the cells from the mixed population adhered to the surface leaving only 5% cells in the non-adherent population. Moreover after 4 hrs, none of the cells in the non-adherent population contained any neurons or SC (0.2% fibroblasts) indicating that 4 hrs is sufficient for neurons, SC, and most of the fibroblasts to adhere to the surface. However, each cell type separated from the mixed population at different time intervals. During cell culture *in vitro*, fibroblasts stick to culture vessels faster than SC. After culturing the mixed population of cells for 1 hr, the fibroblasts began to adhere to the surface of the well plate while the neurons and SC were comprised in the non-adherent population (Figure 3.2). This phenomenon has been observed previously in collagen-coated surfaces [73]. After 2 hr, the adherent population with average cell density of 4.91

$\pm 0.16 \times 10^3$  cells/cm<sup>2</sup> consisted of 98.3% SC (average density of  $4.83 \pm 0.11 \times 10^3$  cells/cm<sup>2</sup>) indicating that the SC begin to separate from the mixed population within 1-2 hr after culture (Figures 3.3, 3.5). After 4 hr, all the cell types had adhered to the surface (Figure 3.4). Hence, the present study shows that 2 hr is the optimal time examined for differential attachment to purify SC with least fibroblastic contamination. The difference in time taken by a particular cell type for adhesion is likely due to differential adhesion. Thus, the results of the present study demonstrate that among the three primary cell types in the DRG: fibroblasts, SC and neurons, the fibroblasts adhered the fastest, followed by SC, and finally neurons.

### 3.5 Conclusion

A simple and effective method was designed to separate the types of cells within chick DRG. At least three cell types were found in the DRG: fibroblasts, SC, and neurons. Characterization of each cell type was performed using morphology and immunostaining. The isolation and cell detachment of each cell type was observed with respect to time. It was found that as the time passed, more cells begin to adhere to the well-plate surface and after 4 hrs  $7.25 \pm 0.16 \times 10^3$  cells/cm<sup>2</sup> adhered to the bottom of the well-plate, constituting 95% of the total mixed cell population. Also, it was observed that fibroblasts adhere to the surface fastest, followed by SC and finally neurons. Culturing the mixed population for 2 hr gave 98.3% pure SC in the adherent population. Finally, no cells were labeled for neurons and SC in the non-adherent population with only 0.2% fibroblasts, indicating that after 4 hrs almost all the cell types had adhered to the surface.

## CHAPTER IV

### EFFECTS OF LOW AND HIGH FREQUENCY STIMULATION ON NEURITE GROWTH, DIRECTIONALITY AND DRG CONDUCTIVITY

#### 4.1 Introduction

The application of external stimulation in the form of electric fields (EF) has been known to impact neural growth and guidance *in vivo* as well as *in vitro*. Various studies have demonstrated that use of different external fields like direct current (DC), alternating current (AC), pulsed electromagnetic fields (PEMF) influence neurite growth [2-5, 40-47]. In fact, application of ES for a short duration of 10 mins has been shown to significantly improve growth in neurites [2]. Also, studies have shown that the neurites have preferential and increased growth towards the cathode of an externally applied EF [43, 44]. Electric stimulation (ES) can also have negative impact on nerve tissues. Experiments have been conducted where *Xenopus laevis* embryos were exposed with high EF (above 1 kHz) resulting in various abnormalities in the neural tube [51]. Similar observations were made in chick embryo neural development [49-51].

Most of the ES studies have used DC in generation of EFs. Recent works on use of AC stimulation for enhancing neural properties have shown that AC stimulation is capable of

producing EFs of greater magnitudes over an increased distance than DC stimulation at the same current magnitude [7]. An additional advantage of AC stimulation is decreased power consumption, which makes it more suitable for large scale therapeutic stimulation. The results of the above mentioned studies indicate that application of ES in any form can have a large impact on the biological characteristics of nerve tissues. However, little is known about the mechanism that causes the biological properties of tissues to change. One of the factors that influence such changes is the bioimpedance of the tissue. Any biological tissue has been modeled as having a capacitive component and a resistive component [53, 54]. Tissues can be modeled as resistor–capacitor circuit in different combinations. The usage of DC, low frequency AC or high frequency AC fields tend to have different effects on the tissue due to the capacitive properties of the tissue. Thus, the impedance (and thereby, the conductivity) of the tissue is frequency dependent, which further impacts the EF that penetrates the tissue surface. The present work quantifies several biological properties of neural tissue like neurite outgrowth, cell spreading, cell viability and neurite density with respect to input frequency at a constant input voltage and current in a non-uniform EF

## 4.2 Materials and Methods

### 4.2.1 Materials

Fertilized eggs were obtained from Sunrise Farms, NY. F12K media, trypsin-EDTA and fetal bovine serum (FBS) were purchased from Sigma Aldrich and nerve growth factor (NGF, host species: mouse) was obtained from BD Biosciences. Sylgard 184 silicone elastomer kit (Cat #: DC4056134) and Sylgard 186 silicone elastomer kit (Cat #:

DC4026144), which contains the Sylgard 184 and 186 silicone elastomer base and Sylgard 184 and 186 silicone elastomer curing agent, respectively, were obtained from Dow Corning Silicones. Platinum foil (Cat #: 11509, 0.1mm thick, 99.99% pure) was acquired from Alfa Aesar. Paraformaldehyde was obtained from Fisher (Cat #: T353-500), wetting agent Triton X-100 from Ricca Chemical Company (Cat #: 8698.5-16), sodium borohydride (Cat #: 102894) and bovine serum albumin (BSA, Cat #: 180577) were purchased from MP Biomedicals. Primary monoclonal antibodies neurofilament marker 3A10 (host species: mouse, isotype: IgG1, Cat #: 3A10), Schwann cell marker 1E8 (host species: mouse, isotype: IgG1, Cat #: 1E8) and fibronectin marker B3/D6 (host species: mouse, isotype: IgG2a, Cat #: B3/D6). 3A10, developed by Thomas M. Jessell / Jane Dodd / Susan Brenner-Morton, 1E8, developed by Eric Frank, and B3/D6, developed by Douglas M. Fambrough were obtained from the Developmental Studies Hybridoma Bank developed under the auspices of the NICHD and maintained by The University of Iowa, Department of Biology, Iowa City, IA 52242. Secondary antibodies Alexa Flour 488 goat anti-mouse IgG1 (Cat #: A21121) and Alexa Flour 546 goat anti-mouse IgG2a (Cat #: A21133) were purchased from Molecular Probes. DNA label Hoechst 33342 (Cat #: H1399) was purchased from Life Technologies. Live/dead stains Calcein AM (Cat #: ALX-610-026-M001) was obtained from Enzo Life Sciences and Ethidium Homodimer (Cat #: E1169) from Life Technologies.

#### 4.2.2 Tissue culture

The DRG were harvested from E9 chick embryos, placed on circular glass coverslips (13mm) with minimal fluid (~100  $\mu$ l) and incubated at 37°C, 5% CO<sub>2</sub> for 4hr to encourage attachment. The coverslips were acid-etched prior to use. This process starts

by washing the coverslips with soapy water and blow drying them with air. The coverslips were immersed in 9:1 H<sub>2</sub>SO<sub>4</sub>:H<sub>2</sub>O<sub>2</sub> for 20 mins, washed in deionized water and submerged in absolute ethanol. Thereafter, the coverslips were blow dried completely before use. Also, the bottom side of each coverslip was marked using a diamond tip pen, which was used to indicate the field alignment. The coverslips were treated with collagen (rat type I in 0.02M acetic acid) overnight at 150 µg/mL concentration in PBS, at 4°C. The additional coating helped the DRG to attach to the surface of the coverslip. The DRG containing coverslips were cultured for a total of 24 hr in growth medium containing Ham's F-12K and 20% FBS, with NGF at 25 ng/mL concentration, at 37°C, 5% CO<sub>2</sub>. One coverslip was placed in each well of a 24 well plate and covered with 0.5 mL of NGF-supplemented media. After 24 hr, the pre-stimulation images were taken for all the cultured DRG.

#### 4.2.3 Electric chamber fabrication

The rectangular silicone chamber was fabricated to stimulate the DRG using Sylgard elastomers. The Sylgard 184 and 186 bases were mixed with their respective curing agents at 9:1 ratio in a flat-bottomed plastic container to obtain 5 mL volume for each elastomer. The elastomers 184 and 186 were combined together at 1:1 ratio to obtain 10 mL volume of the mixture and placed in a vacuum desiccator for 10 mins to remove the air bubbles in the elastomer mixture. Thereafter, the mixture was spread out evenly with 1 cm thickness on a mold with a 7 x 3 cm void in the center and allowed to gel at 37°C overnight. The gel was removed slowly from the mold and copper wires were inserted from the left and right parts of the chamber. Platinum sheets were cut into 3 x 1 cm rectangular shapes and soldered to the copper wire on either side of the chamber. The

chamber was then washed with DI water and soaked in 70% ethanol for 15 mins while being gently shaken. The chambers were rinsed with DI water and soaked in acetone for 15 mins on the shaker. After that, the chambers were rinsed in ultra-pure DI water and dried in the oven at 60°C for 1 hr. While warm, the chambers were placed firmly on top of acid-etched glass slides. The glass slides with the chamber on top were wrapped in a Kimwipe, placed in a sterilization pouch, and autoclaved. The cleaning procedure for the chambers was followed before each experiment.

#### 4.2.4 Electric stimulation

The cultured DRG were stimulated at different frequencies in the electric chamber. After autoclaving the chambers, two points were marked on the bottom of the glass slide, at a distance of 0.5 cm from each electrode using a marker. These points represented the positions of the coverslips at the anode and cathode – designated as position A and position C, respectively. The labeling was done to maintain a constant distance of the DRG from the electrode to expose the tissue to consistent EFs.

The chamber was filled with 1.5mL of PBS and two DRG containing coverslips were placed on positions A and C, as shown in Figure 4.1. A sinusoidal input was passed between the electrodes at 4 different frequencies - 20Hz, 200Hz, 1MHz and 100MHz – at constant amplitude of 2.5 V<sub>p-p</sub>. All stimulations were done for 1hr. The voltages at positions A and C were measured by connecting two wires at A and C with the oscilloscope. To determine the current in the system for each frequency, a low resistor of value 98.3Ω was connected with the cathode. The voltages were measured at four points for all frequencies, as shown in Figure 4.2(A-E).

$V_{src}$  = Input Voltage

$V_{high}$  = Voltage at position A

$V_{low}$  = Voltage at position C

$V_{rsens}$  = Voltage at the sensor (resistor)

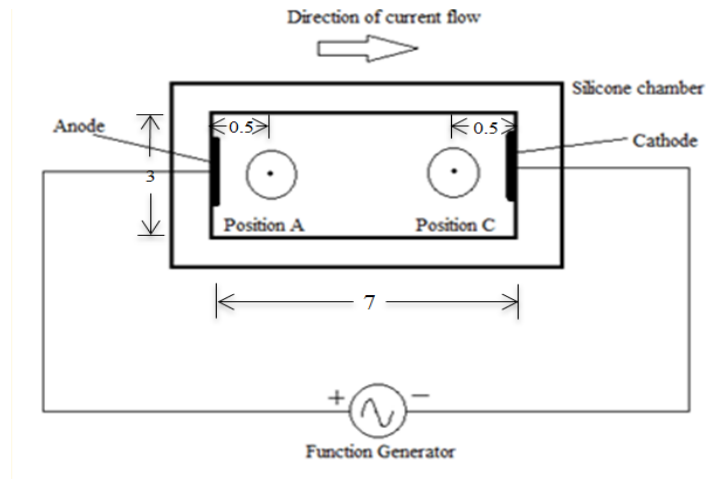


Figure 4.1: Schematic representation of the ES chamber. The units of the distances are in cm. The anode and cathode are made of platinum sheets which is connected with the function generator that supplies the input sinusoidal signal at  $2.5 V_{p-p}$ , at 20Hz, 200Hz, 1MHz and 20MHz. Positions A and C represent the position of the DRG containing coverslip. The chamber is filled with PBS and the flow of charges through PBS on application of EF is from anode to cathode. Position A is exposed to higher EF intensity than position C due to resistance of the PBS and the DRG, the system acts as a voltage divider circuit. Thus, net resistance at position C is more than position A, which results in less intensity.

The current in the system,  $I_{rsens}$  for each frequency was calculated by:

$$I_{rsens} = \frac{V_{rsens}}{R_{sens}} \quad (4.1)$$

Where  $R_{sens} = 98.3\Omega$ .

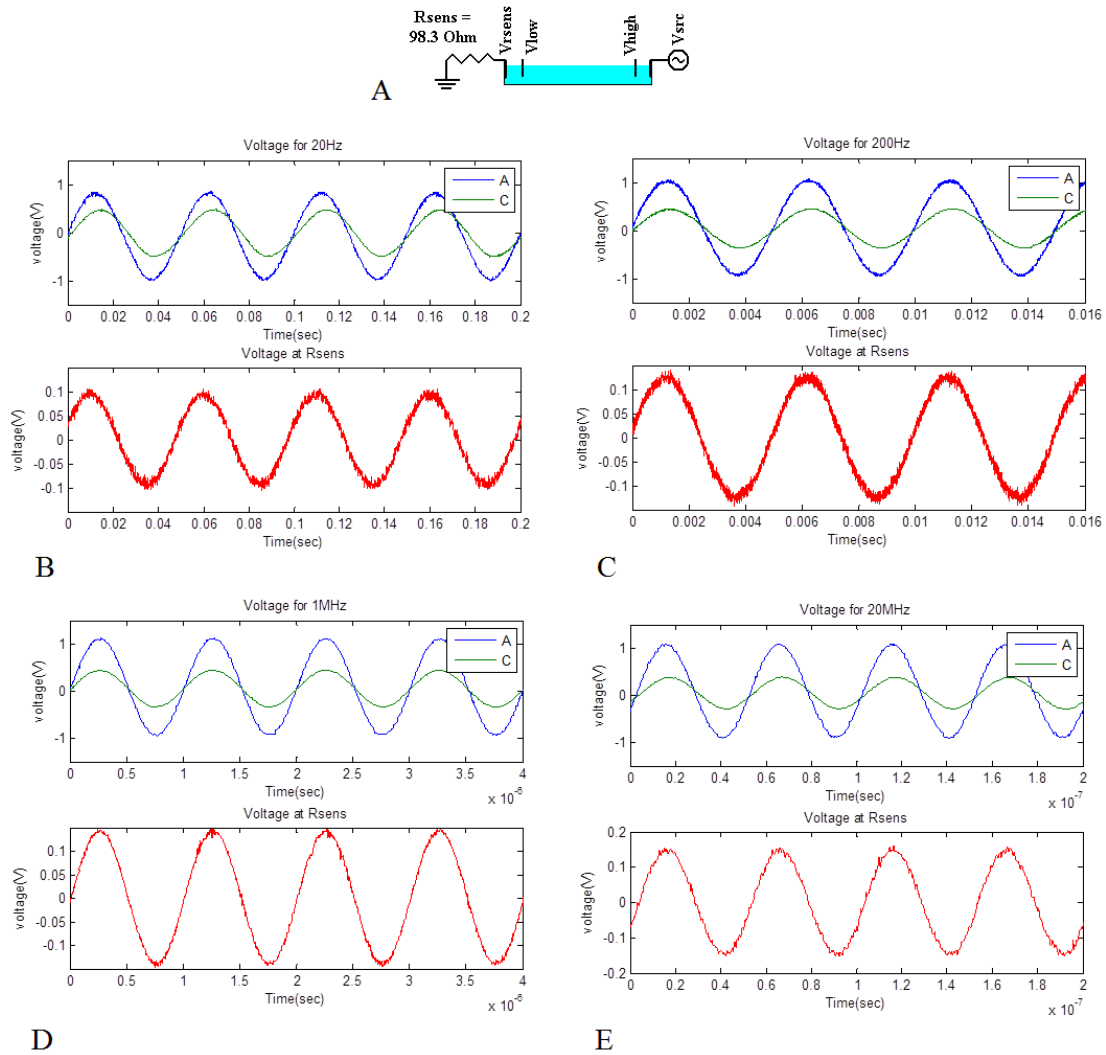


Figure 4.2: Voltage measured at positions A and C for 20Hz, 200Hz, 1MHz and 20MHz. This experiment was done to ensure that the voltage and current passing through the DRG at different frequencies was the same, and that frequency was the only variable. Figure A represents the circuit diagram of the experiment, where a resistor  $R_{sens} = 98.3\Omega$  was placed to near the cathode. The voltage across  $R_{sens}$  was used to calculate the current flow in the system using Ohm's law. (B-E) shows the voltage at positions A and C, and  $R_{sens}$  for all frequencies of stimulation. Results showed 3.7% shift in the voltages across all the frequencies, which is negligible.

Table 4.1: Voltage and current measurements in the ES chamber for different frequencies at positions A and C

<b>Freq (Hz)</b>	<b>position A (V)</b>	<b>position C (V)</b>	<b>V<sub>rsens</sub>(V)</b>	<b>I<sub>rsens</sub>(A)</b>
20	2.04	0.9	0.2	0.002
200	2.08	0.9	0.3	0.003
1000000	2.10	0.8	0.3	0.003
20000000	2.12	0.8	0.3	0.003

Sham exposed controls were examined for each frequency where the DRG containing coverslips were placed in the chamber for 1hr, in PBS with no electric stimulation. The controls were tested to ensure that the changes in the tissue were due to the direct effect of stimulation. Following stimulation, the DRG were cultured for 24hr in NGF-supplemented growth media.

#### 4.2.5 Fixation and staining

Post-stimulated DRG were fixed using 4% paraformaldehyde, which was freshly prepared by dissolving 0.4g of paraformaldehyde powder and 0.1M NaOH in 0.7mL of water at 60°C. The solution was cooled at room temperature after adding 1mL of 10x PBS and the pH was brought to 7.4 by adding 0.1M HCl. Water was added to bring the volume to 10mL. The DRG were exposed to paraformaldehyde for 20 mins and were rinsed with PBS two times to remove any residual aldehyde. The tissues were permeabilized with 0.5% Triton X-100. Freshly prepared sodium borohydride was added

to quench any remaining aldehyde. Finally, 3% BSA was used as a blocking agent, to restrict non-specific binding of the antibodies.

*Antibody Staining:* After fixation, a neurofilament marker monoclonal primary antibody 3A10 was added to the DRG, at a concentration of 1:200 in 1x PBS. The DRG were incubated overnight at 4°C. After that, the secondary antibody was added to the DRG, diluted at 1:200 in 1x PBS, and incubated for 3hr at 37°C. To label the nuclei, H33342 was added along with the secondary antibody at 1:1000 dilution.

*Viability test:* The viability was investigated using 4mM calcein AM and 2mM ethidium homodimer. The concentrations of the solutions were taken as 10µM and 4µM for calcein AM and ethidium homodimer, respectively. The solutions were diluted with 1xPBS from the stock concentration to their respective working concentrations. The solutions were then mixed with DNA stain H33342. Approximately 200µl of the mixed solution was placed over the coverslips. The coverslips were incubated at room temperature for 45 mins, and then imaged.

#### 4.2.6 Image analysis

The images were captured using Carl Zeiss inverted fluorescent microscope. Phase images were taken for pre-stimulated samples using 5x magnification. Fluorescent mosaic images (4x4) were taken for all the post-stimulated DRG samples to cover the entire area of neurite growth and cells. The images were analyzed for length of the longest neurite, distance of the furthest cell from the DRG body, cell viability, and density of neurite growth with respect to the electric field. Axiovision 4.8 image processing software, ImageJ and MATLAB were used for image analysis.

#### 4.2.6.1 Neurite growth

The growth of the neurite was determined by obtaining the difference between the length of longest neurite in pre-stimulated and post-stimulated images. The length of the longest neurite was measured by drawing two concentric circles on the DRG – the inner circle representing the radius of the DRG body and the outer circle representing the tip of the longest neurite. The inner and outer radii for pre-stimulated images were taken as  $i_1$  and  $O_1$ , and for post-stimulated images,  $i_2$  and  $O_2$ , as shown in Figure 4.3A. The growth of the neurite was calculated using the following formula:

$$Growth = (O_2 - i_2) - (O_1 - i_1) \quad (4.2)$$

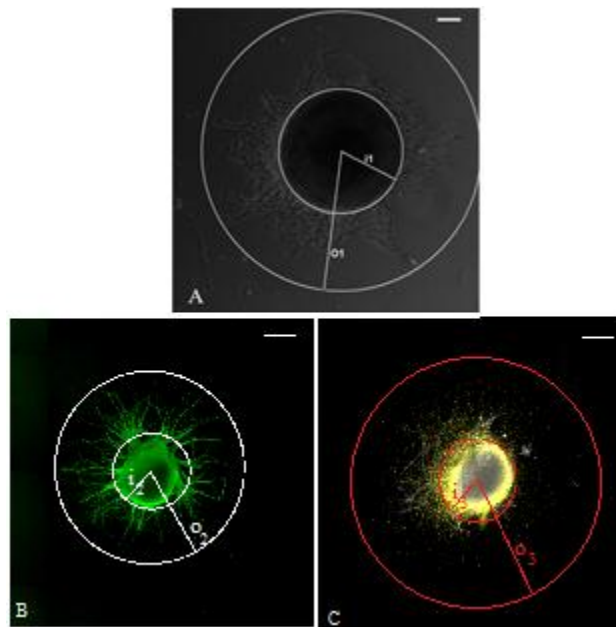


Figure 4.3: Measurement of neurite length and cell distance. Concentric circles are drawn around the DRG body and the tip of the longest neurite (B) or the farthest cell (C). (A) Pre-stimulated image, with  $i_1$  and  $O_1$  as the inner and outer radius of the circles; (B-C) post-stimulation fluorescent images for neurites and cells. The length of the longest neurite and the distance of farthest cell were calculated using Eqns. 4.2 and 4.3. Scale bar in (A) is 100  $\mu\text{m}$  and in (B-C) are 500  $\mu\text{m}$ .

#### 4.2.6.2 Cell spreading from DRG body

The effect of electrical stimulation on movement of the cells from the DRG body was determined. This analysis quantified the spreading of the cells in stimulated samples and compared it to control samples. It determines how far the cells have moved, with respect to the length of the longest neurite. The furthest cell was noted using nuclei labeling. The distance of the furthest cell was measured using the same procedure as the length of the longest neurite - the inner circle representing the radius of the DRG body ( $i_3$ ) and the outer circle representing the distance of the cell furthest away from the DRG body ( $O_3$ ), as shown in Figure 4.3B.

$$L_C = (O_3 - i_3) \quad (4.3)$$

Where  $L_C$  is the distance of the furthest cell from the DRG body.

Since the pre-stimulated images are not stained for cell bodies, only post-stimulated images were considered for this analysis. In order to compare the distance of the furthest cell from the length of the longest neurite, the ratio of the position of the cell to the length of the longest neurite was taken. It must be noted that for the ratio, the length of the longest neurite is considered. The length of the longest neurite in the post-stimulated image was determined by:

$$L_N = (O_2 - i_2) \quad (4.4)$$

Where  $i_2$  is the radius of the DRG body, and  $O_2$  is the radius of the circle representing the length of the longest neurite.

The cell spreading ratio was determined by using the following formula:

$$CS = \frac{L_C}{L_N} \quad (4.5)$$

If the value of CS is greater than 1, the distance of the cell spreading is further than that of the longest neurite; if it is less than 1, the length of the neurite is more than the furthest cell; and if it is equal to 1, the distance of the furthest cell is same as the length of the longest neurite. The ratio was determined separately for positions A and C, as well as for sham control.

#### 4.2.6.3 Cell viability

The quantification of cell viability after exposure to stimulation was done by determining the % cell viability for stimulated samples of all frequencies, at positions A and C, and comparing it with the controls. The original TIFF image was represented in MATLAB as a 2D matrix. The image was converted into binary with threshold 0.3. The number of white pixels was counted for the live and dead stain grey scale images. A variable 'count' was defined, which was incremented by 1 when the corresponding pixel had intensity value equal to 0, thereby counting number of white pixels in the image.

The % cell viability was determined by:

$$\% Viability = \frac{\text{No. of pixels in live stain}}{\text{No. of live stain} + \text{No. of pixels in dead stain}} \times 100\% \quad (4.6)$$

#### 4.2.6.4 Neurite density

The density of neurite growth with respect to the direction of current flow was determined. MATLAB and ImageJ were used for the quantification of neurite density for all the frequencies of stimulation. To measure density, the raw TIFF image was loaded in

ImageJ. The DRG body was traced using the ellipse option and removed. The new image now contained only the neurites. The image was converted to binary image, with threshold of 0.3. The original image is shown in Figure 4.4A. The image was zoomed and the area of the DRG was cropped so that all the neurites are enclosed in the new image and the center of the DRG body is the center of the zoomed image, as shown in Figure 4.4B. The x- and y- coordinates of the center pixel was determined using ImageJ and the image was split into two equal parts along the y axis, as shown in Figure 4.4 (C-D). One half is the anode facing side of the DRG while the other is the cathode facing side. The intensity of white pixels in each half was measured using MATLAB. A variable ‘count’ was defined to keep track of the number of white pixels (see Appendix A, Code 2). Thus, the value of ‘count’ gave the number of white pixels in each half of the image. The density ratio,  $D$ , of neurites was calculated by:

$$D = \frac{count_C}{count_A} \quad (4.7)$$

where  $count_C$  is the no. of white pixels in the image half facing cathode,  $count_A$  is the no. of white pixels in the image half facing anode. If  $D > 1$ , the density of pixels with neurofilament labeling was towards the cathode, if  $D = 1$ , labeling was equally distributed and if  $D < 1$ , the density was towards the anode.

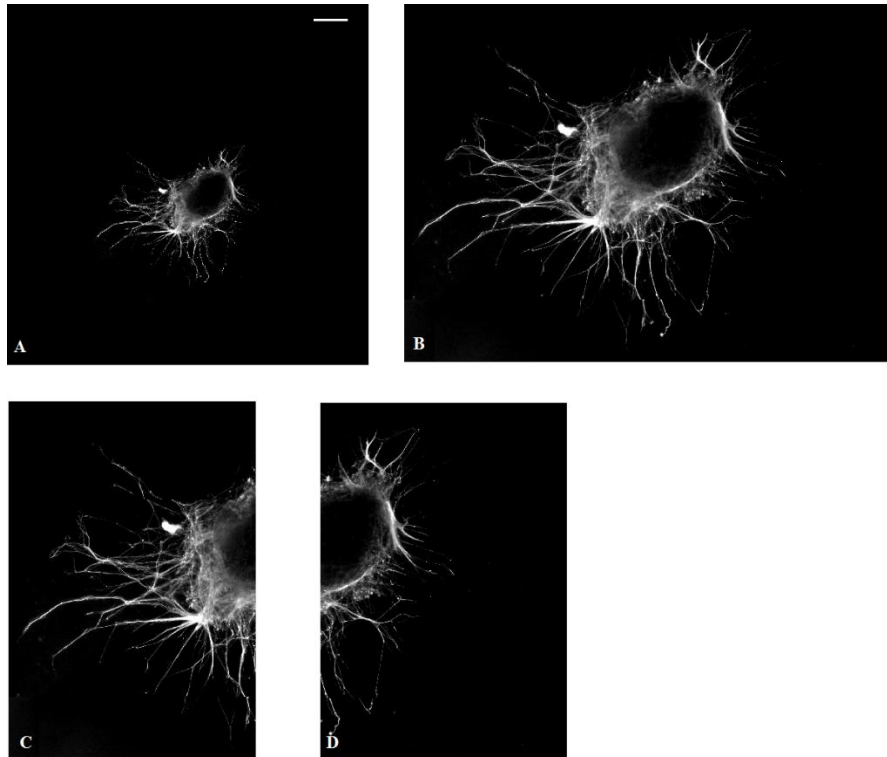


Figure 4.4: Diagram of the density measurement method. The original image is shown in A. The DRG body and the surrounding neurites are zoomed in and cropped (B) to reduce the background. The center pixel x and y coordinates are determined and the image is split into two equal parts (images C and D). The number of white pixels in each half is counted and the ratio of cathode to anode (D) is considered for analysis. If D is greater than 1, then the neurites are denser towards the cathode.

#### 4.2.6.5 Neurite directionality

The orientation of the neurite growth towards anode or cathode was quantified using polar plots. One hundred longest neurites from each image were considered for directionality analysis, using the 50 longest for each half of the image. The neurites were traced using ImageJ to determine the length, which was represented as  $r$ . The angle of the neurite tip from the center of the DRG body was measured, and denoted as  $\theta$ . The polar coordinates of the tip of each neurite ( $r, \theta$ ) were plotted as points in polar plots with  $10^\circ$  intervals using MATLAB (see Appendix A, Code 3). The polar plot was divided into 4

quadrants, as shown in Figure 4.5; quadrant 1 was facing the cathode while quadrant 3 was facing the anode. The red stars represent neurite tips facing the anode while the blue circles represent tips facing cathode. Each point on the polar plot represents the angle and length of a group of 75 neurite tips with a standard deviation of  $\pm 2.5^\circ$  and length deviation of  $\pm 10\mu\text{m}$ .

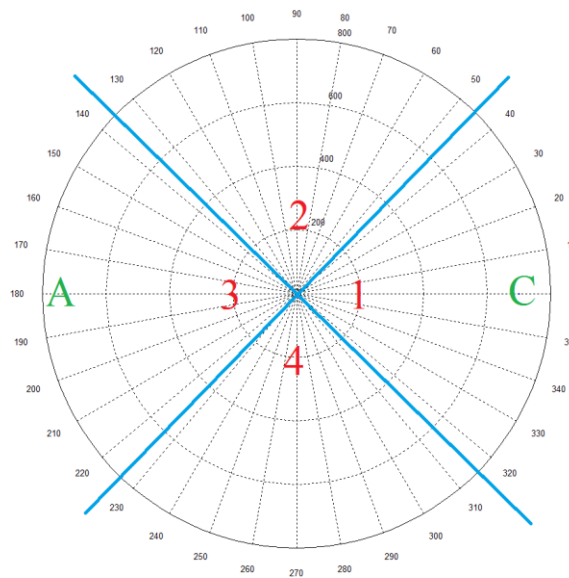


Figure 4.5: Diagram illustrating the quantification of directionality of neurites using polar plots. The plot was divided into 4  $90^\circ$  quadrants, and each quadrant was sub-divided into 3  $30^\circ$  segments. Quadrant 1 faced the cathode (C) whereas quadrant 3 faced the anode (A).

#### 4.2.7 Statistical Analysis

Statistical analysis was performed on neurite growth, cell spreading, neurite density, directionality and cell viability for each position and frequency of stimulation using MATLAB. As the data was not normally distributed, a non-parametric test, Kruskal-

Wallis test was employed to obtain significance between the data, where  $p < 0.05$  was considered significant.

### 4.3 Results

#### 4.3.1 Neurite growth

The labeled images for all frequencies of stimulation at positions A and C are shown in Figure 4.6(A-I). The graphical representation of average neurite growth for about 40 samples per condition, 24hr after stimulation with respect to the stimulation frequency and position is showed in Figure 4.7. The error bars represent the standard deviation of the neurite outgrowth value from the mean. The average growth for 20Hz and 200Hz was  $427 \pm 58.07\mu\text{m}$  and  $395 \pm 54.78\mu\text{m}$  and it decreased with an increase of the input frequency of stimulation. Also, the neurite growth was comparatively greater for DRG at position A than position C, at low frequencies. Statistical tests showed significant difference between the neurite growth at positions A and C for 20Hz and 200Hz ( $p < 0.05$ ). However, no significant difference was found between the neurite growth at positions A and C for 1MHz and 20MHz ( $p > 0.05$ ). Since DRG at position A were exposed to higher EF than position C, these results indicated that neurites grow longer in regions exposed to higher EF. However, the effect of EF was prominent only at low frequencies. The neurite length was also significantly different for stimulated samples from the control ( $149 \pm 23.97\mu\text{m}$ ) for 20Hz, 200Hz and position A at 1MHz, but not for positions C for 1MHz and A, C for 20MHz ( $p > 0.05$ ). Thus, AC stimulation of nerve tissue at frequency less than 1MHz increases neurite growth. The growth of the neurite at 1MHz and 20MHz was similar to the control samples.

Table 4.2: Average  $\pm$  standard deviation neurite growth for all frequencies and positions.  
 \* represents the values that are significantly different from sham.

<b>Freq (Hz)</b>	<b>Sham</b>	<b>position A (<math>\mu\text{m}</math>)</b>	<b>position C (<math>\mu\text{m}</math>)</b>
	149.65 $\pm$ 23.97	-	-
20	-	427.61 $\pm$ 58.07*	322.08 $\pm$ 50.25*
200	-	395.31 $\pm$ 54.78*	302.94 $\pm$ 44.64*
1000000	-	212.51 $\pm$ 47.13*	186 $\pm$ 47.39
20000000	-	172.54 $\pm$ 51.33	157.54 $\pm$ 48.65

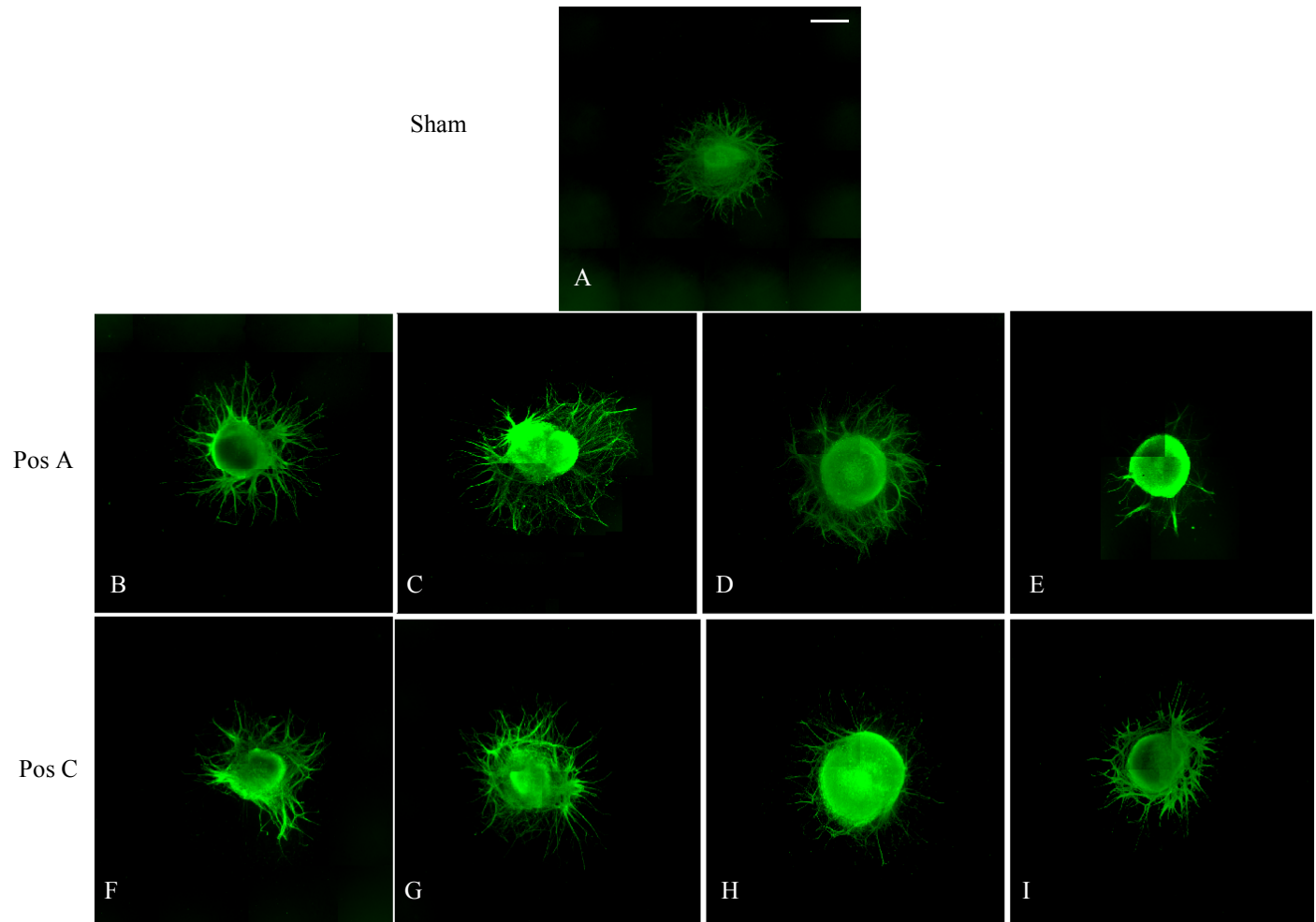


Figure 4.6: Post-stimulated images of DRG samples, A is sham, B-E are stimulated DRG for position A for 20Hz, 200Hz, 1MHz and 20MHz, respectively, while F-I are for position C. The lengths of the neurites were measured by Eqn. 4.2. From the figure, it is clear that neurites grow longer in LF stimulations, and the length of neurites for HF was similar to control. The white bar in A represents a scale of 500  $\mu\text{m}$ .

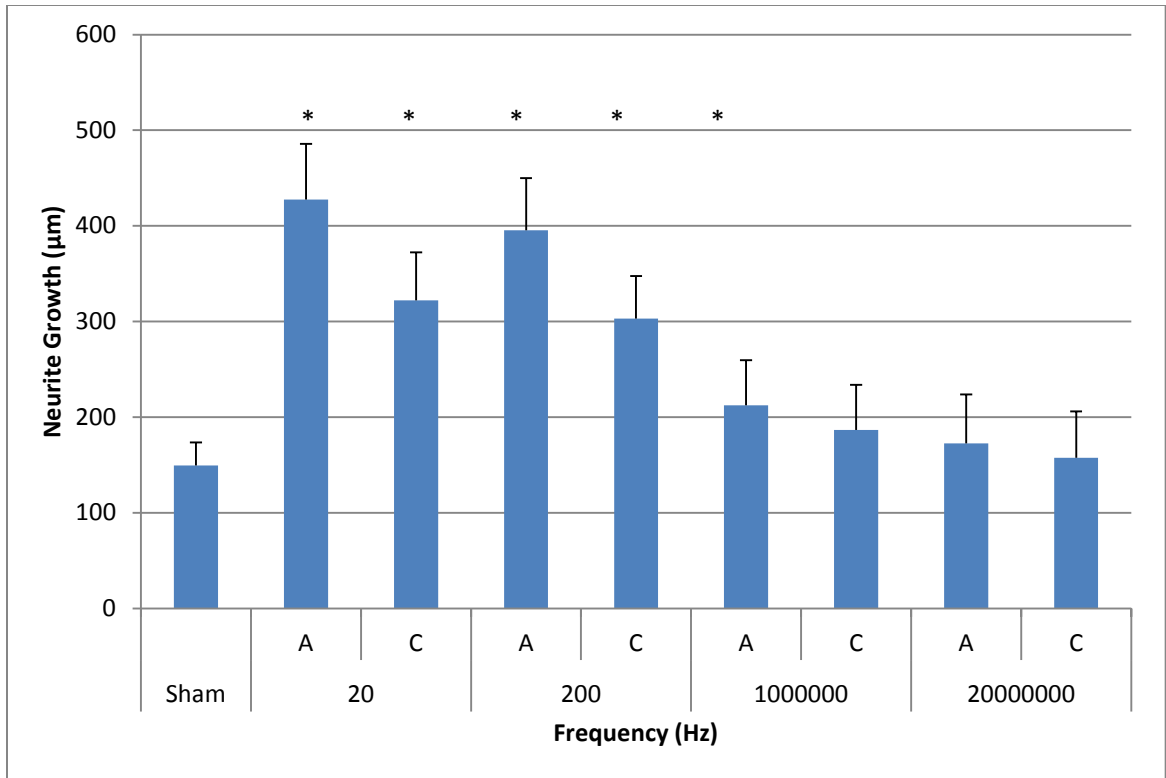


Figure 4.7: Graphical representation of average neurite growth  $\pm$  standard deviation for all the frequencies of stimulation for positions A and C. The sample size was  $n = 40$  for each case. Statistical significance between the sham and stimulated samples is indicated by \* ( $p < 0.05$ ). Results indicate that neurite length for 20Hz, 200Hz and 1MHz (position A) is significantly different from sham and HF. Thus, LF stimulation promotes growth. Also, the length at position A was significantly different from position C for LF samples, indicating that high intensity fields aids in more growth of neurites.

#### 4.3.2 Cell spreading from DRG body

Fluorescent images of cell spreading for all the frequencies of stimulation are shown in Figure 4.8(A-I). The CS ratio was calculated for 40 samples per condition, and the average CS ratio was plotted with respect to frequency and position, as shown in Figure 4.9. The CS ratio for control sample was calculated as  $1.05 \pm 0.03$ , indicating that the distance of the farthest cell was approximately the same as the neurite length. Statistical analysis showed no significant difference in the CS ratio between positions A and C for any frequency of stimulation ( $p > 0.05$ ). However, statistical significance was observed

between CS ratio of stimulated samples for all frequencies with the control samples, with average CS ratio of  $1.48 \pm 0.04$  ( $p < 0.05$ ). Thus in culture, the cells of the DRG migrated from the DRG body. The distance of the farthest cell from the center of the DRG body was larger than the longest neurite in stimulated samples. This indicated that AC stimulation caused the cells in the tissue to spread to a greater distance than no stimulation, regardless of the frequency or the magnitude of the EF. The results are tabulated in Table 4.2.

Table 4.3: Average  $\pm$  standard deviation CS ratio for all frequencies and positions.

<b>Freq (Hz)</b>	<b>Sham</b>	<b>position A (<math>\mu\text{m}</math>)</b>	<b>position C (<math>\mu\text{m}</math>)</b>
	$1.05 \pm 0.04$	-	-
20	-	$1.48 \pm 0.13$	$1.44 \pm 0.12$
200	-	$1.47 \pm 0.12$	$1.46 \pm 0.14$
1000000	-	$1.53 \pm 0.11$	$1.44 \pm 0.11$
20000000	-	$1.53 \pm 0.11$	$1.43 \pm 0.11$

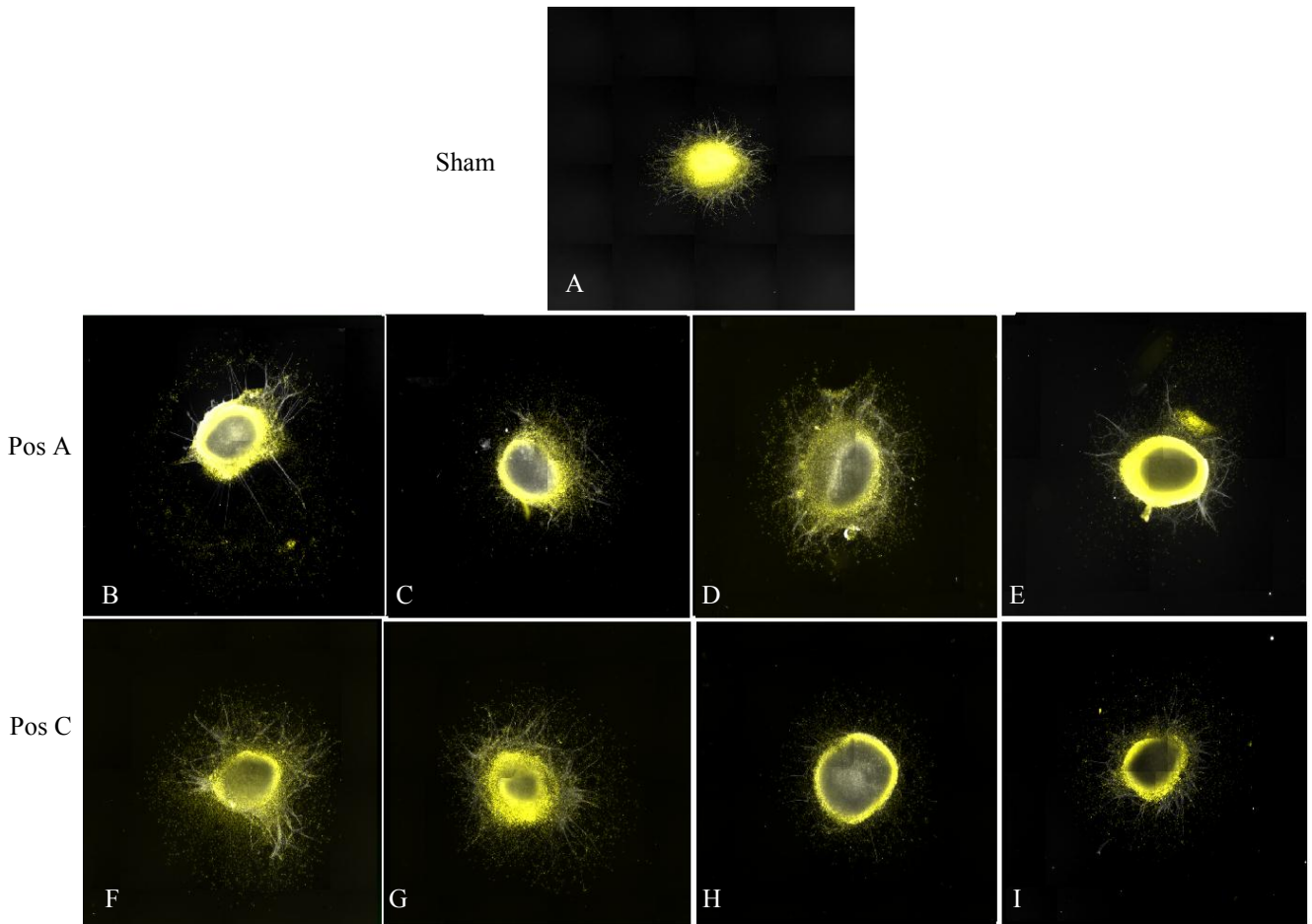


Figure 4.8: Post-stimulated images of DRG samples, yellow dots represents the cells; A is sham, B-E are stimulated DRG for position A for 20Hz, 200Hz, 1MHz and 20MHz, respectively, while F-I are for position C. The distance of furthest cell from the DRG body was quantified by Eqn. 4.5. The figure illustrates that the cells spread to greater distances in stimulated samples, regardless of frequency and intensity of EF, than the control samples. The white bar in A represents a scale of 500  $\mu\text{m}$ .

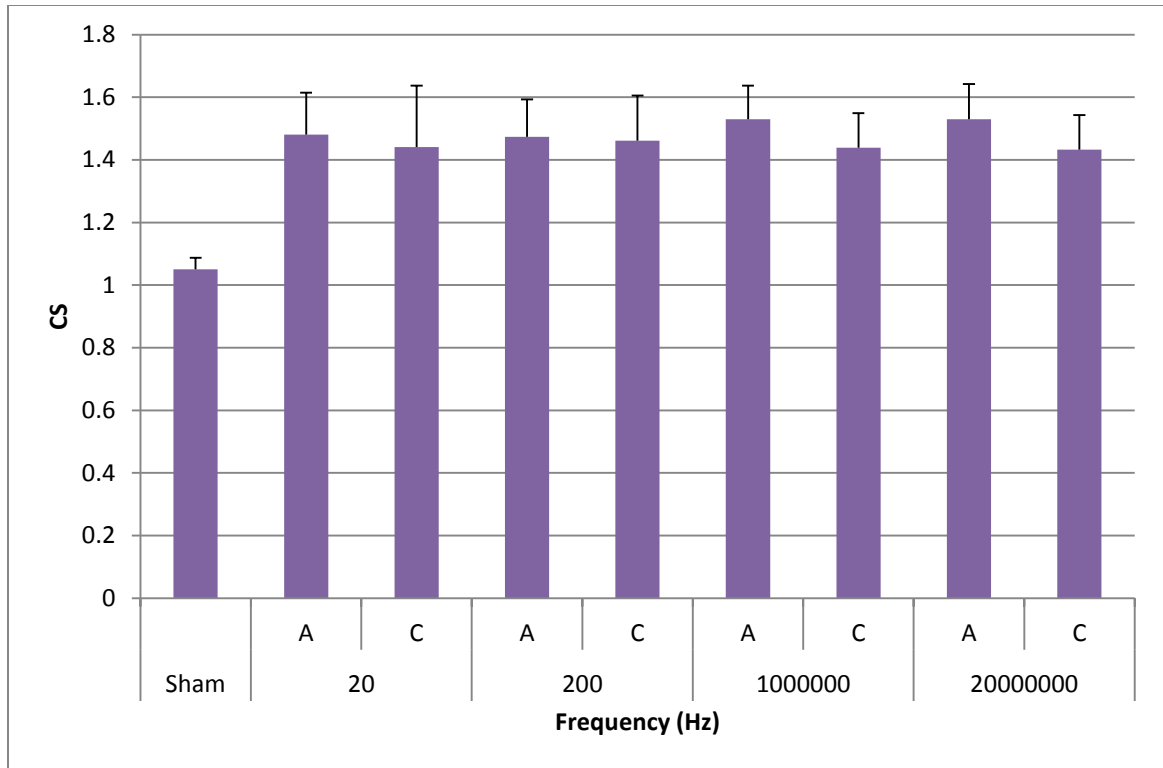


Figure 4.9: Graphical representation of average CS ratio  $\pm$  standard deviation for all the frequencies of stimulation for positions A and C. The sample size was  $n = 40$  for each case. Results indicated that CS ratio for stimulated samples was significantly different from the control samples.

#### 4.3.3 Cell viability

Figure 4.10 (A-R) shows the viability images for all the frequencies of stimulation, where green-labeling represented live cells and the red represented dead cells. MATLAB was used to quantify the cell viability. Figure 4.11 depicts the % viability of cells after stimulation at positions A and C. The plot shows that  $71.4 \pm 1.5\%$  cells were viable after 1 hr AC stimulation at 20Hz and 200Hz. The % cell viability was not significantly different for lower frequencies than at 1MHz and 20MHz, which were  $69.0 \pm 1.35\%$  and  $69.52 \pm 1.4\%$ , respectively ( $p > 0.05$ ). The results show that high frequency AC stimulation of nerve tissue does not impact the cell viability significantly as compared to low frequencies. The results are tabulated in Table 4.3.

Table 4.4: Average  $\pm$  standard deviation % viability for all frequencies and positions.

<b>Freq (Hz)</b>	<b>Sham</b>	<b>position A (%)</b>	<b>position C (%)</b>
	72.8 $\pm$ 1.4	-	-
0	-	71.6 $\pm$ 1.6	71.4 $\pm$ 1.3
200	-	71.2 $\pm$ 1.5	72.6 $\pm$ 1.4
1000000	-	68.9 $\pm$ 1.3	69.1 $\pm$ 1.4
20000000	-	68.5 $\pm$ 1.5	70.1 $\pm$ 1.3

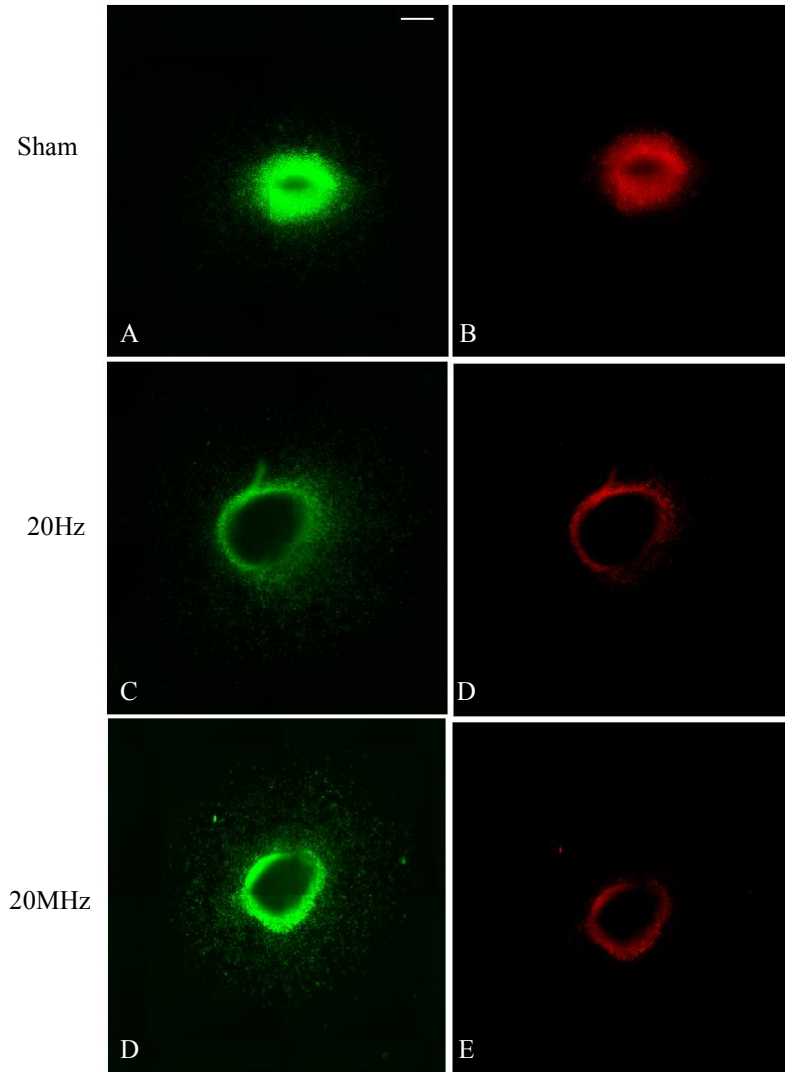


Figure 4.10: Post-stimulated images of DRG for viability study; the green stained images represent the live cells and the red stained images represent the dead cells. The images show that application of EF at high intensity or high frequency does not significantly impact cell viability than compared to control sample. The white bar in A represents a scale of 500 $\mu$ m.

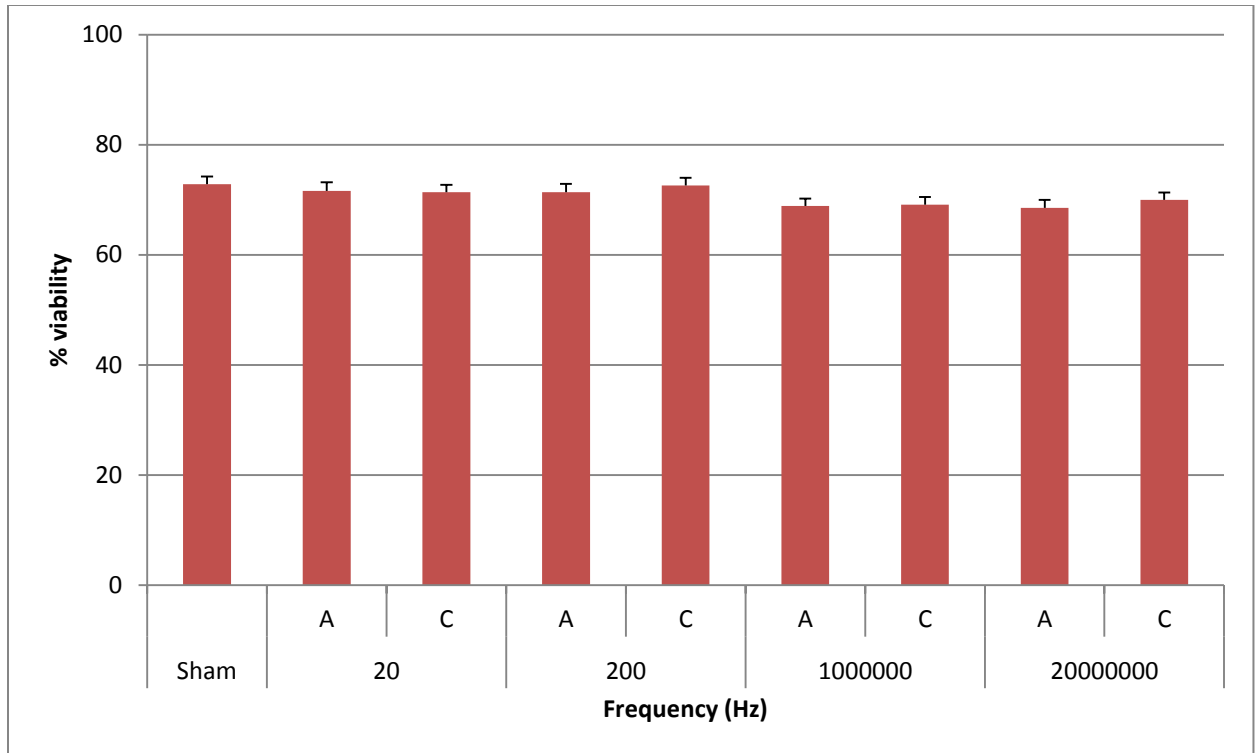


Figure 4.11: Graphical representation of average % viability  $\pm$  standard deviation for all the frequencies of stimulation for positions A and C. The sample size was  $n = 40$  for each case. Results indicate that the cell viability for stimulated samples is not significantly different from the control samples. Thus, application of ES at any intensity or frequency does not affect the cell viability.

#### 4.3.4 Neurite density

The density of the neurites with respect to the position of the electrode was quantified for each frequency using density ratio,  $D$ .  $D$  was calculated for all the 40 experiments for each frequency and sham, and the average  $D \pm$  standard deviation for each frequency was plotted, as shown in Figure 4.12. The value of  $D$  was found to be  $1 \pm 0.27$  for control, indicating that the density of neurite growth towards anode and cathode was almost same. However, for low frequencies,  $D$  was  $1.9 \pm 0.32$  for position C and  $2.4 \pm 0.37$  for position A, which were significantly different from control and HF ( $p < 0.05$ ). These results indicated that neurites grow more densely towards cathode than anode, and that the

density was greater for the DRG at position A. Also, the density of neurites at position A may be greater due to more EF intensity at A than C. As the frequency increases to MHz range, the ratio became  $1.1 \pm 0.29$  for position A and  $1.12 \pm 0.27$  for position C. The density results are similar to those obtained in length of neurite outgrowth, where an increase of frequency decreased growth and the characteristics of the tissue became similar to control ( $p > 0.05$ ). Thus, HF stimulation reduced the length as well as density of neurite growth compared to LF stimulation. The results are tabulated in Table 4.4.

Table 4.5: Average  $\pm$  standard deviation density ratio (D) for all frequencies and positions. \* represents the values that are significantly different from sham.

<b>Freq (Hz)</b>	<b>Sham</b>	<b>position A (<math>\mu\text{m}</math>)</b>	<b>position C (<math>\mu\text{m}</math>)</b>
	$1.01 \pm 0.12$	-	-
20	-	$2.41 \pm 0.32^*$	$1.96 \pm 0.32^*$
200	-	$2.45 \pm 0.36^*$	$1.89 \pm 0.25^*$
1000000	-	$1.12 \pm 0.27$	$1.11 \pm 0.24$
20000000	-	$1.08 \pm 0.32$	$1.04 \pm 0.31$

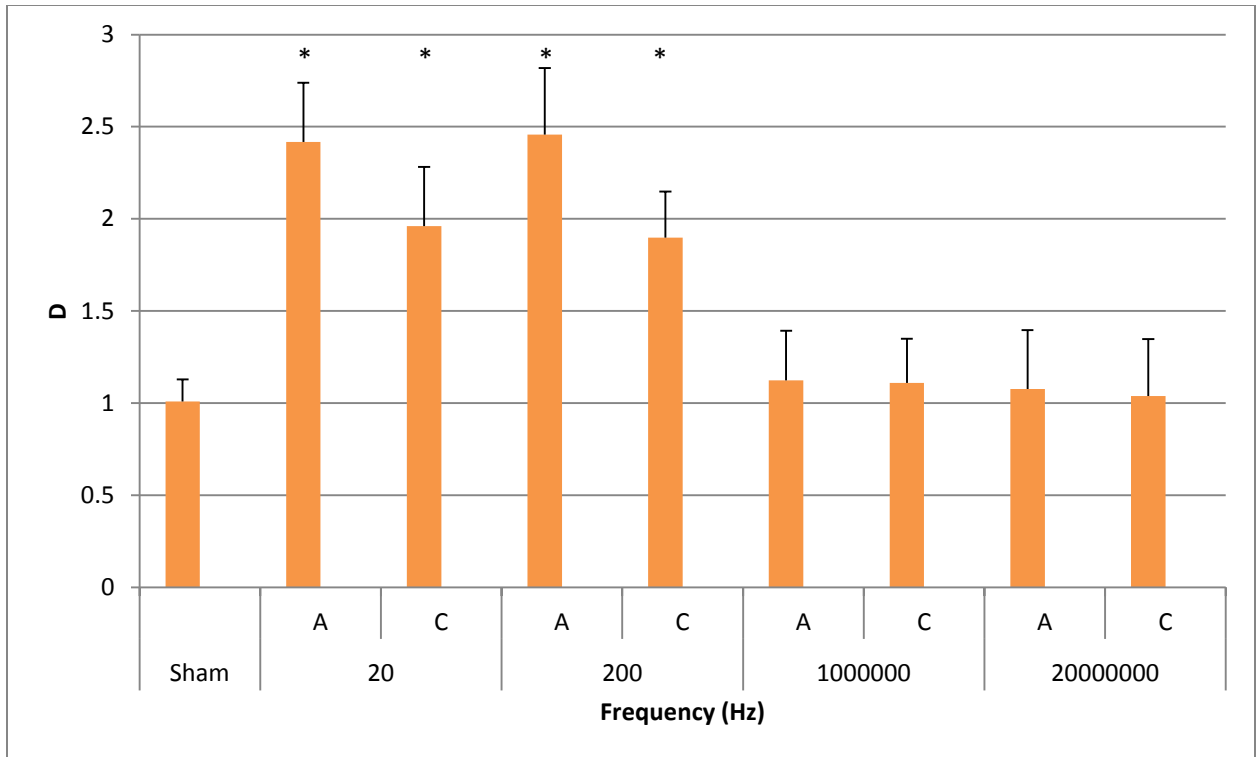


Figure 4.12: Graphical representation of average density ratio ( $D$ )  $\pm$  standard deviation for all the frequencies of stimulation for positions A and C. The sample size was  $n = 40$  for each case. Statistical significance between the sham and stimulated samples is indicated by \* ( $p < 0.05$ ). Results indicated that density for 20Hz, 200Hz and 1MHz (position A) was significantly different from sham and HF. Thus, LF stimulation led to growth of denser neurites towards cathode. Also,  $D$  at position A was significantly different from position C for LF samples, indicating that high intensity fields aided in denser growth of neurites.

#### 4.3.5 Neurite directionality

The number of points per quadrant ( $N_{tips}$ ) was counted to determine the quadrant with the highest number of neurites for all the frequencies and positions, as shown in Figure 4.13 (the plots of other frequencies and positions can be found in Appendix). The total number of neurite tips per quadrant was plotted for each frequency for positions A and C, as shown in Figure 4.14. The quantification of orientation of neurites with regard to the direction of EF was done using polar plots, where the distance of the tip of the neurite

from the DRG body and the angle of the tip were considered. The results for HF were almost equal to sham control. Thus for HF, the number of neurites in each quadrant was not significantly different from each other as well as the sham ( $p>0.05$ ). On the other hand,  $N_{tips}$  for 20Hz and 200Hz stimulation for position A in quadrant 1 were 24 and 23, respectively, which was significantly greater than the  $N_{tips}$  for all the other quadrants ( $p<0.05$ ). The  $N_{tips}$  at quadrant 1 for position C for low frequency stimulation was about  $26.5 \pm 0.5$ , which was significantly different from all other quadrants, as well as HF stimulation ( $p<0.05$ ). Thus, the number of neurites growing in quadrant 1 was significantly more than all the other quadrants and since quadrant 1 faces the cathode, it indicated that neurites have directionality towards the cathode.

Table 4.6: Total number of points in 4 quadrants. Each point represents 75 neurites with  $\pm 2.5^\circ$ . \* represents the values that are significantly different from sham.

		Total no. of points	Quad 1	Quad 2	Quad 3	Quad 4
20Hz	A	60	24*	14	11	11
	C	60	27*	12	9	12
200Hz	A	60	23*	10	13	14
	C	60	26*	13	14	7
1MHz	A	60	16	14	19	11
	C	60	18	13	17	12
20MHz	A	60	14	18	18	10
	C	60	10	16	17	17
	sham	60	13	12	16	19

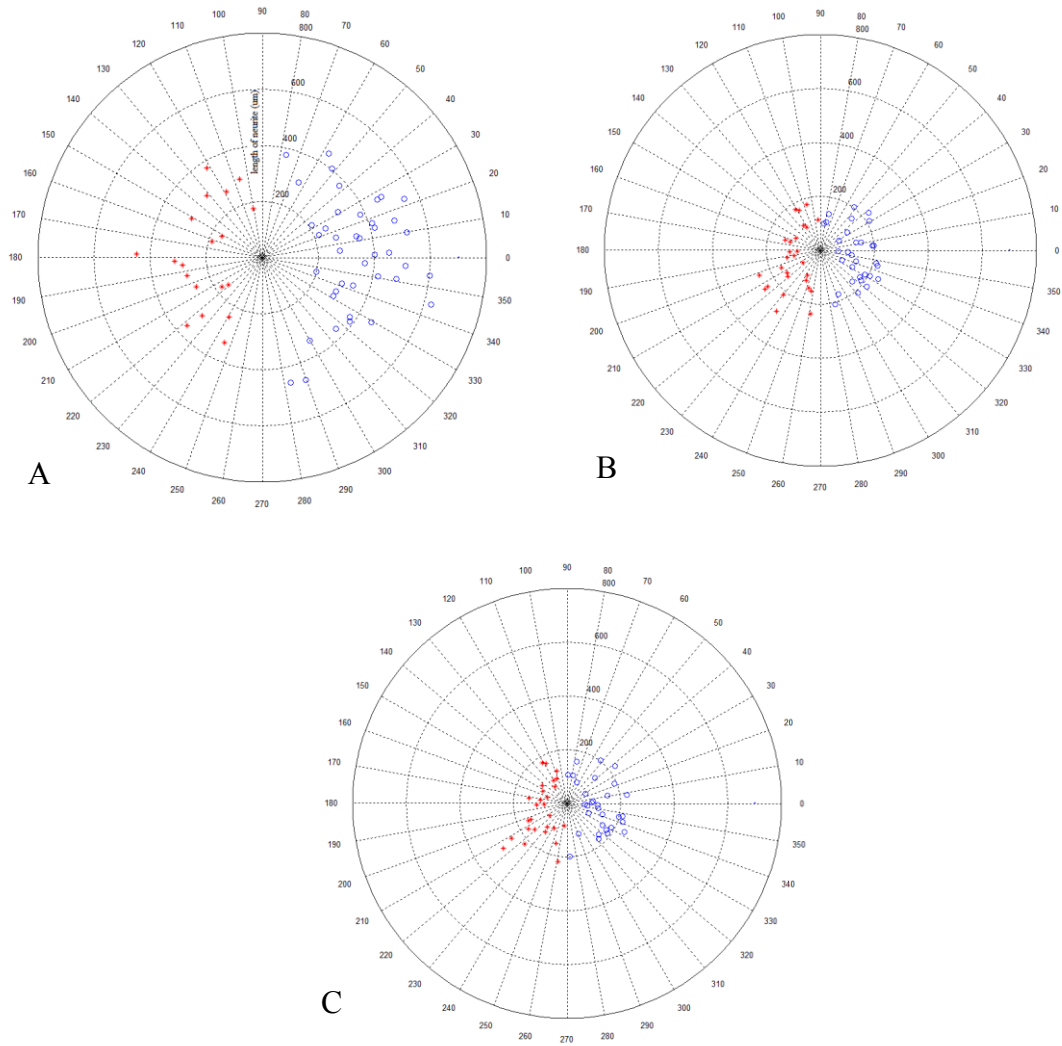


Figure 4.13: Polar plots for directionality measurements for 20Hz position A (A) and 20MHz position A (B), and control (C). The plots show that neurites grow symmetrically around the DRG body for control and 20MHz. For 20Hz, the number of neurites in quadrant 1 was significantly more than other quadrants, as well as control and 20MHz. Thus, neurites show cathodal preference at LF stimulation.

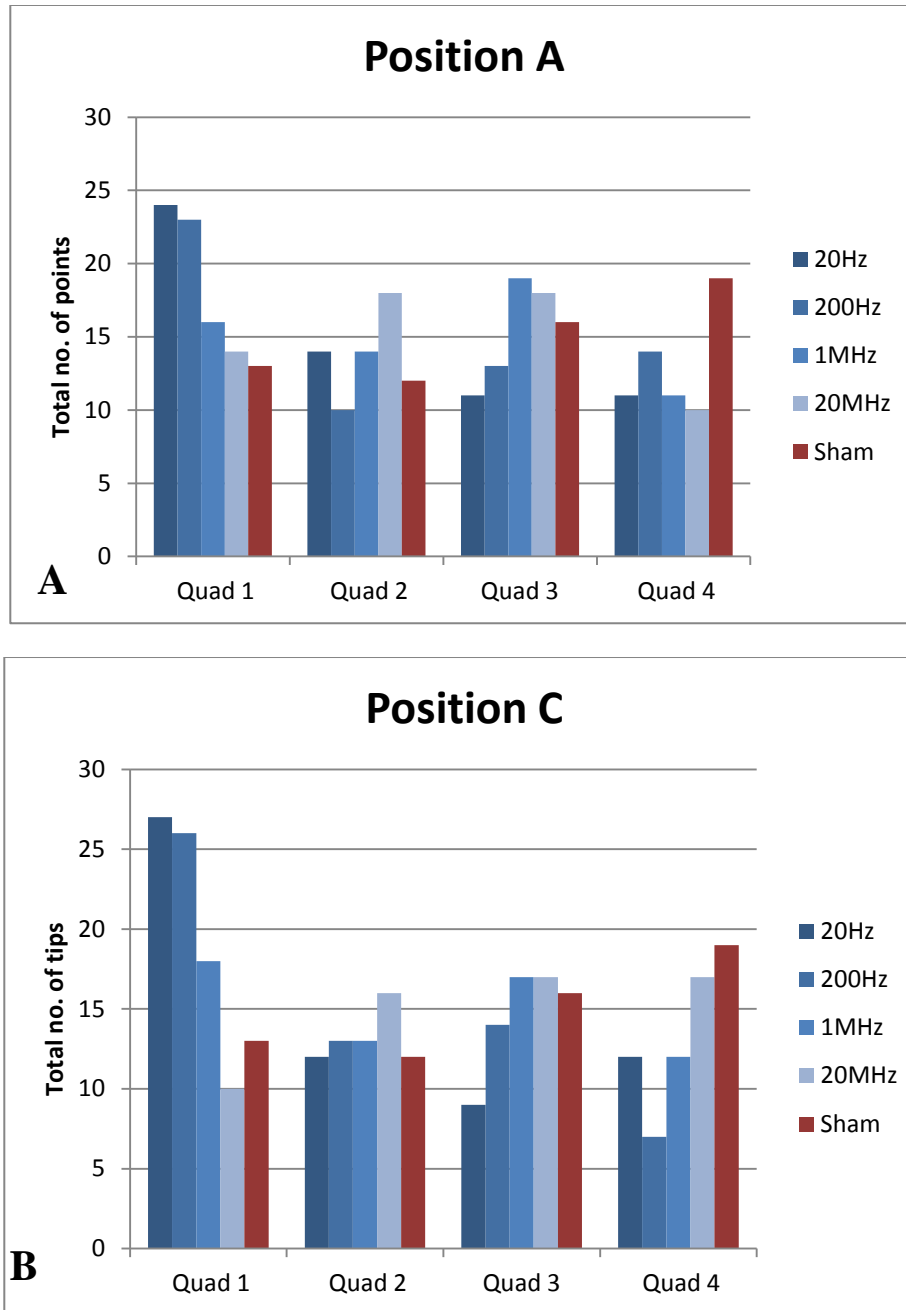


Figure 4.14: Graphical representation of the total number of tips per quadrants for 20Hz, 200Hz, 1MHz and 20MHz. A illustrates the number of tips per quadrant for position A, while B represents position C. 4500 neurites were counted for each condition. The plot representing sham is flat in both cases, indicating that neurites grow equally in all quadrants. The number of neurites is largest in quadrant 1 for 20Hz and 200Hz, indicating that more neurites grow to the side if the DRG facing cathode. The plots for 1MHz and 20MHz look similar to sham, depicting that HF does not promote directional growth of neurites.

#### 4.4 Finite element approximation

The finite element approximation (FEA) analysis of the DRG in the stimulation chamber was done using MATLAB. The partial differential equation (PDE) toolbox was used. The PDE toolbox has a GUI that can replicate any electrolysis system (electrodes and electrolyte), with conductivity of the conductivity medium as  $\sigma$ , and a steady current. The current density  $J$  is related to the electric field  $E$  through the following equation:

$$J = \sigma E \quad (4.8)$$

Combining the continuity equation:

$$\nabla \cdot J = Q \quad (4.9)$$

where  $Q$  is a current source, with the definition of the electric potential  $V$  yields the elliptic Poisson's equation:

$$-\nabla \cdot (\sigma \nabla V) = Q \quad (4.10)$$

PDE toolbox used Eqn. 4.10 to generate plots of  $V$ ,  $J$  or  $E$ . The only two PDE parameters are the conductivity  $\sigma$  and the current source  $Q$ .

The length specifications of the chamber were defined in the toolbox (7 x 3 cm) as rectangle R1, as shown in Figure 4.15. The boundary conditions of R1 was defined such that the left part of R1 (marked A in Figure 4.15) had  $V = 2.5V$  while the other parts had  $V = 0$ . Thus, A represented the anode while C represented the cathode. The two ellipses E1 and E2 represented the DRG, at positions A and C, respectively. The diameter of these ellipses was 200  $\mu\text{m}$ . The electric potential ( $V$ ) distribution along the length of the chamber was plotted, as shown in Figure 4.15. The results indicated that that DRG at

position A was exposed to higher potential than at position C, with the voltage approximately equal to 2V. The DRG at position C was exposed to 0.9V. The simulation results matched with the experimental results obtained, as listed in Table 4.1. The red arrows indicate the current density field lines in the system. From the figure, it was observed that EF flows from anode to cathode, and the current flow changes the directions and bends to flow into the DRG. Grimnes et al. explained this phenomenon by stating that ‘bending of current density field lines occurs at the interface between two homogeneous materials of different conductivity’ [53]. They elaborated that any conductive material has the property to bend oncoming current flow towards itself, while the current away from the conductive material flow parallel to the surface of the contained. In the present study, therefore, the DRG acted as conducting material, and they had the tendency to pull the current towards them. Thus, from FEA analysis, it can be stated that the increase of current density (and voltage) around the DRG body surface may be responsible for changes in neurite growth pattern after ES.

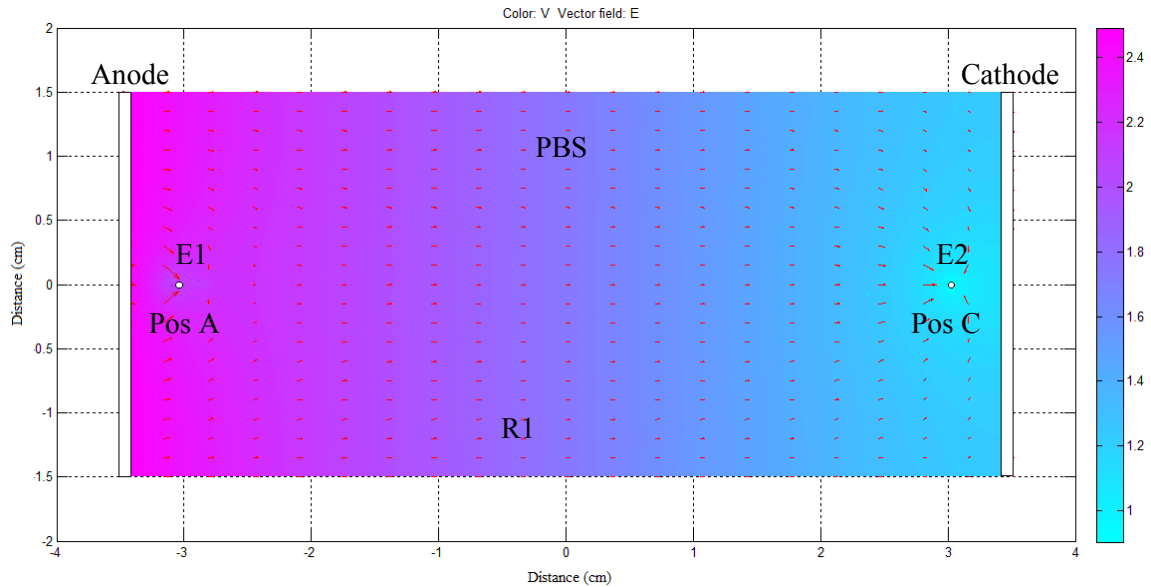


Figure 4.15: FEA plot of the voltage distribution in the ES chamber. Using boundary condition specifications, left side of R1 was stimulated at  $V=2.5$ . The DRG were placed 0.5cm away from each electrode. Results indicated that DRG at position A was exposed to 2V while DRG at position C was exposed to 0.9V, which was similar to the results obtained experimentally (Table 4.1). The red arrows represent the current density field lines.

It must be noted that the PDE equations were not frequency dependent, and the EF in the system was only the magnitude of the potential. However, the simulation was done to view the EF distribution along the chamber, irrespective of the frequency.

#### 4.5 Discussion

The effect of LF and HF stimulation on neurite growth, cell spreading from DRG body, cell viability, neurite density, and neurite directionality were quantified with respect to changes in the input frequency on chick DRG. *In vitro*, DC EF and PEMF have increased overall neurite outgrowth during and after stimulation [2-6, 29, 43-45], but less is known about the effect of frequency and EF intensity on neurite growth and directionality. The

results of the present study demonstrated that the response of chick DRG to EF stimulation at low and high frequencies is frequency dependent.

*In vitro* stimulation of chick DRG for 1hr at low frequency of 20Hz and 200Hz increased neurite growth, and aided in denser neurite growth towards the cathode. Although the density of growth with respect to frequency has not been quantified in the literature, the length of the neurite growth after stimulation frequencies < 200Hz in the present study were similar to the literature, where stimulation of chick DRG and PC12 cells increased growth by approximately 400 $\mu$ m [2, 29]. The effect of field intensities on nerve cells or tissues was another aspect studied in the literature. The intensity of EF used in these studies varies from 0.1V/m to 25V/m for both DC and AC stimulations, and the frequency ranges from 10Hz to 2.5GHz [2, 7, 29, 94]. Graves et al. stimulated *ex vivo* spinal tissue resulting in increased growth and directionality of neurites towards cathode for all samples, regardless of the frequency. The differences in results may be due to different animal models, testing conditions, and number of experiments. FEA analysis was performed using MATLAB, and the results of the simulations indicated that the DRG placed closer to the current source was exposed to higher voltage, and the intensity of exposed voltage decreased as the distance between the DRG and current source increased.

The similarities in growth pattern of neurite for DC and AC fields have not been explained; however, a thorough literature survey on the topic has showed that one of the reasons may be the conductivity changes in the tissue. Tissue conductivity is frequency dependent due to the capacitive nature of the cell membranes in the tissue. According to Grimnes et al, within DC and LF fields, current passes through the extracellular fluid of a

cell [53]. Thus, at DC and LF, current does not pass through the cell, resulting in the tissue conducting less current through it, while at HF, current enters the cytoplasm, increasing the tissue conductivity [54]. Gabriel et al. plotted the conductivities of different types of tissue, which showed that increased input frequency increased conductivity [8]. Since the conductivity of the tissue is low at LF and increases significantly as the frequency increases, the amount of current that would flow inside the tissue may impact the growth. The increase of neurite growth upon application of EF may be due to the influence of EF on factors such as increased SC NGF regulation or upregulation of  $Ca^{2+}$  mediated brain derived neurotrophic factor [6, 29, 41, 45].

The effect of HF on neurite growth has been studied by Narita et al. at 2.45 GHz [94]. The EMF field was exposed to PC12 cells *in vitro* and no difference was observed between the neurite lengths for stimulated samples and control samples for 7 days after exposure. These results are in contrast with the findings of several HF stimulation studies, where significant neurite growth was observed when compared to control samples in different animal models [7, 29]. However, these studies did not observe any difference in length between LF and HF samples. Thus, the differences in the results for these studies and the present study can be due to type of field, intensity, animal model, exposure time. All of these components of an EF stimulation plays an important role in growth of neurites. Further studies on human cell types have to be done to fully understand the impact of frequency on neurite growth and to determine if HF stimulation is safe for clinical use for regeneration of nerves.

The results from the present study also demonstrated that neurites exhibited preferential cathodal growth under the influence of LF AC fields. The findings of asymmetrical

growth of neurites for AC agree with previous studies, all of which quantified neurite directionality for *Xenopus* in DC fields [7, 42-45]. The method of quantification of neurite orientation followed by previous papers was either manually counting the number of neurites on each side or calculating the ratio of total number of neurites on each side. Although these methods showed preferential cathodal orientation statistically, they are not suited for a large group of neurites. The method followed by the present study included plotting groups of neurites on polar plots, which regarded both length and angular position of neurite tips thereby making comparison of large groups of data an easier task, and also provided a good visual of the symmetry of neurite growth around the DRG body.

Weiss explained the reason for neuronal galvanotropism to be the generation of a mechanical force by the micelles oriented in the culture medium [10]. Patel and Poo performed similar experiments using DC fields while constantly changing the culture medium and perfusion of medium perpendicular to the field, and found no changes in the growth symmetry of neurites, thus concluding that galvanotropism was not a factor of charge flow or field induced gradients of ions [42, 43]. The argument put forth by them was that neurites grew preferentially towards cathode may be because the EF may create a cytoplasmic potential drop with respect to the extracellular fluid that could lead to redistribution of cytoplasmic materials involved in neurite growth, which causes asymmetrical growth [42]. The DC field used for the experiments was 10V/cm which was sufficient to create the potential drop across the membrane. Since galvanotropism was observed at LF in the present study, it can be said that the EF generated within the cell at LF was ample to create the potential gradient. However, this does not account for

the fact that galvanotropism was not observed for HF at position A, but was observed for LF at position C, when the former is exposed to more EF even after attenuation of EF. Thus, the argument of redistribution of cytoplasmic material to influence orientation is not satisfactory. The results of the present study shows that neurite orientation is frequency dependent and thus, the changes in intracellular properties of materials controlling neurite growth and symmetry, as suggested by Patel and Poo, may not be due to influence of intensity of voltage, but due to frequency of voltage. Further research needs to be done to obtain conclusive results.

In addition to quantification and comparison of neurite response to EF, the movement of cells was also observed in the present study. Results show that the cells spread away from the DRG body to greater distances than the neurites with the application of AC stimulation, regardless of the frequency of stimulation and intensity of EF. Effective directional neural cell movement is crucial in development of the CNS and for neurogenesis. Recent evidence shows that small EFs not only guide axonal growth, but also direct the events of cell migration in neural tissues [79, 93]. It has been suggested by Marin that movement of cells aids in neurite growth by steering the growth cone and application of EF leads to spreading of cells to greater distances in less time, which may aid in growth of the neurites to longer lengths [79]. While the prime focus of these studies was SC movement, it is not clear if movement of other cell types like fibroblasts, astrocytes, etc. have a role in neurite guidance. The result of the present study showed that the many cells move away from the DRG tissue body and as stated in Chapter 3, the major cell types in DRG can be fibroblasts, neurons or SC. Thus, by using specific labeling techniques described in Chapter 3, the impact of EF on different cell types can

be observed to understand the connection between cell migration and neurite growth, and thus, research can be narrowed down to specific cell types and their effect on neurite growth and ultimately, nerve regeneration.

From the perspective of using AC stimulation in treatment of nerve injury, even though LF stimulation shows similar cellular response to DC stimulation, AC stimulation has additional benefits of low power consumption and greater penetration. Graves et al demonstrated that greater EFs are established by AC stimulation at equal current magnitudes to DC stimulation, which indicates that similar fields can be achieved with less AC stimulation than DC thereby reducing the power [7]. According to this study, the decrease in power consumption would decrease the size of the implantable device due to smaller power requirements and allow for greater treatment periods.

#### 4.6 Conclusion

In the present study, the effect of AC stimulation on chick DRG was observed, at LF and HF in a non-uniform EF. The hypothesis of this study was that biological characteristics of DRG are influenced by the changes in conductivity of the DRG and path of the current flow at HF. Results suggest that LF stimulation enhanced neurite growth and density near the anode (higher EF intensity). Also, AC stimulation caused the cells to move away from the DRG body and the neurites follow the cells, which indicated that the EF led to faster movement of cells and may act as a guidance factor for the neurites. LF stimulation of DRG also aids the neurites to grow preferentially towards the cathode, following the charge flow. The biological characteristics of the DRG at HF were similar to the control. Due to the inability of the cells to respond quickly to the increased rate of cycles at HF

and greater currents inside the tissue, the cellular response of the tissue at HF is diminished than LF. Thus, high intensity fields at LF enhance biological characteristics of nerve tissues better than low intensity fields and HF stimulation.

## CHAPTER V

### CONCLUSION

- *Goal 1:* Identify the cell types in chick dorsal root ganglion (DRG) and purification of Schwann cells from mixed population.

Three main cell types were identified in chick DRG using antibody labeling method: neurons, Schwann cells (SC) and fibroblasts. A simple method of purification of SC from the mixed population was devised based on differential adhesion. Results showed that after 2 hr culture, SC begin to separate from the mixed population, and the adherent population contains 98.3% SC. After 4 hr, all the three cell types adhere to the surface and the non-adherent population contains only 0.05% of the total cells.

- *Goal 2:* Determine the impact of ES on length of neurite.

AC stimulation at low and high frequencies in a non-uniform field impacts neurite growth. Results show that LF stimulation up to 200Hz promotes neurite growth and more growth was observed in the higher EF intensity region with average growth of  $411.46 \pm 22.84 \mu\text{m}$ , which was also shown by FEA analysis of the system. HF stimulation above 1MHz lead to reduced neurite growth of average growth of  $192.52 \pm 28.26 \mu\text{m}$ , which was not significantly different from the

control samples. Thus, LF stimulation at high EF intensity enhances neurite growth, while HF and low intensity stimulation does not.

- *Goal 3:* Quantify changes in cell movement with different ES and compare to neurite length.

The movement of cells after the application of EF was quantified by using the CS ratio value, which is the ratio of the distance of the furthest cell from the DRG body to the length of the longest neurite. The CS for control was  $1.05 \pm 0.03$ , indicating that for unstimulated samples, the cells do not spread to a greater distance. On application of stimulation, for both LF and HF, the CS ratio was  $1.48 \pm 0.04$ . Thus, ES increased the spreading of cells away from the DRG body.

- *Goal 4:* Quantify cell viability with respect to frequency of stimulation.

Percent cell viability was calculated for all frequencies of stimulation and intensities by using MATLAB. Results showed that for control samples, 72.8% cells are viable. The average % viabilities for LF and HF stimulation were  $72.0 \pm 0.6\%$  and  $69.5 \pm 0.6\%$ , respectively which were not significantly different from control samples. Thus, AC stimulation of DRG at frequencies up to 20MHz at any intensity up to  $2.5V_{p-p}$  did not significantly impact the cell viability

- *Goal 5:* Determine the impact of ES on neurite density.

The density of neurite outgrowth with respect to the electrodes was quantified by using MATLAB. A variable called density ratio (D) was defined, which was the ratio of the number of neurite pixels facing cathode to anode. Control samples depicted symmetrical density distribution of neurites, with D value equal to  $1.01 \pm 0.12$ . However, at LF stimulation, the value of D was greater and

significantly different from control samples, with denser neurites growing to the side of the DRG facing the cathode. At HF, D reduced to  $1.11.5 \pm 0.24$  and  $1.06 \pm 0.35$  which was significantly different from LF but not from sham. Thus, LF stimulation and low as well as high intensity promotes the growth of denser neurites towards cathode.

- *Goal 6:* Determine the impact of ES on directionality of neurite.

The quantification of directionality of neurite growth with respect to direction of flow of current in the chamber was done by using polar plots. The total number of neurite tips was counted for each frequency in quadrants, with quadrant 1 facing the cathode and quadrant 3 facing the anode. Around 24 and 23 points were counted out of 60 points to grow in quadrant 1 for 20Hz and 200Hz, respectively at position A, while 27 and 26 points were counted at position C, each point representing a total of 75 neurites within  $\pm 2.5^\circ$  angle and  $\pm 10 \mu\text{m}$  length. These values were significantly different from control samples and HF samples as well as all the other three quadrants. The results indicate that more neurite grow towards the cathode than anode at LF stimulation and at low intensity of EF, the number of neurites facing cathode is more. Thus, neurites exhibit directionality towards the cathode at LF and greater orientation was observed at low EF intensity. With the increase of frequency, the neurites grow symmetrically around the DRG body, similar to sham.

## CHAPTER VI

### FUTURE WORK

The results of the present study demonstrated that frequency of the external AC field has an impact on neurite growth, density, and directionality. Also, the distance of cell migration from the DRG body compared to the neurite length increased on ES application regardless of the frequency. The conductivity of DRG tissue needs to be further established by electrical modeling. However, the usage of microelectrodes for measurement of conductivity of DRG would give more reliable results. Also, literature review showed that increased activity of voltage gated ion channels at low frequencies leads to increased influx of ions, which may influence neurite growth. Usage of voltage clamping techniques to measure ionic current at different frequencies may supply information to address whether these channels are influenced by ES. Also, measurement of ionic concentration inside the cytoplasm of the neurites before and after stimulation can give more concrete inferences on the role of ionic concentration on neurite growth.

## BIBLIOGRAPHY

1. National Center for Health Statistics. PNS Injury Facts and Figures at a Glance. Birmingham, AL: National Center for Health Statistics, 2011.
2. Wood, M., Willits, R. K. (2006). Short-Duration, DC Electrical Stimulation Increases Chick Embryo DRG Neurite Outgrowth. *Bioelectromagnetics*, 27(4): 328-331.
3. Greenebaum, B., Sutton, C. H., Vadula, M. S., Battocletti, J. H., Swiontek, T., DeKeyser, J., Siskin, B. F. (1996a). Effects of pulsed magnetic fields on neurite outgrowth from chick embryo dorsal root ganglia. *Bioelectromagnetics*, 17(4):293–302.
4. Macias, M. Y., Battocletti, J. H., Sutton, C. H., Pintar, F. A., Maiman, D. J. (2000). Directed and enhanced neurite growth with pulsed magnetic field stimulation. *Bioelectromagnetics*, 21(4):272–286.
5. Zhang, Y., Ding, J., Duan, W., Fan, W. (2005) Influence of Pulsed Electromagnetic Field with different Pulse Duty Cycles on neurite outgrowth in PC12 rat pheochromocytoma cells. *Bioelectromagnetics*, 26(5): 406-411.
6. Koppes, A. N., Seggio, A. M., Thompson, D. M. (2011) Neurite outgrowth is significantly increased by the simultaneous presentation of Schwann cells and moderate exogenous electric fields. *J Neural Eng.* 8(4):046023.
7. Graves, M. S., Hassell, T., Beier, B. L., Alboris, G. O, Irazoqui, P. P (2011) Electrically Mediated Neuronal Guidance with Applied Alternating Current Electric Fields. *Ann Biomed Eng.* 39(6): 1759 – 1761.
8. Gabriel, S., Lau, R. W., Gabriel, C. (1996) The dielectric properties of biological tissues: II. Measurements in the frequency range 10 Hz to 20 GHz. *Phys. Med. Biol.* 41:2251–2269.

9. Whitaker, J. C. (1996) *The Electronics Handbook*. CRC Press, CA.
10. Weissmanshomer, P., Fry, M. (1975). Chick embryo fibroblasts senescence in vitro: Pattern of cell division and life span as a function of cell density. *Mechanisms of Ageing and Development* 4 (2): 159–166.
11. Hartline, D. K., Colman, D. R. (2007). Rapid conduction and the evolution of giant axons and myelinated fibers. *Curr. Biol.* 17 (1): 29–35.
12. Grothe, C., Nikkhah G. (2001). The role of basic fibroblast growth factor in peripheral nerve regeneration. *Anat Embryol (Berl)*. 204(3):171-7.
13. Danielsen, N., Pettmann, B., Vahlsing, H. L., Manthorpe, M., Varon S. (1988) Fibroblast growth factor effects on peripheral nerve regeneration in a silicone chamber model. *J Neurosci Res.* 20(3):320-30.
14. Dreesmann, L., Mittnacht, U., Lietz, M., Schlosshauer, B. (2009) Nerve fibroblast impact on Schwann cell behavior. *Eur J Cell Biol.* 88(5):285-300.
15. Bhatheja, K., Field, J. (2006). Schwann cells: Origins and role in axonal maintenance and regeneration. *Int. J. Biochem. Cell Biol.* 38 (12): 1995–9
16. Moradzadeh, A., Borschel, G. H., Luciano, J. P., Whitlock, E. L., Hayashi, A., Hunter, D. A., Mackinnon, S. E. The impact of motor and sensory nerve architecture on nerve regeneration. *Exp Neurol.* 212(2):370-6.
17. Brushart, T. M., Seiler, W. D. (1987) Selective reinnervation of distal motor stumps by peripheral motor axons. *Exp Neurol.* 97:289–300.
18. Brenner, M. J, Lowe J. B., Fox, I. K., Mackinnon, S. E., Hunter, D. A., Darcy, M. D., Duncan, J.R., Wood, P., Mohanakumar, T. (2005) Effects of Schwann cells and donor antigen on long-nerve allograft regeneration. *Microsurgery.* 25:61–70.

19. J. John Alan Kiernan, J. J. A. Barr's *The Human Nervous System: An Anatomical Viewpoint*, Wolters Kluwer Health/Lippincott Williams & Wilkins, Philadelphia, 2009
20. Simon, S. *The Brain: Our Nervous System*, Mulberry Books, New York, 2006
21. Zalc, B. (2006) The acquisition of myelin: a success story. *Novartis Found. Symp.* 276: 15–21.
22. Poliak, S., Peles, E. (2006). The local differentiation of myelinated axons at nodes of Ranvier. *Nat. Rev. Neurosci.* 12 (4): 968–80.
23. Huang, C. W., Tzeng, J. N., Chen, Y. J., Tsai, W. F., Chen, C. C., Sun, W. H. (2007). Nociceptors of dorsal root ganglion express proton-sensing G-protein-coupled receptors. *Mol Cell Neurosci.* 36(2):195-210.
24. Gasser, H. S. (1955) Properties of dorsal root unmyelinated fibers on the two sides of the ganglion. *J. Gen. Physiol.* 38(5): 709-728.
25. Kandel, E. R., Schwartz, J. H., Jessell, T. M. (2000) *Principles of Neural Science*, 4th ed., McGraw-Hill, New York (2000).
26. Nieminen, K., Suarez-Isla, B. A., Rapoport, S. I (1988). Electrical properties of cultured dorsal root ganglion neurons from normal and trisomy 21 human fetal tissue. *Brain Res.*, 474: 246- 254.
27. Harper, A. A., Lawson, S. N. (1984). Electrical Properties of Rat Dorsal Root Ganglion Neurones with Different Peripheral Nerve Conduction Velocities. *J. Physiol.* 359: 47-63.
28. Brushart, T. M., Jari, R., Verge, V., Rohde, C., Gordon, T. (2005) Electrical stimulation restores the specificity of sensory axon regeneration. *Exp Neurol.* 194(1):221-9.

29. Wan, L., Xia, R., Ding, W. (2010) Low-frequency electrical stimulation improves neurite outgrowth of dorsal root ganglion neurons in vitro via upregulating Ca<sup>2+</sup>-mediated brain-derived neurotrophic factor expression. *Neural Regener. Res.* 5(16):1256-1260.
  
30. Cohan, C. S., Kater, S. B. (1986) Suppression of neurite elongation and growth cone motility by electrical activity. *Science* 232:1638-1640.
  
31. Kater, S., Letoumeau, P. (1985) Biology of nerve growth cone. *J Neurosci Res* 13: 1-347.
  
32. Kater, S. B., Mattson, M. P., Cohan, C., Connor, J. (1988) Calcium regulation of the neuronal growth cone. *Trends Neurosci* 11: 315-321.
  
33. Roth, B. J. (1994) Mechanisms for electrical stimulation of excitable tissue. *Crit Rev Biomed Eng.* 22(3-4):253-305.
  
34. Merrill, D. R., Bikson, M., Jefferys, J. G. (2005) Electrical stimulation of excitable tissue: design of efficacious and safe protocols. *J Neurosci Methods.* 141(2):171-98.
  
35. Hodgkin, A. L., Huxley, A. F. (1952) The components of membrane conductance in the giant axon of *Loligo*. *J Physiol.* 116(4): 473–496.
  
36. Gorman, P. H, Mortimer, J. T. (1983) The effect of stimulus parameters on the recruitment characteristics of direct nerve stimulation. *IEEE Trans Biomed Eng.* 30(7):407-14.
  
37. Grahame, D. C. (1947) The electrical double layer and the theory of electrocapillarity. *Chem Rev.* 41(3):441-501.
  
38. Gildemeister, M. (1944) Untersuchungen u“ber die Wirkung der Mittelfrequenzstro“me auf den Menschen. *Pfluegers Arch* 247: 366–404.
  
39. Bromm, B., Lullies, H. (1966) U“ber den Mechanismus der Reizwirkung mittelfrequenter Wechselstro“me auf die Nervenmembran. *Pfluegers Arch* 289: 215–226.

40. McFarlane, E. H., Dawe, G. S., Marks, M., Campbell, I. C. (2000). Changes in neurite outgrowth but not in cell division induced by low EMF exposure: Influence of field strength and culture conditions on responses in rat PC12 pheochromocytoma cells. *Bioelectrochemistry*, 52(1): 23-28.
41. Haastert-Talini, K., Schmitte, R., Korte, N., Klode, D., Ratzka, A., Grothe, C. (2011) Electrical stimulation accelerates axonal and functional peripheral nerve regeneration across long gaps. *J Neurotrauma*, 28(4): 661-674.
42. Patel, N., Poo, M. M. (1982). Orientation of neurite growth by extracellular electric fields. *J Neurosci* 2(4):483–496.
43. Jaffe, L. F., Poo, M. M. (1979). Neurites grow faster towards the cathode than the anode in a steady field. *J Experiment Zool* 209(1): 115–128.
44. McCaig, C. D., Sangster, L., Stewart, R. (2000). Neurotrophins enhance electric field-directed growth cone guidance and directed nerve branching. *Dev Dyn* 217(3):299–308.
45. Rajnicek, A. M., Robinson, K. R., McCaig, C. D. (1998). The direction of neurite growth in a weak DC electric field depends on the substratum: contributions of adhesivity and net surface charge. *Dev Biol.*, 203(2):412-423.
46. Fields, R. D., Neale, E. A., Nelson, P. G. (1990) Effects of patterned electrical activity on neurite outgrowth from mouse sensory neurons. *J Neurosci*. 10(9):2950-64.
47. Wo, Y., Xia, R., Li, F., Ding, W. (2009). The effect of high frequency stimulation on intracellular  $Ca^{2+}$  in sympathetic PC12 cells. *Life Science Journal*, 6(2): 65 – 70.
48. Lu, P., Jones, L. L., Snyder, E. Y., Tuszynski, M. H. (2003) Neural stem cells constitutively secrete neurotrophic factors and promote extensive host axonal growth after spinal cord injury. *Exp Neurol*. 181(2):115-29.

49. Hotary, K. B., and K. R. Robinson. (1990) Endogenous electrical currents and the resultant voltage gradients in the chick embryo. *Dev. Biol.* 140:149–160.
50. Hotary, K. B., and K. R. Robinson. (1991) The neural tube of the *Xenopus* embryo maintains a potential difference across itself. *Dev. Brain Res.* 59:65–73.
51. Hotary, K. B., and K. R. Robinson. (1992) Evidence for a role of endogenous electrical fields in chick embryo development. *Development* 114:985–996.
52. Metcalf, M. E., and R. B. Borgens. (1994) Weak applied voltages interfere with amphibian morphogenesis and pattern. *J. Exp. Zool.* 268:322–338.
53. Grimnes, S., Martinsen, O. G. *Bioimpedance and Bioelectricity Basics: Second edition.* Elsevier, London, 2008.
54. Pauly, H., Schwan, H. P. (1959) Über die Impedanz einer Suspension von Kugelformigen Teilchen mit einer Schale. *Z Naturfor*, 14b, 125 – 131.
55. Panteny, S., Stevens, R., Bowen, C. R. (2005) The Frequency Dependent Permittivity and AC Conductivity of Random Electrical Networks. *Ferroelectrics*, 319:199–208.
56. Komiyama, T., Nakao, Y., Toyama, Y., Asou, H., Vacanti, C. A., Vacanti, M. P. (2003) A novel technique to isolate adult Schwann cells for an artificial nerve conduit. *J Neurosci Methods*, 2:195–200.
57. Bhatheja, K., Field, J. (2006) Schwann cells: origins and role in axonal maintenance and regeneration. *Int J Biochem Cell Biol.* 12:1995–9.
58. Fu, S. Y., Gordon, T. (1997) The cellular and molecular basis of peripheral nerve regeneration. *Mol Neurobiol.* 1–2:67–116.

59. Bunge, M. B., Wood, P. M., Tynan, L. B., Bates, M. L., Sanes, J. R. (1989) Perineurium originates from fibroblasts: demonstration in vitro with a retroviral marker. *Science*. 243:229-31.
60. Wood, P. M. (1976) Separation of functional Schwann cells and neurons from normal peripheral nerve tissue. *Brain Res*. 3:361–75.
61. Needham, L. K., Tennekoon, G. I., McKhann, G. M. (1987) Selective growth of rat Schwann cells in neuron- and serum-free primary culture. *J Neurosci*. 7:1-9.
62. Honkanen, H. (2011) Isolation, purification and expansion of myelination-competent, neonatal mouse Schwann cells, *Eur. J Neurosci*. 26:953–964.
63. Jin, Y. (2008) Efficient Schwann cell purification by differential cell detachment using multiplex collagenase treatment, *J Neurosci. Meth*. 170(1):140–148.
64. Kreider, B. Q., Messing, A., Doan, H., Kim, S. U., Lisak, R. P., Pleasure, D. E. (1981) Enrichment of Schwann cell cultures from neonatal rat sciatic nerve by differential adhesion. *Brain Res*. 2:433–44.
65. Vroemen, M. (2002) Purification of Schwann cells by selection of p75 low affinity nerve growth factor receptor expressing cells from adult peripheral nerve, *J Neurosci. Meth.*124(2):135–143
66. Kim, H.A., Rosenbaum, T., Marchionni, M.A., Ratner, N., De Clue, J.E. (1995) Schwann cells from neurofibromin-deficient mice exhibit activation of p21ras, inhibition of cell proliferation and morphological changes. *Oncogene*, 11, 325–335.
67. Dong, Z., Sinanan, A., Parkinson, D., Parmantier, E., Mirsky, R.,Jessen, K.R. (1999) Schwann cell development in embryonic mouse nerves. *J. Neurosci. Res.*, 56, 334–348.
68. Verdu, E., Rodriguez, F.J., Gudino-Cabrera, G., Nieto-Sampedro, M., Navarro, X. (2000) Expansion of adult Schwann cells from mouse predegenerated peripheral nerves. *J. Neurosci. Meth*. 99, 111–117.

69. Lepore, G., Zedda, M., Gadau, S., Farina, V. (2003) Purified Schwann cell primary cultures from mouse and rat sciatic nerve. *Arch. Ital. Biol.*, 141, 207–210.
70. Pannunzio, M.E., Jou, I.M., Long, A., Wind, T.C., Beck, G., Balian, G. (2005) A new method of selecting Schwann cells from adult mouse sciatic nerve. *J. Neurosci. Meth.*, 149, 74–81.
71. Casella, G.T., Bunge, R.P., Wood, P.M. (1996) Improved method for harvesting human Schwann cells from mature peripheral nerve and expansion in vitro. *Glia*, 17, 327–338.
72. Ratner, N., Hong, D.M., Lieberman, M.A., Bunge, R.P., Glaser, L. (1988) The neuronal cell-surface molecule mitogenic for Schwann cells is a heparin-binding protein. *Proc. Natl Acad. Sci. U.S.A.*, 85, 6992–6996.
73. Oda, Y., Okada, Y., Katsuda, S., Ikeda, K., Nakanishi, I. (1989) A simple method for the Schwann cell preparation from newborn rat sciatic nerves. *J Neurosci Meth.* 3:163–9.
74. Foty, R. A. (2005) The differential adhesion hypothesis: a direct evaluation, *Dev Biol.* 278:255–263.
75. Steinberg, M. S. (2007) Differential adhesion in morphogenesis: a modern view. *Curr. Opin. Genet. Dev.* 17(4): 281–286.
76. Marín, O., Valiente, M., Ge, X., Tsai, L (2010) Guiding Neuronal Cell Migrations. *Cold Spring Harb Perspect Biol.* 2(2): a001834.
77. Marín, O., Rubenstein, J. L. (2003). Cell migration in the forebrain. *Annu Rev Neurosci* 26:441–483.
78. Hatten, M. E. (1999). Central nervous system neuronal migration. *Annu Rev Neurosci* 22:511–539.

79. Suga, S., Mitani, S., Shimamoto, Y., Kawase, T., Toya, S., Sakamoto, K., Kanai, H., Fukui, M., Takeneka, N. (1990) In vivo measurement of intra- and extracellular space of brain tissue by electrical impedance method. *Acta Neurochir Suppl (Wien)* ;51:22-4.
80. Horsch, K. W., Dhillon, G. S. *Neuroprosthetics: theory and practice: Volume 2.* World Scientific Publishing Co. Singapore, 2004.
81. Scott, S.A. *Sensory Neurons: Diversity, Development, and Plasticity.* Oxford University Press, USA, 1992.
82. Norman. R. S. Cable (1972) Theory for Finite Length Dendritic Cylinders with Initial and Boundary Conditions. *Biophys J.*; 12(1): 25–45.
83. Purves, D., Augustine GJ, Fitzpatrick D. *Neuroscience.* 2nd edition, Sunderland (MA): Sinauer Associates; 2001.
84. Norman, R.S. (1972) Cable Theory for Finite Length Dendritic Cylinders with Initial and Boundary Conditions. *Biophys J.* ; 12(1): 25–45.
85. Meunier, C., Lamotte d'Incamps, B. (2008) Extending cable theory to heterogeneous dendrites. *Neural Comput.*;20(7):1732-75.
86. Wilson, C.J. (1984) Passive cable properties of dendritic spines and spiny neurons. *J Neurosci.*; 4(1):281-97.
87. Bressloff, P. (2009) Cable theory of protein receptor trafficking in a dendritic tree. *Physical Review E* 79:4.
88. Prinz, A. A., Fromherz, P. (2003) Effect of neuritic cables on conductance estimates for remote electrical synapses. *J Neurophysiol.*;89(4):2215-24.
89. Kater, S. B, Mills, L. R. (1991) Regulation of growth cone behavior by calcium. *J Neurosci.*;11(4):891-9.

90. Henley, J., Poo, M. (2004) Guiding Neuronal Growth Cones by Ca<sup>2+</sup> Signals. *Trends Cell Biol.*; 14(6): 320–330.
91. Dickson, B. J. (2002) Molecular mechanisms of axon guidance. *Science.*;298(5600):1959–1964.
92. Dent, E. W., Gertler, F. B. (2003) Cytoskeletal dynamics and transport in growth cone motility and axon guidance. *Neuron.*;40(2):209–227.
93. Yao, L., Pandit, A., Yao, S., McCaig, C. D. (2011). Electric field-guided neuron migration: a novel approach in neurogenesis. *Tissue Eng Part B*, 17(3):143-53.
94. Narita, E., Sakurai, T., Suzuki, Y, Taki, M., Miyakoshi, J. (2011) Effects of Exposure to A High-Frequency Electromagnetic Field at 2.45GHz on Neurite Outgrowth in PC12VG Cells. *Microwave Workshop Series on Innovative Wireless Power Transmission: Technologies, Systems, and Applications (IMWS), 2011 IEEE MTT-S International* , pp.215,218, 12-13.
95. Tai, C., de Groat, W. C., Roppolo, J. R. (2005) Simulation of Nerve Block by High-Frequency Sinusoidal Electrical Current Based on the Hodgkin–Huxley Model. *IEEE Trans Neural Syst Rehabil Eng.*;13(3):415-22.

## APPENDICES

## APPENDIX A

### DRG MODEL AND CONDUCTIVITY

#### 1. Introduction

Biological matters such as cells and tissue have several electrical properties, such as resistance, conductance, permittivity etc. The components of the cytoplasm and membrane give rise to the dielectric behavior of the tissue. Thus, application of external field to tissue changes these properties, which govern the flow of current and voltage in it. Various theories like relaxation and dispersion have been devised to understand the response of tissue in EF, which are explained in detail in Chapter 2. The increase of conductivity plays a very important role in the changes in biological properties of any tissue because it results in intake of greater EF inside the tissue.

Panteny et al. performed experiments on random RC networks to observe the effective conductivity of the circuit when an AC sinusoidal signal is applied [55]. The findings of this study indicated that at lower frequency ( $<1\text{kHz}$ ), the conductivity of the resistors is more dominating in the circuit, and as the frequency increases, the conductivity of the capacitor increases and the entire circuit is open. Thus, at higher frequencies, the charges flowed more quickly between the parallel plates of the capacitor as it had minimum

reactance. Research by Roth confirmed these results, which were used to derive of effective conductivity of cell suspension in saline solution for different frequencies based on the volume fraction and saline conductivity [33]. Gabriel et al. plotted the conductivity of various tissues as a function of frequency [8]. Figure A.1 shows that conductivity of grey matter increases with respect to frequency.

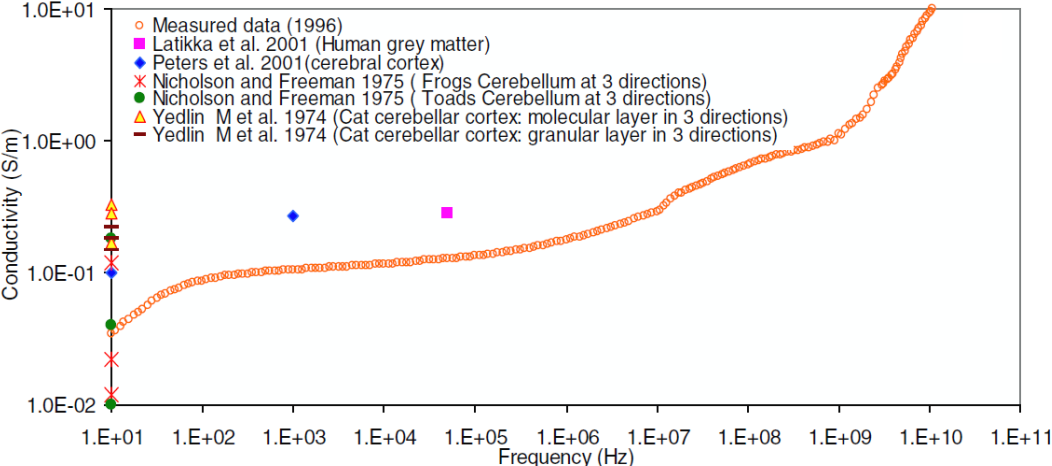


Figure A.1: Tissue conductivity of grey matter with respect to frequency of stimulation

2. Method

The DRG was modeled in the ES chamber with PBS solution using two parallel models – Maxwell-Wagner and Cole-Cole model. Using Roth equations, where the equivalent conductivity of a cell suspension of length L was derived, the DRG was modeled, as shown in Figure A.2. Here, the cells in the DRG are modeled by dividing the tissue in two parts – intracellular and extracellular. The resistive branch of the circuit is assumed as the extracellular fluid (ECF), with resistance  $R = 46 \text{ m}\Omega$  [26]. In case of Maxwell-Wagner model, the capacitive branch has  $C = 0.41 \times 10^{-3} \mu\text{F}$ . In Cole-Cole model,  $R1 = 46 \text{ m}\Omega$ ,  $R2 = 0.2 \Omega$  and  $C = 0.41 \times 10^{-3} \mu\text{F}$  [26, 27]. The assumption was made that the

average diameter of the DRG tissue was  $300\mu\text{m}$ . Thus, according to our model, if the current flows through the resistive branch, then all the current passes through the ECF and no current enters the cells. If the current passes through capacitive branch, then all the current enters through the cell membrane into the cytoplasm.

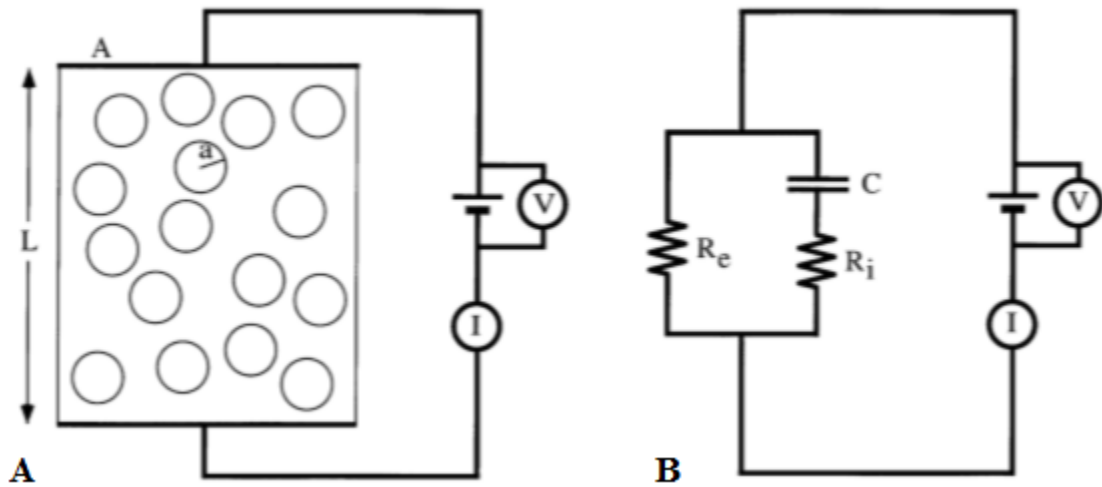


Figure A.2: (A) A schematic diagram of a suspension of cells; (B) An electric circuit equivalent of the effective conductivity of the suspended cells (*with permission* [33]).

## 2.1 Maxwell-Wagner model

The simplest form of Maxwell-Wagner model consists of two elements: a resistor and a capacitor. These elements can be combined in two different forms: in parallel or in series. However, for mimicking the electrical behavior of the tissue in the presence of DC or AC field, only parallel models are considered, because in the series model, the capacitive element blocks the passage of DC. The effective frequency-dependent conductivity of the system can be calculated using corresponding equations for each model. Let us consider the resistive element as  $R$ , capacitive element as  $C$ , as shown in Figure A.3.

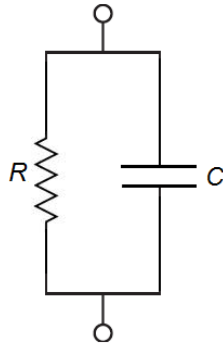


Figure A.3: Diagram of Maxwell-Wagner model in parallel combination

In the parallel combination, the admittance,  $Y$  of the circuit is given by:

$$Y = \frac{i}{v} \quad (1)$$

$$Y = G + j\omega C \quad (2)$$

Where  $i$  is the current flow in the system,  $v$  is the applied voltage and  $G$  is the conductivity of the system, in S/m.  $Y$  is a measure of the ease with which current flows in a circuit. It is the inverse of impedance ( $Z$ ) and is measured in S. The conductivity of the parallel circuit is given by:-

$$G = Y \left( \frac{1 - j\omega\tau}{1 + \omega^2\tau^2} \right) \quad (3)$$

Where  $\omega$  is the angular frequency =  $2\pi f$ , where  $f$  is the input frequency measured in Hz, and  $\tau$  is the time constant =  $RC$ .

## 2.2 Cole-Cole model

The Cole-Cole model consists of 2 resistors and 1 capacitor in parallel or series combination. The parallel combination was considered as series model blocks the the flow of DC due to presence of the capacitor element. The circuit representation of the Cole-Cole 2R-1C model is shown in Figure A.4.

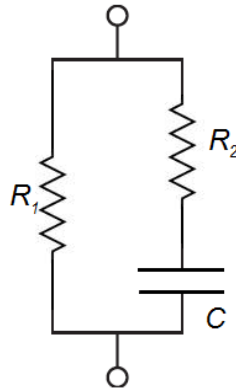


Figure A.4: Diagram of Cole-Cole model in parallel combination

If the admittance,  $Y$ , of the circuit is calculated using Eqn. 1, then the effective conductivity,  $G$ , of the Cole-Cole model is:-

$$G = Y - \frac{\omega^2 C \tau + j \omega C}{1 + \omega^2 \tau^2} \quad (4)$$

Where  $\omega$  is the angular frequency =  $2\pi f$ , where  $f$  is the input frequency measured in Hz, and  $\tau$  is the time constant =  $R_2 C$ .

The real and imaginary parts of the conductivity were calculated using Eqns. 3 and 4, and the results were plotted with respect to frequency.

### 3. Results and discussion

The conductivity of chick DRG tissue using Maxwell-Wagner model and Cole-Cole model was calculated and plotted with respect to input frequency, as shown in Figure A.5. The results are also tabulated in Table A.1.

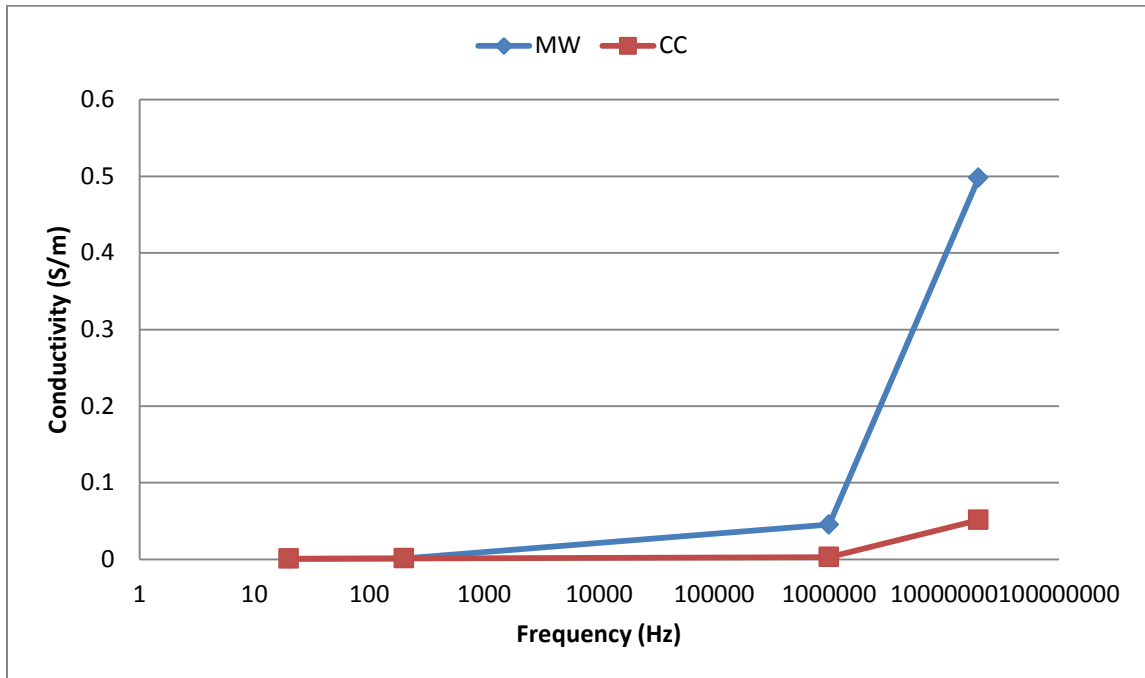


Figure A.5: Plot of DRG conductivity using Maxwell-Wagner model and Cole-Cole model, with respect to frequency. The conductivity values were obtained by using admittance equations of these models. The results show very low conductivity values at 20Hz, 200Hz but increase at higher frequencies. However, the values of conductivity at high frequencies for Maxwell-Wagner and Cole-Cole models differ by about 0.45 S/m.

Table A.1: List of conductivities for Maxwell-Wagner and Cole-Cole models for different frequencies.

Frequency (Hz)	Conductivities (S/m)	
	Maxwell-Wagner	Cole-Cole
20	0.001	0.001
200	0.001	0.001
1000000	0.04	0.003
20000000	0.5	0.05

The conductivity of the DRG at 20Hz and 200Hz was same for both the models, as 0.001 S/m. As the input frequency increases, the DRG conductivity also increased. However, at high frequencies, the conductivity values of Maxwell-Wagner and Cole-Cole models did not match. The values of conductivity using Maxwell-Wagner model gave higher values than Cole-Cole model. Although the pattern of the increase was similar in both cases (an increase at 1MHz), a difference of about 0.45 S/m between the two models at 20MHz. Since no data is available in literature on chick DRG conductivity, the results of the present study could not be validated. However, the results demonstrated that an increase of input frequency increases the conductivity of the tissue.

The increase in conductivity of the tissue is due to the capacitive nature of the double layer cell membrane [53]. The two layers of lipid in the lipid bilayer of the cell membrane act as the two plates of the capacitor. As explained in Chapter 2, at DC and low frequencies, the capacitive component of the cell membrane allows little or no

current flow inside the cytoplasm due to the high capacitive reactance of the membrane. At high frequencies, the capacitive branch is short, and maximum current flows through the intracellular branch inside the cytoplasm. According to Roth, the conductivity of the tissue becomes frequency dependent due to the capacitance of the cell membrane [33]. Thus, at DC and low frequencies, the current is restricted to the interstitial space while at high frequencies, C shunts across the membrane. Although at high frequencies the conductivity of the tissue is more, the restriction of current at the membrane at DC and low frequencies may help in increasing the membrane voltage, which may have an indirect effect on neurite growth and density. Further experiments need to be done to prove this hypothesis.

#### 4. Conclusion

The chick DRG tissue was modeled using Maxwell-Wagner and Cole-Cole models, assuming the tissue as a suspension of cells. Present results show that increase of input frequency increases the conductivity of the DRG. However, the values of conductivities at high frequencies had a difference of 0.45 S/m between both the models. With no literature data on chick DRG conductivity, these results could not be validated. The frequency dependence of the tissue conductivity was due to the capacitive nature of the cell membrane. At DC and low frequencies, the current was restricted in the interstitial space, which may increase the membrane voltage of the cells, thereby having an effect on the neurite growth and density. However, more experiments need to be done to prove the results obtained by the present study.

## APPENDIX B

### MATLAB CODES

```
clc;
clear all;
close all;
original = imread('imgb.tiff'); % READ ORIGINAL IMAGE
figure;
imshow(original); %DISPLAY ORIGINAL IMAGE
BW = im2bw(original,0.3) %THRESHOLD
count = 0; %DEFINE VARIABLE 'COUNT'
for i = 1:1678
    for j = 1:1678
        if BW(i,j)==0 % COUNT NO. OF WHITE PIXELS

            count=count+1; %INCREMENT VARIABLE 'COUNT'

        end

    end

end
end
count % DISPLAY VARIABLE COUNT VALUE
```

#### Code 1: MATLAB code for viability study

```
clc;
clear all;
close all;
original = imread('sample1.tiff'); %READ ORIGINAL IMAGE
figure(1);
imshow(original); %DISPLAY ORIGINAL IMAGE
BW = im2bw(original,0.3) %THRESHOLD
count = 0; %DEFINE VARIABLE 'COUNT'
image1 = BW(1:1483,1:1333,:);% CROP IMAGE (TOWARDS A)
figure(2);
imshow(image1);% DISPLAY CROPPED IMAGE
image2 = BW(1:1483,1334:1665,:);% CROP IMAGE (TOWARDS C)
figure(3);
imshow(image2);% DISPLAY CROPPED IMAGE
for i = 1:1483
    for j = 1:1333
        if BW(i,j)== 0;%COUNT WHITE PIXELS
```

```

        count=count+1;%INCREMENT VARIABLE 'COUNT'
    end
end
end
count % DISPLAY VARIABLE COUNT VALUE

```

### Code 2: MATLAB code for density study

```

clc
clear all
close all

% Create data for the polar plot function
t=0; % MINIMUM ANGLE
r=700; %MAXIMUM RADIUS
aa=0.0174; %DEGREE TO RADIANS CONVERSION FACTOR

% ADD ANGLE AND LENGTH OF NEURITE TIP
t1 = aa*172.63;
r1 = 142.32;
t2 = aa*113.62;
r2 = 100.32;
t3 = aa*163.62;
r3 = 77.53;
t4 = aa*255.72;
r4 = 153.25;
t5=aa*233.63;
r5=132.53;
t6=aa*107.84;
r6=125.63;
t7=aa*214.04;
r7=173.76;
t8=aa*263.15;
r8=84.73;
t9 = aa*173.43;
r9=99.73;
t10= aa*273.72;
r10=198.53;
t11 =aa*292.32;
r11=121.63;
t12= aa*312.82;
r12=176.42;
t13=aa*329.27;
r13=155.52;
t14=aa*355.27;
r14=75.52;
t15=aa*7.76;
r15=226.54;
t16=aa*22.76;
r16=191.76;
t17=aa*42.35;
r17=140.62;
t18=aa*65.87;
r18=86.78;

```

```

t19=aa*77.37;
r19=158.76;
t20=aa*88;
r20=107.73;

% Create a polar plot using the function polar
figure;
polar(t,r);
hold on
polar(t1, r1, '*r');
hold on
polar(t2,r2, '*r');
hold on
polar(t3,r3, '*r');
hold on
polar(t4,r4, '*r');
hold on
polar(t5, r5, '*r');
hold on
polar(t6,r6, '*r');
hold on
polar(t7,r7, '*r');
hold on
polar(t8,r8, '*r');
hold on
polar(t9, r9, '*r');
hold on
polar(t10,r10, 'ob');
hold on
polar(t11,r11, 'ob');
hold on
polar(t12,r12, 'ob');
hold on
polar(t13,r13, 'ob');
hold on
polar(t14,r14, 'ob');
hold on
polar(t15,r15, 'ob');
hold on
polar(t16,r16, 'ob');
hold on
polar(t17,r17, 'ob');
hold on
polar(t18,r18, 'ob');
hold on
polar(t19,r19, 'ob');
hold on
polar(t20,r20, 'ob');

```

Code 3: Sample MATLAB code for directionality study

```

clc
clear all
close all
growth = [490.73 579.17 474.29 497.44 419.74 491.12 416.69 492.94
469.66 486.64 420.61 449.59 496.24 425.71 403.18 594.05 396.9 369.14
406.77 468.19 367.29 412.88 387.41 369.03 370.99 399.94 419.25 367.42
369.89 387.65 436.6 371.38 414.36 479.27 458.09 337.65 374.92 425.28
411.97 345.4 373.5];
freq = {'20Hz-a','20Hz-a','20Hz-a','20Hz-a','20Hz-a','20Hz-a','20Hz-
a','20Hz-a','20Hz-a','20Hz-a','20Hz-a','20Hz-a','20Hz-a','20Hz-
a','20Hz-a','20Hz-a','20Hz-a','20Hz-a','20Hz-a','20Hz-a','20Hz-
c','20Hz-c','20Hz-c','20Hz-c','20Hz-c','20Hz-c','20Hz-c','20Hz-
c','20Hz-c','20Hz-c','20Hz-c','20Hz-c','20Hz-c','20Hz-c','20Hz-
c','20Hz-c','20Hz-c','20Hz-c','20Hz-c','20Hz-c','20Hz-c'};
p = kruskalwallis(growth,freq,'off')

```

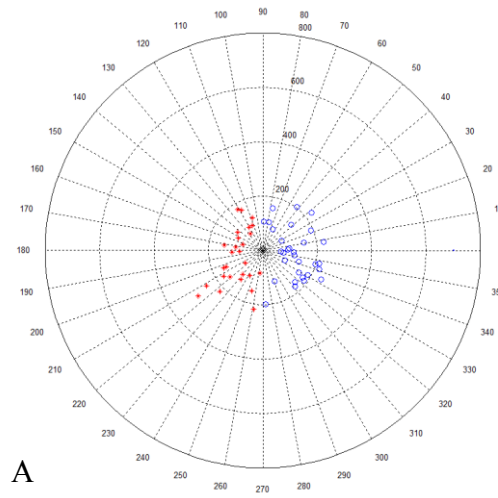
Code 4: Sample MATLAB code for statistical analysis using non-parametric test Kruskal Wallis one way ANOVA.

## APPENDIX C

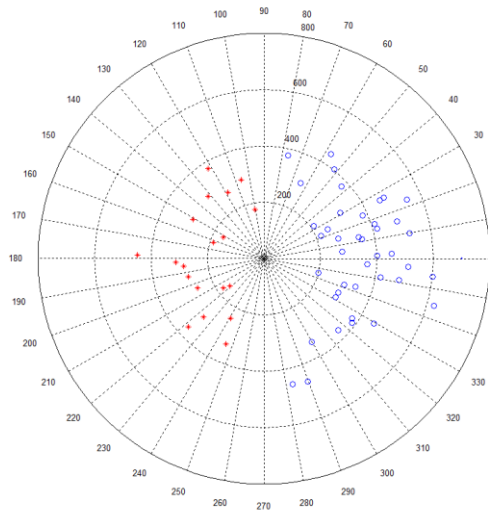
### DATA TABLES AND FIGURES

Table C.1: Cell densities of total cells and SC for mixed, non-adherent and adherent population, for the three time points. Data is depicted as average  $\pm$  standard deviation, with sample size, n=28, n=43 and n=45 for 1, 2 and 4 hrs time points, respectively.

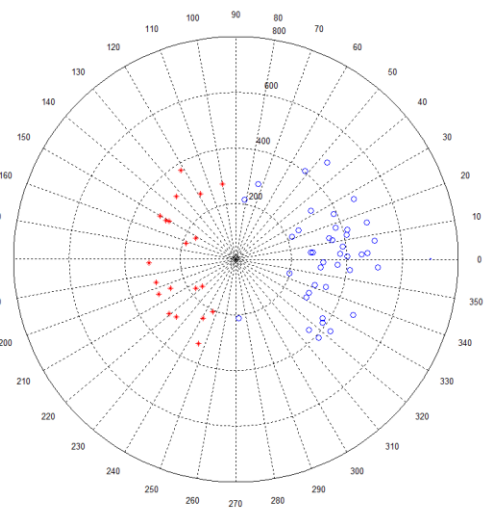
	Cell Densities (number x 10 <sup>3</sup> )				
Population	Time point (hr)		1	2	4
	No. of samples	45	28	43	45
Mixed	Total cells	7.593 $\pm$ 0.18	-	-	-
	SC	2.152 $\pm$ 0.11	-	-	-
Non-Adherent	Total cells	-	5.187 $\pm$ 0.12	2.572 $\pm$ 0.13	0.434 $\pm$ 0.02
	SC	-	3.691 $\pm$ 0.18	0.363 $\pm$ 0.07	0
Adherent	Total cells	-	2.493 $\pm$ 0.16	4.914 $\pm$ 0.16	7.255 $\pm$ 0.16
	SC	-	0	4.832 $\pm$ 0.11	6.842 $\pm$ 0.21



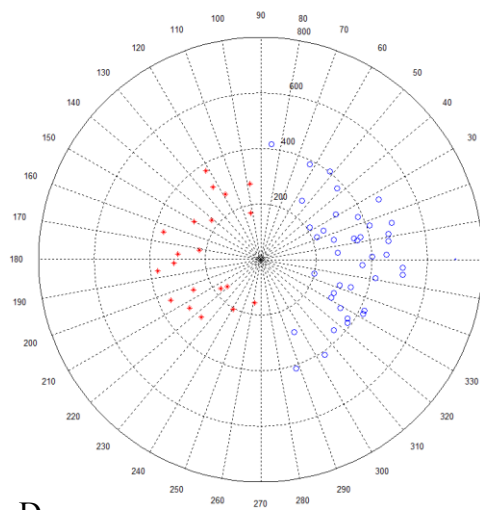
A



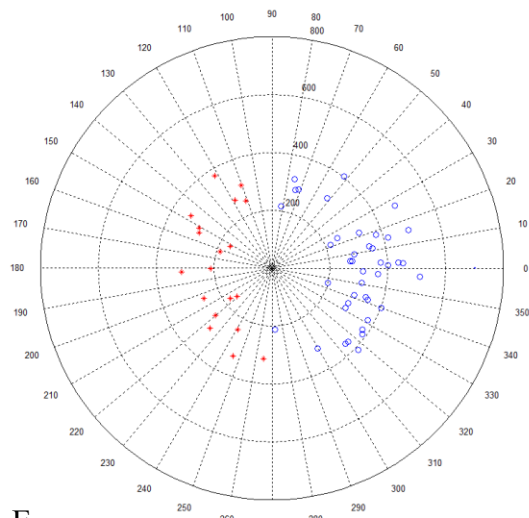
B



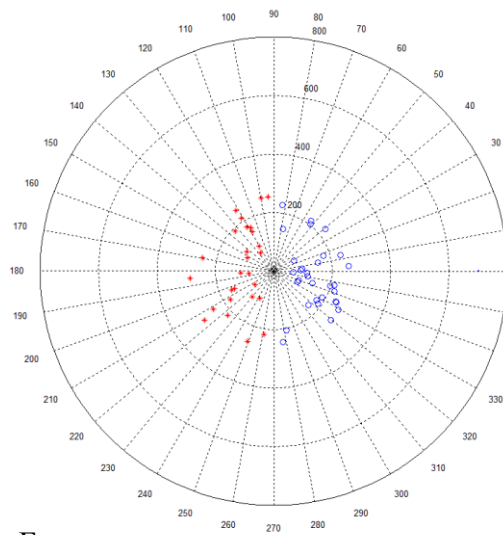
C



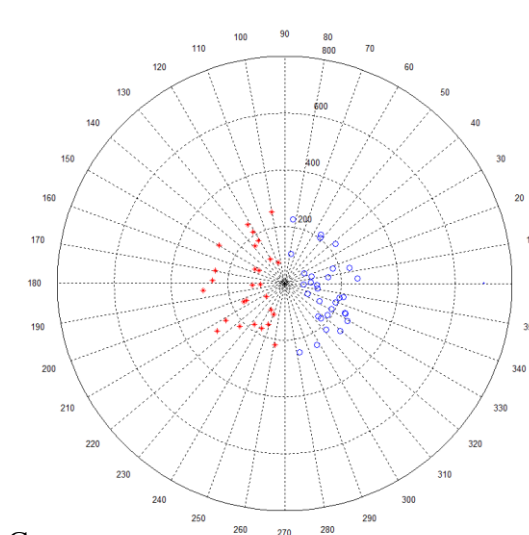
D



E



F



G

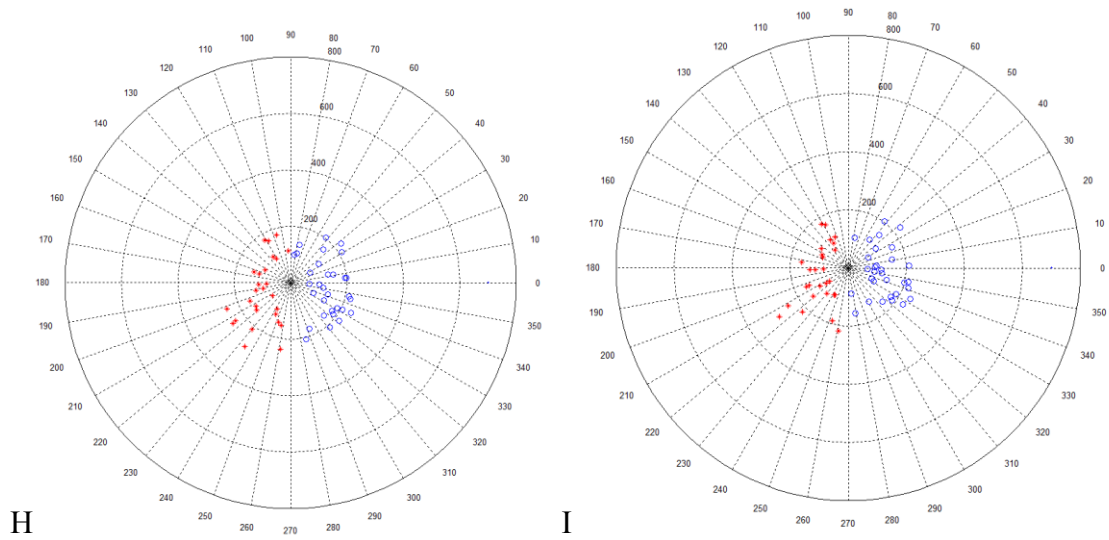


Figure C.1: Polar plots for directionality measurements. Figure (A) represents the polar plot for sham, B, D, F, H represent polar plots for position A for 20Hz, 200Hz, 1MHz and 20MHz, respectively, while C, E, G, I represent polar plots for position C for 20Hz, 200Hz, 1MHz and 20MHz, respectively.